

**NASA
Technical
Paper
3342**

June 1996

**Experimental Reacting Hydrogen Shear Layer
Data at High Subsonic Mach Number**

C.T. Chang, C.J. Marek, C. Wey, and C.C. Wey



National Aeronautics and
Space Administration

1996

**Experimental Reacting Hydrogen Shear Layer
Data at High Subsonic Mach Number**

C.T. Chang and C.J. Marek
*Lewis Research Center
Cleveland, Ohio*

C. Wey
*NYMA, Inc.
Brook Park, Ohio*

C.C. Wey
*Ohio Aerospace Institute
Brook Park, Ohio*



National Aeronautics and
Space Administration

Office of Management

Scientific and Technical
Information Program

Contents

Nomenclature	v
1. Introduction	1
2. Experiment Description	2
2.1 Flow Facility	2
2.2 Diagnostics	4
2.2.1 Velocity Measurement	4
2.2.2 Temperature Measurement	6
2.2.3 Dynamic Pressure Using Microphones	7
2.2.4 Flow Visualization with Schlieren	7
2.2.5 Flow Visualization with UV Emission	8
2.3 Operating Conditions	8
2.4 Error Analysis	9
2.4.1 Flow Controls	9
2.4.2 Positioning Error	9
2.4.3 LDV Parameters	9
2.4.4 Thermocouple Uncertainty	10
2.4.5 Microphone Uncertainty	11
2.4.6 Imaging Limits	11
2.5 Coordinate Convention	12
3. Results and Discussion	12
3.1 Observations	12
3.2 Velocity Measurements	13
3.2.1 Mean Flows: U and V	13
3.2.2 Turbulence and Diffusion	14
3.2.3 Layer Growth Rate	15
3.2.4 Probability Density Function	15
3.2.5 Joint Probability Density Function	16
3.3 Thermal Distribution	16
3.4 Schlieren Imaging	17
3.5 OH Fluorescence at 306 nm (UV)	18
3.6 Flow Acoustics	18
3.6.1 rms Pressure Magnitude	19
3.6.2 Band Selection	19
3.6.3 Downstream Signal Sources	19
3.6.4 Signal Sources in Shear Layer	20
4. General Discussion	21
5. Conclusions	22
References	23
Table 1: Conditions of Related Planar Shear Layer Experiments	25
Table 2: Laser Doppler Velocimetry System Characteristics	28
Table 3: Flow Conditions	29

Table 4: Nonreacting Planar Shear Layer Velocimetry Statistics	30
Table 5: Reacting Planar Shear Layer Velocimetry Statistics	33
Table 6: Shear Layer Width Characteristics	36
Table 7: Measured Temperature Distributions	37
Table 8: Microphone Measurement Intensities	39

List of Figures:

1. Computational fluid dynamics versus experiment	40
2. Mach number regimes of planar shear layer experiments	41
3. Absolute flow speed regimes of planar shear layer experiments	42
4. Schematic diagram of planar reacting shear layer wind tunnel	43
5. Test cell facility flow routing, cell CE-9B, ERB	44
6. Nozzle geometry	45
7. Inlets and test section	46
8. Details of hydrogen-fueled torch	47
9. Layout of LDV table components	48
10. TSI 9100-7 four-beam, forward-scattered laser Doppler system	49
11. Seeder design	50
12. Infinite-line microphone assembly	51
13. Microphone locations	52
14. Schlieren and LDV table in three dimensions	53
15. Streamwise mean flow distribution, $U(x,y)$	54
16. Streamwise mean flow velocity profiles normalized by vorticity width	55
17. Streamwise mean flow velocity profiles normalized by speed differential	56
18. Cross-stream mean flow velocity in planar shear layer, $V(x,y)$	57
19. Streamwise and cross-stream absolute turbulence intensities, $u'(x,y)$, $v'(x,y)$	58
20. Streamwise and cross-stream fluctuations normalized by streamwise mean speed ...	59
21. Streamwise turbulence intensity normalized by local mean flow speed	60
22. Reynolds stress normalized by local turbulence intensities u' and v'	61
23. Reynolds stress normalized by slip speed squared	62
24. Shear layer vorticity width boundaries	63
25. Probability density functions of streamwise velocity component, u	64
26. Probability density functions of cross-stream velocity component, v	67
27. Joint probability density function contours of streamwise and cross-stream flow velocities, u and v	70
28. Temperature distribution at three downstream locations from splitter plate tip	73
29. Schlieren images of nonreacting planar shear layer flows	74
30. Schlieren images of reacting planar shear layer flows	75
31. Mean intensity of 256 schlieren images of reacting and nonreacting flows	76
32. Mean contour of 256 schlieren images of reacting and nonreacting flows	77
33. rms contour of 256 schlieren images of reacting and nonreacting flows	78
34. Mean instantaneous shear layer width ($\delta_{\omega}(x)$) without layer corrugation	79
35. Long-time exposure (>1 ms) OH emission image	80
36. Instantaneous (approximately 10 ns) OH emission image	80
37. Spectral density of microphone 5 at airstream nozzle inlet near hydrogen torch	81
38. Spectral density distribution of microphones with and without reaction	82
39. Microphone temporal signal cross-correlation	83

Nomenclature

a	speed of sound, m/s
f	LDV data frequency, Hz
M	Mach number
M_c	convective Mach number
Mo	average molecular weight, g/mole
P	pressure, Pa
r	ratio of fuel-side to air-side streamwise mean flow, U_2/U_1
R_{uv}	normalized cross-correlation of u and v
T	thermocouple temperature, not corrected for radiative loss, K
U, V	streamwise and cross-stream mean flow speeds, m/s
U_c	convective speed, speed at which dynamic pressure from the two streams are equal
U_m	mean streamwise speed, $(U_1 + U_2)/2$, m/s
ΔU	slip speed, $U_1 - U_2$
u, v	instantaneous streamwise and cross-stream speeds, in x and y directions, m/s
u', v'	streamwise and cross-stream absolute turbulence intensities, rms, m/s
x	streamwise coordinate, origin at splitter plate tip, mm
y	cross-stream coordinate, origin at splitter plate tip, mm
y_c	location at each streamwise station where U_m exists
δ_w	layer width based on maximum velocity gradient (vorticity width)
δ'_c/δ'_i	growth rate ratio of compressible shear layer to incompressible shear layer
ρ	mass density, kg/m ³
Φ	equal volume equivalence ratio

Subscripts:

max	maximum
0	total
1	air side (lower duct) flow parameter
2	fuel side (upper duct) flow parameters

1. Introduction

In a survey of research done on turbulent reacting flows, Strahle and Lekoudis (1985) noted that much more turbulence and reacting data are needed for planar reacting shear layers at high Reynolds number conditions, especially when using nonintrusive laser diagnostics. This observation is all the more important as large deviations exist between experimental data, such as that of Hermanson (1985), and computational models such as the standard two-equation turbulence-dissipation model, here shown in figure 1(a) (Claus, 1986). To further complicate the issue, most such experimental studies have not included the magnitude of the turbulence, a severe handicap when the data are used as a computational fluid dynamics (CFD) benchmark.

Computer models, of course, can be expanded to produce a more accurate result, if the result is known first. For example, by including generation terms from velocity and concentration coupling, and by adding 8 more differential equations and 11 more constants (Farshchi, 1986) achieved a much better comparison, here shown in figure 1(b). The relevant question, however, is whether these formulations and constants are universal over a large range of interest.

Data are available on planar shear layers with reactions at lower speeds. Batt (1977) studied a wall jet mixing into still air through dilute nitrogen tetroxide dissociation by using seeded flow photography. He observed that the turbulent motion in a shear layer is characterized more by random three-dimensional motion than by two-dimensional coherent structures, and he inferred a turbulent Prandtl number of 0.5 from his reacting shear layers. The speeds involved were only 15 and 7 m/s, respectively. Wallace (1981) studied the shear layer in a duct by reacting dilute nitric oxide with ozone in helium, nitrogen, and argon and using simultaneous shadowgraphs. His main conclusion was that the reaction heat release did not change the overall shear layer growth rate, with the growth due to thermal expansion being countered by entrainment rate reductions caused by the attenuation of the smaller scales that was visible from his shadowgraphs. As in Batt's case, these are low-speed experiments (25 m/s flows), which are much lower than the speed involved in commonly used combustors. Whether these same phenomena also exist at the higher speed regimes is not well understood.

With the resurgence in high-speed flow research, the need to understand mixing and reaction in compressible flows is even more pressing, and major efforts are being carried out in supersonic flows to address the issues involved in planar shear layers (e.g., Clemens and Mungal (1992), Goebel, et al. (1990), Messersmith, et al. (1991), and Samimy and Elliott (1990)). However, a large gap exists in the high-subsonic range of the data base that is applicable to advanced gas turbine combustors, afterburners, ramjet combustors, and internal rocket flows. A partial listing of planar shear layer experiments done in the last 20 years is shown in table 1. Figures 2 and 3 plot these experiments by their Mach numbers and absolute flow speeds. They show that the only

recent data associated with the high subsonic range were taken by Hall (1991) in CalTech's blow-down tunnel, which has a very short time span and does not provide turbulence measurements. As the figures show, few planar shear layer experiments have been done in the high subsonic range, let alone any with chemical reaction.

At NASA Lewis, the National Propulsion System Simulator Program proposes to use integrated CFD codes to shorten the gestation time of jet engine design cycles. This optimization process is based on the premise that codes accurate over the desired operating ranges are available. Accurate combustor codes, however, require accurate physical models of the reacting shear layer, since the latter is essentially the commonly found cooling film on modern combustor liners. Thus, CFD model development and verification are essential. Assuming that the reacting shear layers will behave the same way as those without reaction and heat release is extremely risky.

For the purpose of CFD verification and to answer the questions raised above, a continuous-flow, reacting shear layer facility was built at NASA Lewis to provide a comprehensive set of reacting shear layer data, including boundary and initial conditions. This report presents velocity and temperature data obtained on May 27 and June 10, 1992, schlieren photographs obtained in March 1991, and hydroxyl (OH) fluorescence images obtained in November 1991. Presented here are the mean velocities, turbulence intensities, Reynolds stress distributions, temperature profiles, and some images for a planar shear layer of hot air reacting with hydrogen (diluted with nitrogen). Hydrogen was chosen as the fuel because of its relatively fast and well-known reaction kinetics, and also because it has the simplest reaction among commonly used propulsion fuels. A nonreacting shear layer substituting air for the hydrogen stream was also measured for direct comparison. (Using helium is too expensive at this scale.) The high-speed, high-temperature air side flowed at Mach 0.71, and the speed ratio was 0.34. The shear layer width Reynolds number at $x=300$ mm based on average viscosity, local layer width, and slip speed, was about 1.8×10^5 . These speeds are about an order of magnitude larger than those of previously available reacting experiments. Flow field velocities were measured with a two-component laser Doppler velocimeter (LDV), and the temperatures were measured with platinum wire thermocouples.

2. Experiment Description

2.1 Flow Facility

A continuously operating, planar reacting shear layer wind tunnel was built to provide optical diagnostics of the phenomenon. It is located in test cell CE-9B of the Engine Research Building. Figure 4 shows the wind tunnel schematic and the approximate dimensions of the experiment. Figure 5 shows the support facility piping of the test cell.

The two streams enter the test section horizontally and parallel to each other. A compressor supplies a maximum of 16 kg/s of air at 30 atm. A control valve then throttles it down to the desired pressure. Part of this air is diverted for cooling the test section, such as the "slave" air streams above and below the test section and the air film that cools the windows. The air used for combustion is diverted away and heated to 870 K by a nonvitiating heater. This flow is introduced into the test section below the horizontal splitter plate. The fuel streams, composed of nitrogen and hydrogen, are provided separately from bulk trailers. A typical run consists of a single hydrogen trailer of 45,000 scf (104 kg) or 70,000 scf (163 kg) capacity and two 70,000 scf (2300 kg) nitrogen trailers. The nitrogen gas is heated first by a steam heat exchanger, for safety reasons, and then is mixed with the hydrogen outside the test cell before being introduced into the test section above the same splitter plate. This fuel stream can flow a maximum of 0.055 kg/s of hydrogen with a maximum dilution of about 3 kg/s of nitrogen. For nonreacting experiments, part of the compressor-supplied air is routed to the upper duct in place of the nitrogen-hydrogen mixture. Flow rate measurements are done, along with pressure drop measurement across orifices downstream of the individual control valves.

The inlet ducts change the circular flow cross sections to rectangular. In these sections, turbulence flow conditioning is by means of screens and honeycombs. Each stream first passes through a 40% blockage plate with 1.27 cm diameter holes into a 25 by 20 cm rectangular duct. At 127 cm upstream of the splitter plate, honeycomb grids with 0.63 cm squares are inserted to break up the large scales of turbulence. The grids are followed by two 30-mesh screens with 0.33 mm diameter wires at 107 and 97 cm upstream of the splitter plate. The flow area then contracts five times in a two-dimensional nozzle, thus further reducing the normalized turbulence intensity. The shape of the nozzle is defined by the two-arc method as done in Hermanson's (1985) experiment, with the dimensions shown in figure 6. The two streams converge at the splitter plate tip with a 6° convergence angle for the last 12.1 cm. The splitter plate is made of a Haynes alloy to provide mechanical strength at high temperature, and the tip is cut to 0.2 mm thick to reduce edge ripple.

The test section is a rectangular channel inside a pressure housing rated for three atm. It is 10 cm high by 20 cm wide at the splitter plate tip, and the upper and lower walls (flappers) extend about 63 cm downstream from the splitter plate tip (fig. 7). The upper and lower walls are hinged at the upstream end, and each has a 4 cm range of motion at the downstream end, allowing the duct cross section to be changed so that the axial pressure gradient can be adjusted to zero. These walls are convectively air cooled on the back side with airflow independently adjusted (slave airflows). Each wall has two 2.5 cm wide quartz windows, one 17.5 cm long and the other 23 cm long, allowing laser sheet lighting for illuminated imaging work.

The two side walls each contain two sets of quartz windows (7 mm thick) with individual viewing areas of 8.5 by 21.5 cm. The windows are air film cooled on the inside of the test section, each with a 0.48 cm wide film slot beginning at the upstream edge of each window and covering the complete height of each window. They allow optical access for LDV and imaging cameras. The first set of windows includes approximately 4.5 cm of the splitter plate so that the upstream boundaries can be observed and measured. Using the splitter plate tip as the origin, the two viewing areas cover from $x = -4.5$ to 17.0 cm and then from $x = 26.0$ to 47.5 cm.

The test section is followed by a transition section from a rectangular cross section at the test section outlet to a 45 cm diameter round area where backpressure tubes can be inserted for operating at elevated pressures. Water sprays then cool the gases, which are expelled over the test cell roof.

A hydrogen-fueled torch using vitiating heating provides the hot air duct with some 300 K temperature boost. This boost is necessary to sustain and stabilize the reaction inside the test section. Tests without this boost (even with nitrous oxide addition) did not lead to self-sustained ignition at the splitter plate edge. Figure 8 shows the construction of the torch and its placement in the hot air duct. Initial ignition is by a spark plug built into the torch, and the spark is turned off once the burning stabilizes. Flow control is by regulating the pressure across a choked orifice upstream of the torch. Torch ignition was done while the main-stream flow was low and was maintained throughout the flow envelope.

2.2 Diagnostics

2.2.1 Velocity Measurement

Figure 9 shows the layout of the two-component, forward-scattered, heterodyne LDV system used to measure the streamwise and cross-stream flow components in the planar reacting shear layer duct. The system parameters are listed in table 2. A 5 W argon ion laser operating in the multiline mode provided the illumination. The 488.0 nm blue line was used to measure the (horizontal) streamwise velocity component u , and the 514.5 nm green line was used to measure the (vertical) cross-stream component v . Laser beam output diameter was 1.5 mm.

The transmission optics were arranged on a 61 by 183 cm breadboard, essentially as a Thermal System, Inc. (TSI) model 9100-7 four-beam system (fig. 10). The multiline emission was separated by using a prism color separator before the green (514.5 nm) and the blue (488.0 nm) beams were sent through separate beam splitter crystals. Beam separation distance was 50 mm.

An 60 mm diameter achromatic lens with 602 mm focal length focused the four beams into the test section centerline through the large 10 by 20 cm windows. For the green beams, the waist

was 262 μm wide and 6.3 mm long and the fringe width was 6.18 μm . For the blue beams, the waist was 250 μm wide and 6.0 mm long and fringe width was 5.86 μm . For the cross-stream component v , a 40 MHz shift was added through a Bragg cell because flow reversal is possible in this direction; no frequency shift was used for the streamwise component u .

Since the incident beams converged at 5.3° angle, the LDV system could not measure from any location closer than 5 mm to the surface of the splitter plate. Therefore, the velocity mapping at $x=0$ mm detoured around the tip of the splitter plate using the tip as the center of a 6 mm semi-circular arc. For simplicity, LDV measurements taken from this arc were treated as part of the $x=0$ mm scan.

The receiving optics were arranged on a 61 by 61 cm breadboard on the other side of the test section. The elements for the two color components were separated to optimize the amount of light collected. Each train consists of a receiving lens, an integral assembly containing a 100 mm focusing lens, a narrow-band color filter, and a two-axis traverse adjustment. A photomultiplier tube (PMT) with a 175 μm diameter pinhole is attached to each train to collect the light. Each train is placed at an angle of 10° off axis in order to avoid having the incident laser beam shining directly into the PMT's. An $f9$, 350 mm focal length lens was used to collect the blue light and an $f11$, 450 mm focal length lens was used to collect the green light.

The signal from the blue PMT was sent directly to a TSI model 1990 burst counter processor; the PMT signal of the frequency-shifted green light was first sent back into a downmixer (removing 30 MHz) and then to the processor. The transmission lines from the PMT's in the test cell to the processors inside the control room were a pair of 30 m long RG58 coaxial cables.

The burst counters were normally set to constant settings for the duration of the experiment once the computer-controlled mapping started. The filter amplifier gains were usually set between 1 and 2. The blue cutoff frequencies were 20 and 100 MHz. The green cutoff frequencies were 2 and 20 MHz. The signals were sent out through the counters' analog frequency outputs with 12-bit resolution. They were linearly proportional to the detected Doppler frequencies and hence to the velocity components. The analog signals were sent to a sample and hold board and then to a 12-bit digitizer board on the Concurrent 5600 data acquisition computer. The sampling rate was fixed at 20 kHz per channel.

Flow speeds were measured at various locations from the splitter plate tip to 330 mm downstream. The measurement probe volume was moved relative to the test section by driving the whole optics table with stepper motors controlled by a CompuMotor 4000 controller. This controller in turn was controlled remotely by the Concurrent 5600, which controlled the measurement location as well as the high-speed data acquisition. The data acquisition and control software were custom written by the authors. Typical cycling time was about 7 s per location, of which only 4 s were data acquisition (2 s for the nonreacting case) and the rest was occupied by

table traverse and stabilization. The total mapping cycle covering the two sets of windows took about 30 min. This was usually the maximum mapping time, as the seeders rarely worked well longer than 30 min.

Various types of seeds were used to scatter the incident laser beams, but a mixture of 20% fumigated silica of 0.06 μm diameter and 80% alumina of nominally 1 μm diameter was eventually adapted as standard. (Attempts at using titanium dioxide formed from the reaction of titanium tetrachloride and steam were unsuccessful, as no scatterable particles were observed at temperatures above 700 K. The technique was abandoned.) The powder mixture was first heated in an oven to 470 K for an hour to dry the powder, and then it was poured into the two seeders, one each for the upper fuel duct and the lower air duct.

The seeder design (fig. 11) used features from fluidized beds and cyclone separators. The cylindrical seeders were made with 15 cm diameter, 60 cm long steel pipes, capped at the top and bottom with end caps. The latter were attached to the pipe with standard flexible seals for quick release. Dried nitrogen was introduced in the center of the bottom cap and entered the bottom of the mixing chamber through a porous sintered metal plate such that the gas moving upward through the 5 cm thick seed bed agitated the seeds. Two small swirl nozzles about 5 cm from the bottom of the bed injected air tangentially into the fluidized bed chamber so that larger particles were spun to the side and attached themselves to the wall as the bulk flow rose. The particle-laden flow was siphoned off the center of the top cap and ducted (through a copper tube to prevent static electricity buildup) to a 1.2 cm diameter probe inserted into the main air ducts upstream of the honeycombs. During operation, the carrier nitrogen pressure normally was set to 420 kPa.

2.2.2 Temperature Measurement

The temperature profiles across the shear layer (in the vertical direction y) at three stream-wise stations were measured with open-ball, type-R thermocouple probes with 0.625 mm diameter wires. These servomotor-placed thermocouple probes were mounted on metal plates in place of the transparent windows. They were measured at the vertical midplane of the test section.

Because of the large thermal inertia of the thermocouple wire junction as well as the steep thermal gradient, traverse had to be slow. The typical traverse speed was approximately 0.2 to 0.4 mm/s to reduce error introduced by thermal inertia. The signal was amplified 500-fold by an instrumentation amplifier and fed into the sample and hold A/D of the computer. Sampling speed was 5 Hz.

Owing to the vertical motion of the splitter plate tip, a firm origin was defined from the centerline of the duct as it appeared from the two sets of large side windows. The thermocouples

were moved by a closed-loop position controller, and the thermocouple position was fed to the A/D board through an amplifier along with the output of the amplified thermocouple signal.

Measurements at $x = 150$ mm and $x = 300$ mm were performed to evaluate the thermal layer width. Measurement at $x = 0$ mm was done to assess the influence of the hydrogen-fueled torch on the temperature distribution across the inlet air duct.

2.2.3 Dynamic Pressure Using Microphones

The reacting shear layer facility contains many flow-related acoustic sources. Aside from the flow noise of the mixing layer itself, noise also is generated by auxiliary flows (such as the slave and film-cooling flows) as well as by flow control devices (such as the inlet and outlet valves and flow-conditioning screens). Each of these has characteristics that can be identified from the pressure perturbation it dispenses in the flow. High-frequency condenser microphones (Englund and Richards, 1984) were used to measure the acoustic pressure fluctuations at several locations inside the duct, thus providing some boundary conditions of the flow channel.

Figure 12 shows the high-frequency condenser microphones (B & K model 2633) used to measure pressure boundary conditions at locations indicated in figure 13. They had a flat frequency response up to 200 kHz. Each microphone was flush-mounted inside a canister that was attached to the rig, and a nitrogen purging source was used to prevent contamination and destruction by contact with the hot gas inside the test section. The line from the canister to the nitrogen source was about 70 ft long and was controlled by a 3 psi differential pressure regulator to control the amount of purge flow as well as to serve as an acoustic sink to minimize any reflected pressure waves. Microphones 1 and 5 were located in the inlet of the nozzles. Positions 2, 3, 6, and 7 monitored the signals in the test section.

Because the microphones were mounted 28 cm to 43 cm away from the static pressure taps on the top and bottom of the test section, the signals received by the microphones were not concurrent. After the signals had been digitized simultaneously, the small transport delays were removed from each microphone signal by advancing each signal by the same amount based on the lead-in tube length. Each sample contained five microphones each sampling at 50,000 samples per second for 10 s.

2.2.4 Flow Visualization with Schlieren

A standard schlieren system (with 30 cm diameter mirrors) capable of observing a whole window at once was used in conjunction with a 10,000 frame per second, high-speed, 16 mm film camera to capture the instantaneous density gradient distribution. The light source was a xenon

lamp. The light was made parallel by using 12 inch diameter parabolic mirrors. Knife-edges on the receiving side were placed horizontally to highlight the changes in the vertical direction. Figure 14 shows the approximate three-dimensional schlieren system layout in conjunction with the LDV setup.

The film frames were digitized into the Concurrent 5600 computer through a custom-made frame grabber board making 512 by 480 pixel, 8-bit images. The film was projected directly into a Sony charged couple device (CCD) camera through two neutral density filters so as to reduce any image intensity distortion from external influence. The images were blown up to use as many pixels as possible. The pixels of the camera have a width-to-height aspect ratio of 1.22; this was found by digitizing a 1 in. by 1 in. grid pattern. A series of 256 consecutive frames were digitized from each of the nonreacting and reacting experiments.

Average frame characteristics were found by averaging the 256 consecutive images. However, each instantaneous image does not reside on the same location on the digitized frame. This frame-to-frame displacement was corrected by using a custom-written pattern recognition algorithm based on the minimization of differences in key features from frame to frame.

2.2.5 Flow Visualization with UV Emission

An intensified, gated camera from Xybion with two-dimensional array (512 by 480 pixels) was used to measure OH fluorescence in the upstream window. A narrow-band optic filter centered at 306 nm with a 10 nm bandwidth was used to isolate the spontaneous emission of OH radical as a product of the combustion process. The focal plane was on the centerline of the test section with approximately a 5 cm wide field of view. However, because nearly the entire width of the reacting shear layer fluoresced, the images obtained also include unfocused signals from planes other than the centerline location. To freeze images, fast gate times of about 10 ns were used. For a time-averaged image, the gate times were extended to longer than 1 ms.

2.3 Operating Conditions

The nominal control settings and measured flow conditions are given in table 3. Flow times were limited by the capacity of the tanker trucks supplying nitrogen and hydrogen. A typical reacting run used two 70,000 scf trailers of nitrogen and one 70,000 scf hydrogen tuber. These supplies lasted 1 to 2 hr. For the nonreacting run, the upper fuel stream (nitrogen-diluted hydrogen) was replaced with air. The velocity ratio was fixed nominally at 0.34 for all experiments.

2.4 Error Analysis

2.4.1 Flow Controls

All flows were manually controlled with pneumatic valves. Flow rate fluctuations in the data acquisition period were maintained to within $\pm 0.6\%$ of the mean, peak to peak.

2.4.2 Positioning Error

The positioning uncertainty due to thermal expansion of the rig was about 0.5 mm vertically. As much as 5 mm displacement of the test section on other occasions has been noticed. In the reacting case, there was a spatial uncertainty regarding the exact location of the splitter plate tip (the origin) after the LDV data scan. This uncertainty was corrected by using the U profile at the $x = 0$ mm station as a guide. Apparently, the extra heating due to hydrogen combustion caused the rig to bow and displace vertically slightly, for this was not observed in the nonreacting hot air case. This spatial uncertainty was not present in the thermocouple measurements because the thermocouple translation mechanisms were fixed to the test section directly.

2.4.3 LDV Parameters

Uncertainty in the fringe width and hence the scaling value to convert the signal from frequency into absolute flow speed was 0.4%. However, because this uncertainty affected the whole data set equally, it did not alter the normalized characteristics of the data. Quantities such as normalized turbulence intensity, spectral densities, and scales were not affected.

Signal leakage of one component into the other because the two components were not orthogonal was not assessable, and we assumed it to be limited by the TSI-manufactured modular components. For example, for 400 m/s mean flow in the streamwise direction, only a 2.3° misalignment was necessary to cause a 16 m/s mean flow to appear in the cross-stream direction component.

It is well known that the signal gain setting on the TSI burst counter processors can affect the measured absolute turbulence intensity. As the gain was increased, signals and noise from smaller particles were accepted by the processor as valid results; thus increasing gain manifested itself as higher data rates. This condition was not assessed as it is a function of the nature of the seed size distribution, nominally rated at $1\text{ }\mu\text{m}$ diameter. However, this uncertainty is more sensitive in the lower level turbulence of the inlet free-stream flows. Assuming that the inlet turbulence is isotropic, approximately 25% error in the measured inlet turbulence intensities can be expected.

Signal discretization introduced approximately a 0.01% error with the 12-bit digitizer. In physical values the u and v components had uncertainties of 5.5 and 1.4 cm/s, respectively.

The effect of laser beam steering due to flow-field temperature changes on the signal was not noticeable. This lack of effect may be attributed to the normal incidence angle formed between the side windows and the optical axis, along with the shallow convergence angles of the incident laser beams, which minimized the misalignment of the focal points of the transmitting and receiving components. However, radiative heating of the table more than once caused misalignment in the optic system so that one or both of the signals disappeared completely. This was corrected by installing radiation shields on the table.

No vibration of the optical components was observed. The optics table was examined with accelerometers and was found to have no detectable displacement. The vibration of the rig itself was barely noticeable by physical touch, and the amplitude was judged to be less than 0.5 mm in the 30 Hz range.

The greatest source of random noise came from ground loop and electromagnetic interference from coupled electronic instruments. During operation, noise levels of approximately 20 mV from the analog output of the counterprocessor to the digitizer board on the computer could be observed. This level corresponds to roughly 1 m/s random noise on u and 1/4 m/s on v .

Velocity measurement error due to particle mistrack was at most 3% of the local rms turbulence level. Velocity bias due to unequal particle seeding density in the two streams was compensated for by using time averages instead of particle averages. The standard error for velocity measurement at any location was at most 1/90th of the corresponding measured turbulence level, or 0.5 m/s in u and 0.2 in v . This low error is the result of collecting at least 8000 samples; some locations had more than 60,000 samples in 4 s, and there the standard errors were reduced by the square root of the corresponding number of samples.

2.4.4 Thermocouple Uncertainty

Temperature measurements have significant errors at these elevated temperatures due to losses to conduction, advection, and radiation. Because the shear layer was a two-dimensional phenomenon and the length of the probe passed through the same region of the shear layer, no conduction along the length of the probe was significant as long as adequate time was given for the temperature to equalize. The variation was not discernible from the normal experimental fluctuation, which was about 20 K. Likewise, temperature recovery associated with the advection process was expected to be small, perhaps accounting for 15 K in the high-speed stream assuming a recovery factor of 80%.

By far the largest temperature error was the radiation loss; however, this may not have been

as large as it seemed. A worst-case scenario assumed the gas to be transparent and the surface emissivity to be 0.9. Assuming a gas temperature of 1500 K, a Reynolds number of 6000, and a Prandtl number of 0.8, Froessling's correlation gave a Nussult number of 45. Dividing the radiation flux at 1500 K from the heat transfer coefficient obtained from this Nussult number yielded a temperature loss of just 60 K. This result may not be so far-fetched in view of the very large Nussult number due to the high flow speeds. The actual correction would have varied inside the shear layer, of course, depending on the local conditions.

The temperature values presented in this report have not been corrected for radiation loss.

2.4.5 Microphone Uncertainty

The microphones were calibrated on site with a piston phone calibrator. It generates a sinusoidal pressure signal at 124.0 dB above the threshold of hearing (2×10^{-5} Pa) at standard atmospheric conditions. The increased cavity created by the extra purge lines decreased the gain of the microphones, but the calibration factor took this into consideration.

From day to day, however, the measured amplitude varied slightly, as the signal was contaminated somewhat with various radiofrequency sources inside the test cell. Measurements taken on the same day, however, were consistent. Thus, amplitude comparisons between data from different days were not reliable. However, other time-dependent information, such as the transport time between different microphones and correlation coefficients, varied less than 10%, a reasonable range for extracting qualitative information.

2.4.6 Imaging Limits

The absolute sizes of the schlieren images were uncertain, more so for the reacting series than the series without reaction. The sizes presented for the reacting series were estimated to have a 5% error margin, even though the aspect ratio was correct. The relative sizes of individual frames in the series were also correct. The nonreacting flow series, with the physical targets and the window frame visible, had a smaller size uncertainty of 2%.

The digitization of the high-speed camera films by using a projector and a CCD camera posed an uncertainty in the frame-to-frame illumination intensity that could be compensated for to a limited degree. Because the intensity of the projection lamp varied with the voltage fluctuation in the alternating-current power line, the same film image digitized several times could appear with different intensities. An accurate scaling factor for each frame was approximated by assuming that the total light received by each frame was the same. As result of this, the absolute intensity of the rms fluctuation is highly unreliable, although the relative relationship of each pixel to the whole image was meaningful.

The absolute sizes of the OH fluorescence images have an uncertainty of approximately 10%.

2.5 Coordinate Convention

A three-axis Cartesian coordinate system was defined with the origin at the tip of the splitter plate, at the duct centerline. The x coordinate was positive downstream. The y coordinate was positive upward across the stream. The z component, across the width of the shear layer, was not used. All velocity and temperature measurements were done within ± 0.5 cm of the rig centerline.

3. Results and Discussion

3.1 Observations

A slightly yellowish glow was noticed in the mixing zone where the combustion took place. The consensus opinion of the research personnel was that the hydrogen fuel from the bulk trailer was contaminated with sodium, as is typical of this source.

The temperatures of the two streams were not high enough to ensure spontaneous and sustained ignition inside the test section. To overcome this, 0.0022 kg/s of the total hydrogen flow was diverted into the heated air duct to fuel a hydrogen torch. (The quoted hydrogen flow includes this torch hydrogen.) This vitiated heating created a slightly uneven temperature distribution inside the air nozzle. A temperature rise of about 270 K was present for a significant distance across the layer (see section 3.3.1). This rise, unfortunately, increased the incident turbulence in the hot air stream to approximately 6 to 7%.

Data rates fluctuated throughout the 30 min data acquisition cycle as well as with locations of measurement, as is typical of the nonhomogeneous nature of the seeding process. The counterprocessors indicated data rates as high as 130 kHz per channel, but the excess data were not used since the computer was sampling only at the fixed 20 kHz frequency. Where the data rate was lower, the computer recorded the zeroth order hold nature of the processors' analog outputs as a series of steps. The sampling rates and sampling times are tabulated in table 2.

The acoustical signature's differed with and without reaction. In the presence of the non-reacting shear layer, a high-frequency hiss was heard in the control room. Microphone measurements have recorded wide-band dynamic pressures inside the test section to as high as 1200 Pa. When ignition in the shear layer was stabilized, the dynamic pressure roughly doubled and the tone heard in the control room was lower in frequency.

3.2 Velocity Measurements

The mean flow speeds, turbulent intensities, Reynolds stress, and the estimated data sample rates for each location inside the nonreacting shear layer are tabulated in table 4. The corresponding values for the reacting shear layer are tabulated in table 5. These two cases correspond to the flow conditions specified in table 3.

3.2.1 Mean Flows: U and V

The streamwise mean flow speeds U for the two shear layers at the same initial flow speeds are shown in figure 15. The free-stream speed remained stable for the nonreacting case but decreased slightly for the reacting case owing to the slightly divergent channel, approximately 10% less at the $x = 150$ mm station. Also, in the reacting flow case the free-stream speed at the cold fuel side was not measurable at the $x = 300$ mm and $x = 330$ mm stations owing to the displacement of the layer toward the low-speed side.

Velocity profiles for both cases were made self-similar by normalizing the cross-stream coordinates using the local vorticity width* based on the shear layer slip velocity. They collapsed into two curves in figures 16 and 17, suggesting that the layer was dominated by the shearing of the two streams. The collapsed curves were best represented by the error function (erf), also drawn on the same plot as a reference. The curve fit is not perfect, however, since the high-speed side tends to have a slightly steeper corner, as was observed by Hermanson (1985). Nevertheless, this feature is well within the data scatter.

The exception to this similarity phenomenon was the small deviation detected at the $x = 0$ mm station, this being the result of momentum deficiency introduced by the boundary layers from the splitter plate. Because this station was within the development length of 12 mm based on the Reynolds number criterion as specified by Goebel et al. (1990), this deficiency was expected.

*The choice of a vorticity-based layer width was not only a matter of convenience but one that indicates the character of the gradient form inside the layer. For a fixed profile form, such as erf, this width has fixed ratios to the various widths based on fixed percentages of the slip speed. In this case, a width based on the 10% to 90% definition was 1.02 times the vorticity width. Based on 5% to 95%, it was 1.31; on 2%, 1.63; and on 1%, 1.86. The hyperbolic tangent has been used by other researchers to provide tighter data fit to the velocity profile, but we considered it unnecessary as the chief driver of the mixing phenomenon in the shear layer was apparently the flow speed differential. In other similar fluid phenomena such as boundary layer profiles, the erf function appeared to be adequate.

The cross-stream mean flow velocity V shows no strong organization in figure 18. With reaction, however, there was a slight upward bias speed as the flow progressed downstream.

3.2.2 Turbulence and Diffusion

The distribution of absolute turbulence intensities for the streamwise direction u' and that for the cross-stream direction v' are shown in figure 19. The measured inlet intensities in the non-reacting case, normalized by the local U were approximately 2.5% and 3%, approximately two times higher than originally designed. The corresponding values were 4% and 5.6% for the reacting case. The normalized turbulence intensities are shown in figure 20. The much higher turbulence in the high-speed air duct was produced by the addition of the hydrogen torch. Note that the free-stream turbulences in both inlets for the nonreacting case were approximately the same size, suggesting that isotropic turbulence is a reasonable assumption as an inlet boundary condition. In the presence of the hydrogen torch, however, it is not.

Under the nonreacting condition, the u' profiles exhibited bell-shaped curves about the shear layer, whereas those in the reacting case were much more difficult to characterize because of the distortion of additional turbulence from the torch. However, the basically bell-shaped distribution remained, as shown in figure 21. The peak streamwise turbulences at each station were approximately the same for the two cases, although the peaks in the reacting case tended to be broader and moved toward the low-speed side, corresponding to the layer shift in figure 15.

The cross-stream turbulence v' did not vary as much as u' across the layer. Although there seemed to be a slight increase in the center of the shear layer at the more upstream stations, those at 300 mm and 330 mm were nearly flat in the nonreacting case, suggesting the lack of an organized transport process to transfer turbulent energy from u' to v' . Of course, the turbulence was highly nonisotropic inside the shear layer, with u' to v' at roughly a ratio of 3 in the middle of the layer.

The Reynolds stresses normalized with respect to the the turbulence components u' and v' were generally small in the incident flows (figs. 22 and 23), which was expected in isotropic free-stream flows. Without reaction, the values remained small and disorganized throughout the length of the shear layer, suggesting either the lack of large-scale coherent structures or that the larger scales were overshadowed by the more chaotic smaller scale motions.

With the presence of combustion, however, slightly larger values were detected at all downstream locations of $x > 25$ mm with values ranging from -0.15 to 0.2. A trend of larger positive values in the middle of the shear layer appeared, beginning at $x = 100$ mm, and became more

organized as the shear layer moved downstream. This positive value corresponded to the faster fluid moving upward and the slower fluid moving downward, suggesting the presence of a larger scale momentum exchange, perhaps even a vortex type of entrainment process. Schlieren photographs show the presence of large-scale structures related to the layer undulating in the streamwise direction; this feature is apparently absent without reaction. In the same manner, the somewhat small but organized negative values at downstream stations of $x > 25$ mm may represent the diffusion of high-speed fluid moving into slower fluids near the diverging bottom wall.

3.2.3 Layer Growth Rate

The mixing layer boundaries based on the vorticity width of the layer are presented in figure 24 for both cases (table 6). The mixing layer angles with and without reaction were approximately 8.1° and 6.1° , respectively, averaged from $x = 50$ mm to $x = 300$ mm, with the latter angle comparing favorably with the prediction based on the formulation of Dimotakis (1984) at 5.5° . The layer growth rate with heat release, however, was much larger than expected, contrary to the observations of Wallace (1981) and Hermanson (1985), where the maximum velocity gradient steepened with reaction instead of being flattened. The lateral flapping motion of the layer, however, can easily have flattened the time-averaged profile spatially.

Also different was the shift of the shear layer into the slower fuel stream when reaction was present; not only did the centerline shift, but both edges shifted as well (see fig. 24). No simple explanation is adequate. For example, one theory is that the torch somehow provided an initial upward flow along the centerline of the test section and that this upward motion continued throughout the length of the shear layer, as can be seen in figure 18. This is certainly a plausible explanation in that the shear layer transit time to traverse the 300 mm at the median flow speed of 270 m/s was approximately 1.1 ms. For an average upward motion of 16 m/s, the middle of the layer was displaced 18 mm during this same period. However, a review of the schlieren photographs showed that the mean layer position shifted toward the test section horizontal centerline when the main hydrogen was turned off, even while the torch was left on. Turning the torch off (equivalent to the nonreacting case) did not make a noticeable further shift. Thus, the presence of the torch alone was insufficient to explain the shift of the reacting shear layer toward the slower fuel side.

3.2.4 Probability Density Function

The probability density functions (PDF's) of the streamwise velocity component u in regions outside the shear layers showed normal Gaussian distribution about the mean flow speed, with

and without reaction. Inside, however, the distribution became heavily skewed owing to entrainment of fluid from the other stream. Figure 25 show distributions across the width of the mixing layer at $x = 25, 50, 75, 100, 150$, and 300 mm. Note that this same behavior was retained regardless of the presence of reaction. As the flow moved downstream, more of the cross-stream locations developed into the non-Gaussian distribution that is common inside a shear layer.

The PDF's of the cross-stream component v remained approximately Gaussian throughout the flow, even inside the shear layers, for both the reacting and nonreacting cases (fig. 26).

3.2.5 Joint Probability Density Function

The joint probability density functions (JPDF's) of u and v showed no distinctive axis of alignment throughout the free stream. Figure 27 shows the contours of these JPDF's taken at the marked locations. Inside the shear layer, no definitive pattern emerged for the nonreacting air-to-air flow. With reaction, a slight alignment occurred inside the shear layer at downstream locations. This observation is consistent with the slightly positive Reynolds stress measured at downstream stations and corroborates the development of organized turbulent transport inside the shear layer.

3.3 Thermal Distribution

The temperatures measured at $x = 0$ mm, $x = 150$ mm, and $x = 300$ mm are tabulated in table 7 for both the nonreacting and the reacting planar shear layer experiments. The resultant thermal layer width and thermal layer centerline are tabulated in table 3. The turbulent Prandtl numbers based upon the thermal and vorticity width are listed in table 6.

The dependence on the hydrogen torch for continuous ignition inside the shear layer raised an issue regarding the amount of disturbance to the hot airstream by the torch. Figure 28(a) shows measured average temperatures across the inlet plane at $x = 0$ mm. The temperature rise was not uniform across the cross section of the hot air inlet, and the highest increase was approximately 250 K. The presence of combustion in the shear layer itself did not vary this distribution significantly except at y locations immediately downstream of the splitter plate tip.

The temperature profiles measured at $x = 150$ mm show that the shear layer was fully developed (fig. 28(b)). The nonreacting shear layer appeared to exhibit an erf type of distribution while leaving a significant portion of the sampled locations as free stream. The nonreacting thermal layer was approximately 18.5 mm and was centered approximately $y = -5.1$ mm. The torch raised the average temperature approximately 200 K inside the layer, and the increase was nearly uniform for the width of the layer itself.

The heat release due to the combustion inside the shear layer itself was distributed across the shear layer in the form of a normal distribution. This heat release layer was approximately 29.4 mm thick and centered at approximately $y = -0.9$ mm.

Thermal layer width for the hot air shear layer was 37.6 mm at $x = 300$ mm (fig. 28(c)). It is based on the vorticity concept using the maximum thermal gradient found in the middle of the layer. With reaction, it was approximately 54.2 mm. For the nonreacting flow, the median temperature was reached at $y = 8.7$ mm, and the maximum temperature increase with reaction was registered at $y = 9.4$ mm. Both locations were significantly far from the midpoint of the corresponding momentum layers, which were at $y = -1.6$ mm and $y = 17$ mm, respectively.

3.4 Schlieren Imaging

Figure 29 shows a series of 12 consecutive frames for the nonreacting flow in the upstream window. The macroscopic behavior is quiescent, with extensive fluctuations associated with scales of the size, or smaller than, the local shear layer width. At an average advection speed of 265 m/s, an advected structure would move 2.65 cm between consecutive frames, or approximately 7.5 frames from the beginning of the window to the end. There was no apparent advection of large-scale structures and hence correlations from frame to frame. (A small vertical tab was placed in the lower left side to indicate the hot air side of the picture. A small arc protruding upward from the bottom of the test section is likely cold air drawn in from a microphone tap accidentally left open. This tap was 50 mm from the centerline of the duct and affected the measurement at the centerline only slightly. These features were not present in the reacting case.)

Figure 30 shows the corresponding images for the reacting case where large-scale corrugation of the shear layer is apparent. The layer was also visibly displaced upward into the lower speed fuel-stream side. The large-scale fluctuation cycled in roughly four to five frames, at approximately 2000 to 2500 Hz. Because the visible portion of each frame was approximately 15 cm long and 8 cm high, the wavelength of the corrugation was estimated to be between 10 and 30 cm. This upward shift of the layer position is consistent with the observation obtained by LDV measurement. A significant amount of thermal disturbance was introduced into the hot airstream from the torch upstream inside the lower duct.

The time averages of the schlieren photograph contours are compared in figure 31. Two images each averaged from 256 consecutive frames are shown with and without reaction. For the nonreacting case, the shear layer grew at approximately 6.6° and was displaced downward slightly by approximately 1° ; for the reacting case, the average layer spread angle was approximately 7.1° , not a significant change from the nonreacting case, except that the layer was shifted upward by nearly 4° .

To clarify the features of the averaged images, the contours of the reacting and nonreacting cases are shown in figure 32, and the corresponding rms value contours are shown in figure 33. (Because of the nonuniformity of the prism inside the high-speed film camera, each individual frame was digitized slightly displaced from the previous one. A special pattern recognition algorithm was developed to identify and match each frame so that the displacement effect is removed.) At first glance, it appears that the average growth rate of the reacting layer was lower than for the nonreacting case. However, the growth rates of the two cases are not directly comparable, as the gradient for the reacting case was much more gradual than that for the nonreacting case.

By removing the large-scale corrugation of the reacting shear layer, average widths for the reacting and nonreacting shear layer cases are shown in figure 34. Here, the mean growth rate for the first 5 cm of the mixing layer in the reacting case was much larger than that without reaction, at 11.6° and 7.6° , respectively. This difference disappeared after approximately 5 cm of flow, suggesting that the chief contribution of the large-scale corrugation is to lateral displacement of the layer instantaneously inside the duct, so that the layer is present over a larger region. Small or no change in the growth rate may imply relatively small change in terms of the flow structure that is relevant to mixing and entrainment.

3.5 OH Fluorescence at 306 nm (UV)

Figure 35 shows an image taken with the gate open for a relatively long time. The nearly triangular shape and uniform intensity distribution suggest that the reaction and mixing zone was distributed inside a well-behaved and growing shear layer with features corresponding to those observed in the schlieren images and in the LDV.

However, just as in the schlieren images, the short time gate of the camera produced the images taken consecutively in figures 36(a) to (d). They show that the OH emissions were highly localized with great frame-to-frame variation, especially with the previously observed layer corrugation. Thus, the wedge shape of the reaction zone and the shear layer is only a valid description under the time-averaged premise.

3.6 Flow Acoustics

The most important role for acoustic measurement is to assess the approximate locations of the fluid-dynamics-related acoustic and pressure perturbation sources. Normally, this is a straightforward process because the delay time between the multiple sensors tends to point to the general direction of the sources. However, here this process was much more complicated as not

only did each signal have to propagate across a spatially and temporally fluctuating medium through multiple paths, but also each received signal was subjected to “contamination” from a whole host of other sources. In a mathematical model, then, the measured signal is the summation of the multiple sources convoluted with the acoustical transfer function of the medium. The difficulty with determining the source or the medium solely from the acoustics is that both the acoustic transfer function and the sources are unknown. Statistics, at best, can only yield an educated guess as to the true nature of the shear layer. Other independent means are required to sort and reduce the number of variables.

3.6.1 Rms Pressure Magnitude

A simple overview of the rms pressure magnitudes collected by the microphones shows that reaction and heat release in the shear layer roughly doubled the acoustic pressure disturbances in the flow field. Table 8 shows the values from each microphone on four separate experiments as denoted by the dates. This shear layer doubling suggests that the magnitude of the flow turbulence was increased by approximately 70%, as the pressure perturbation varies as the square of the velocity fluctuation. The change in acoustic level was quite noticeable, even from inside the control room. The contribution from the torch itself (fig. 37) was small relative to the reacting shear layer and varied slightly across the frequency spectrum.

3.6.2 Band Selection

The pressure spectral density distributions (fig. 38) of the four microphones nearest to the test section suggest that the increase was associated mainly with lower frequency and hence larger flow disturbances. (The locations of these four microphones are shown in figure 13.) The difference between the pressure spectral density distributions with and without reaction are most evident in the 75 Hz to 2 kHz range and insignificant at higher frequencies. Reaction produced two large peaks: a broad band centered around 375 Hz and a narrower band around 1150 Hz. These correspond to wavelengths of approximately 60 cm and 20 cm, respectively. These peaks were not as distinctive in the downstream locations (microphones 3 and 7) as in the upstream locations (microphones 2 and 6).

3.6.3 Downstream Signal Sources

The cross-correlation of acoustic signals between the upper (2 and 3) and the lower (6 and 7) microphone pairs in figures 39(a) and (d) suggests that broadband pressure signals originated

from somewhere downstream and traveled upstream inside the test section. Measured transport delays in the streamwise direction, in all cases, showed that the bulk of this broadband signal propagated upstream. The positive delay times of the peaks means that the downstream microphones received the signals earlier than those in the upstream locations. The flat shapes of the correlation functions show that the delay times varied over a broad range, consistent with the model of multipath propagation through a nonhomogeneous medium such as a shear layer.

Calculated transport time delays using the propagation upstream model agreed with those shown in figures 39(a) and (d). These are based on the 56 cm distance between the microphone taps and on the propagation speed toward the upstream (a minus U). Without reaction, these calculated delays were remarkably close to the peaks shown in figure 39(a). A 3% increase in sonic speed was sufficient to match the calculated time to that measured. The delay time on the airstream side was somewhat longer than the measured 3.2 ms, but the discrepancy can be accounted for by the uncertainty in the mean flow speed and the sonic speed. Reaction in the shear layer reduced the delay time by approximately one-third on both the fuel and air sides. On the fuel side, the mismatch was only a few percentage points. On the air side, the calculated delay time of 2.0 ms was almost the same as that measured (fig. 39(d)) because the sonic speed in the airstream was increased owing to the vitiation-induced temperature increase (from 867 K to 1100 K). Calculated delay times based on signals moving downstream (a plus U) do not match anything in the experimental results.

These same two figures also suggest that the reacting shear layer was a major contributor of acoustic pressure disturbance in the test section. Reaction significantly increased the amplitude of the correlation peaks from approximately 0.3 to 0.5, suggesting that the portion of the wide-band signal originating from downstream increased with reaction. Whether these sources are related to the shear layer impinging on the exhaust valve or to the vortical structures in the shear layer as they are advected downstream is unknown, but the wide-band source is located in that direction.

3.6.4 Signal Sources in Shear Layer

Cross-correlation (figs. 39(b) and (c)) of microphone signals across channels (microphones 2 and 6) and (microphones 3 and 7) suggests that the shear layer itself also may be an important pressure fluctuation source. This source is a narrower band type, with cyclic rates of approximately 4.5 ms or 220 Hz. The near-unity correlation coefficients and the small time delays from locations across the shear layer mean that the two sensors were picking up nearly the same signals simultaneously, most likely from sources in the middle of the channel. It is unlikely that the shear layer was flapping in the channel, for that would appear as a correlation 180° out of phase. One workable hypothesis is that a series of flame kernels (or packets of reacting fluids inside the shear

layer) were advected downstream with the mean flow of the shear layer and were responsible for sending out pressure fluctuations to the sensors on either side of the test section.

The reacting cases produced much higher peak correlations, suggesting that reactions in the shear layer perhaps formed more coherent or stronger structures in the shear layer. The reduction in this magnitude in the downstream location may be explained by the breakdown of these structures as they were advected downstream and dissipated.

4. General Discussion

Although the nonreacting shear layer grew at about the same rate as predicted, the reacting shear layer grew at a much faster rate than predicted. One likely explanation of this difference is that the divergence of the upper and lower walls of the test section slowed the flow, set up an adverse pressure gradient, and caused the mixing layer to grow at a faster rate. However, transducers monitoring the test section pressures did not indicate this.

The growth rates for both of these cases, however, still fell within the established limits. The convective Mach numbers M_c in our reacting and nonreacting cases were 0.26 and 0.29. These Mach numbers correspond to δ_c/δ_i of 0.90 in figure 4 of Messersmith et al. (1988), meaning that the mixing layer was practically incompressible even though the two incident streams themselves were moving in the compressible regime. Then, from the incompressible plot of δ_i versus $\Delta U/U_m$ (fig. 5 of Messersmith), the growth rates of the reacting and nonreacting layers at 0.14 and 0.11 were found to be near the upper edge of the data scatter, ranging from 0.09 to 0.14.

In both cases, the velocity profiles collapsed onto the Erf curve. Without reaction, the thermal profile also fitted Erf as well. Because both the thermal and velocity profiles can be represented by Erf, turbulent entrainment was assumed to be the main mechanism by which elements from the two streams were brought together to react. The ratio of the momentum and thermal layers was used to form a turbulent Prandtl number for each case. These were 0.77 and 0.83 for the flows with and without reaction, a significant departure from Batt's (1977) value of 0.5.

The thermocouple data for the reacting case show significant heat release due to combustion in the mixing layer. The long dashed line in figure 28(b) shows a peak temperature rise of about 810 K. Assuming that the temperature increase is the direct result of local heat release due to chemical reaction, the turbulent Schmidt number of 0.77 was used to approximate the species distribution inside the layer. An approximate adiabatic temperature profile is shown here as the dash-dot curve in figure 28(c). It is about 250 K higher than the measured temperature peak with reaction, suggesting that perhaps approximately 70% of the reactants have been consumed. This proportion will increase with radiation loss correction for the thermocouples added, as the temperature difference will be less.

Heat release apparently increased the level of larger scale turbulence. Whether the increase in the turbulence scales was on the order of the layer width is uncertain, but schlieren photographs of the reacting shear layer in figure 30 clearly show large-scale corrugation of the shear layer, in some respect akin to a traveling wave. This type of behavior is coherent and correlatable and can be used to explain the origin of the small but organized Reynolds stress in figure 22. Assuming that only this larger scale motion is coherent, the approximately 25% cross-correlation coefficients in the u' and v' components from the last three downstream stations in figure 22 suggest that about 25% of the turbulence energy measured in the reacting flow can be associated with large-scale structures, compared with only about 10% in the nonreacting flow.

The changes in the finer flow scales inside the layers could not be determined from the present set of LDV data alone. The maximum 20 kHz data rate was only able to resolve length scales longer than 4 cm at 400 m/s mean flow speed. This size was larger than the mixing layer width for the first 200 mm of the layer and so is not meaningful in providing information regarding the smaller scales inside the layer itself. That information must come from flow visualization techniques.

5. Conclusions

Statistical values of measured velocity, turbulence, and temperature profiles were obtained at Mach 0.71 with and without reaction. However, the low convective Mach numbers of 0.29 and 0.26 mean that these cases can be treated as incompressible. Even with combustion, the error function fit the reduced velocity profile fairly well, suggesting that the shear layer was dominated by the shear of the two free streams. Reaction in the shear layer accelerated the shear layer growth rate and shifted the layer toward the lower speed side. It apparently also increased the larger scale turbulence, in this case the undulation of the shear layer itself, and slightly increased the organization of turbulent energy transport from the streamwise direction to the cross-stream direction.

Lewis Research Center
National Aeronautics and Space Administration
Cleveland, Ohio
March 31, 1996

References

- Batt, R.G., 1977, "Turbulent Mixing of Passive and Chemically Reacting Species in a Low-Speed Shear Layer," *Journal of Fluid Mechanics*, vol. 82, pp. 53-95.
- Brown, G.L and A. Roshko, 1974, "On Density Effects and Large Structure in Turbulent Mixing Layers," *Journal of Fluid Mechanics*, vol. 64, pp. 775-816.
- Chang, C.T., C.J. Marek, C.C. Wey, R. A. Jones, and M. J. Smith, 1993, "Comparison of Reacting and Non-Reacting Shear Layers at a High Subsonic Mach Number," AIAA-93-2381.
- Claus, R.W., 1986, "Modeling Turbulent, Reacting Flow," *Combustion Fundamentals*, NASA CP-2433. pp. 31-46.
- Clemens, N.T., and M.G. Mungal, 1992, "Two and Three-Dimensional Effects in the Supersonic Mixing Layer," *AIAA Journal*, vol. 30, no. 4. pp. 973-981.
- Dimotakis, P.E., 1984, "Entrainment Into a Fully Developed, Two-Dimensional Shear Layer," AIAA-84-0368.
- Elliott, G.S. and M. Samimy, 1990, "Compressibility Effects in Free Shear Layers," *Physics of Fluids*, vol. A2, no. 7, July, pp. 1231-1240.
- Englund, D.R. and W.B. Richards, 1984, "The Infinite Line Pressure Probe," NASA TM-83582.
- Farshchi, M., 1986, "Prediction of Heat Release Effects on a Mixing Layer," AIAA-86-0058.
- Goebel, S.G., J.C. Dutton, H. Krier, and J.P. Renie, 1990, "Mean and Turbulent Velocity Measurements of Supersonic Mixing Layers," *Experiments in Fluids*, vol. 8, pp. 263-272.
- Hall, J., 1991, "An Experimental Investigation of Structure, Mixing and Combustion in Compressible Turbulent Shear Layers," Ph.D. Thesis, California Institute of Technology, Pasadena, CA.
- Hermanson, J.C., 1985, "Heat Release Effects in a Turbulent, Reacting Shear Layer," Ph.D. Thesis, California Institute of Technology, Pasadena, CA.
- Messersmith, N.L., J.C. Dutton, and H. Krier, 1991, "Experimental Investigation of Large Scale Structures in Compressible Mixing Layers," AIAA-91-0244.
- Messersmith, N.L., S.G. Goebel, W.H. Frantz, E.A. Krammer, J.P. Renie, J.C. Dutton, and H. Krier, 1988, "Experimental and Analytical Investigations of Supersonic Mixing Layers," AIAA-88-0702.
- Miller, M.F., T.C. Island, J.M. Seitzman, C.T. Bowman, M.G. Mungal, and R.K. Hanson, 1993, "Compressibility Effects in a Reacting Mixing Layer," AIAA-93-1771.

- Oster, D. and I. Wygnanski, 1982, "The Forced Mixing Layer Between Parallel Streams," *Journal of Fluid Mechanics*, vol. 123. pp. 91-130.
- Papamoschou, D. and A. Roshko, 1986, "Observations of Supersonic Free Shear Layers," AIAA-86-0162.
- Samimy, M. and G.S. Elliott, 1990, "Effect of Compressibility on the Characteristics of Free Shear Layers," *AIAA Journal*, vol. 28, no. 3, pp. 439-445.
- Spencer, B.W. and B.G. Jones, 1971, "Statistical Investigation of Pressure and Velocity Fields in the Turbulent Two-Stream Mixing Layer," AIAA-71-613.
- Strahle, W.C. and S.G. Lekoudis, 1985, "Evaluation of Data on Simple Turbulent Reacting Flows," AFOSR-TR-85-0880. (Available as NTIS, AD-A170071.)
- Wallace, A.K., 1981, "Experimental Investigation on the Effects of Chemical Heat Release in the Reacting Turbulent Plane Shear Layer," Ph.D. Thesis, California Institute of Technology, Pasadena, CA. (Available as AFOSR-TR-84-0650.)

Table 1: Conditions of Related Planar Shear Layer Experiments

Source	Case	Φ	M_1	M_2	M_c	U_1 m/s	U_2 m/s	Time s	T_{01} K	T_{02} K	P kPa	r	s	Tools	Reactants	a_1 m/s	a_2 m/s	s, r^2	T_1 K	T_2 K
Goebel et al. (1990)	1	0.0	2.01	1.38	0.20	516	405	1127	295	295	46	0.79	0.76	LDV	air-air	257	294	0.469	163	214
	1d	0.0	2.02	1.39	0.20	499	393	751	275	275	55	0.79	0.76	LDV	air-air	247	283	0.471	151	198
	2	0.0	1.91	1.36	0.46	701	401	1076	578	295	49	0.57	1.55	LDV	air-air	367	295	0.506	334	215
	3	0.0	1.96	0.27	0.69	500	91	1108	285	285	53	0.18	0.57	LDV	air-air	255	337	0.019	161	281
	3r	0.0	2.22	0.43	0.72	562	143	859	315	285	53	0.25	0.58	LDV	air-air	253	333	0.038	159	275
Messersmith et al. (1991)	4	0.0	2.35	0.30	0.86	617	102	1829	360	290	36	0.16	0.60	LDV	air-air	263	339	0.016	171	285
	5	0.0	2.27	0.38	0.99	831	130	3459	675	300	32	0.16	1.14	LDV	air-air	366	343	0.028	332	292
		0.0	2.45	1.38	0.31	554	394	722	279	279	46	0.71	0.63	Mie Image	air-air	226	286	0.318	127	202
		0.0	2.44	0.38	0.62	549	156	1772	275	430	37	0.28	0.25	Mie Image	air-air	225	411	0.020	126	418
		0.0	2.45	0.43	0.74	554	142	1405	279	279	36	0.25	0.47	Mie Image	air-air	226	329	0.029	127	269
Clemens and Mungal (1992)	1	0.0	1.64	0.91	0.28	430	275	30	265	260	67	0.64	0.77	Mie, Sch	air-air	264	300	0.315	172	223
	2	0.0	1.97	0.42	0.62	480	130	30	265	260	66	0.27	0.59	Mie, Sch	air-air	245	318	0.043	149	251
	3	0.0	2.15	0.38	0.79	508	110	30	265	260	61	0.22	0.77	Mie, Sch	air-Ar	236	298	0.036	138	248
Miller et al. (1993)		1.05	1.25	0.32	0.35	910	310	30	1600	280	98	0.34	0.67	Mie, Sch	air-H ₂ /He	727	983	0.078	1276	271
		1.05	1.25	0.43	0.70	910	150	30	1600	280	92	0.17	4.51	Mie, Sch	air-H ₂ /N ₂	727	352	0.124	1276	270
Samimy and Elliott (1990)	1	0.0	1.83	0.51	0.51	484	170	808	291	291	52	0.35	0.64	LDV	air-air	264	333	0.079	174	277
	2	0.0	1.96	0.37	0.64	504	125	921	291	291	43	0.25	0.58	LDV	air-air	257	337	0.036	165	283
	3	0.0	3.01	0.45	0.86	597	155	3255	276	291	71	0.25	0.35	LDV	air-air	198	335	0.022	98	280
Hall (1991)	1	0.0	1.50	0.35	0.96	1156	111		300	300	195	0.10	5.95	Sch, T	He-Ar	771	316	0.054	171	288
	2	0.0	1.48	0.30	0.91	1147	105		300	300	201	0.09	4.12	Sch, T	He-N ₂	775	350	0.035	173	295
	3	0.0	1.46	0.29	0.51	432	102		300	300	228	0.24	0.71	Sch, T	N ₂ -N ₂	296	350	0.039	210	295
	4	0.0	1.48	0.44	0.43	436	164		300	300	222	0.38	0.74	Sch, T	N ₂ He/Ar	294	373	0.105	209	282
	5	0.0	1.48	0.42	0.34	436	194		300	300	222	0.45	0.48	Sch, T	N ₂ -He/Ar	294	462	0.096	209	283
	6	0.0	1.47	0.36	0.29	434	199		300	300	225	0.46	0.34	Sch, T	N ₂ -He/Ar	295	554	0.071	209	288
	7	0.0	1.48	0.28	0.24	436	204		300	300	222	0.47	0.19	Sch, T	N ₂ -He/Ar	294	730	0.043	209	292
	8	0.0	1.48	0.23	0.17	436	232		300	300	222	0.53	0.10	Sch, T	N ₂ -He	294	1011	0.029	209	295
	9	0.0	1.50	0.23	0.11	365	232		300	300	195	0.64	0.06	Sch, T	Ar-He	244	1011	0.024	171	295
	10	0.0	0.59	0.27	0.14	201	103		300	300	625	0.51	0.96	Sch, T	N ₂ -He/Ar	341	380	0.249	280	293
	11	0.0	0.65	0.10	0.09	220	102		300	300	595	0.46	0.13	Sch, T	N ₂ -He	339	1018	0.028	277	299
	3a	R	1.46	0.29	0.51	434	101		300	300	228	0.23	0.72	Sch, T	H ₂ /NO-F ₂ in	297	350	0.039	210	295
	3b	R	1.46	0.29	0.51	436	101		300	300	228	0.23	0.73	Sch, T		298	349	0.039	210	295
	3c	R	1.46	0.29	0.51	440	101		300	300	228	0.23	0.75	Sch, T	N ₂ -N ₂	301	348	0.039	210	295

Table 1: (Continued)

Source	Case	Φ	M_1	M_2	M_c	U_1 m/s	U_2 m/s	Time s	T_{01} K	T_{02} K	P kPa	r	s	Tools	Reactants	a_1 m/s	a_2 m/s	$s.r.^2$	T_1 K	T_2 K
Hall (1991)	3d	R	1.46	0.29	0.51	449	101		300	300	228	0.23	0.78	Sch,T	..	307	349	0.039	210	295
	3e	R	1.46	0.29	0.51	436	100		300	300	228	0.23	0.75	Sch,T	..	298	345	0.039	210	295
	2a	R	1.48	0.30	0.91	1143	105		300	300	201	0.09	4.12	Sch,T	H ₂ /NO-F ₂ in He-N ₂	773	349	0.035	173	295
	2b	R	1.48	0.30	0.91	1149	105		300	300	201	0.09	4.13	Sch,T	..	776	350	0.035	173	295
	2c	R	1.48	0.30	0.91	1155	105		300	300	201	0.09	4.18	Sch,T	..	780	350	0.035	173	295
	1a	R	1.50	0.35	0.96	1173	111		300	300	195	0.09	6.11	Sch,T	H ₂ /NO-F ₂ in He-Ar	782	316	0.054	171	288
Hermanson (1985)	1b	R	1.50	0.35	0.96	1155	111		300	300	195	0.10	5.91	Sch,T	..	770	317	0.054	171	288
	32	0.0	0.066	0.026	0.02	21.8	8.6		300	300	100	0.39	1.00	T,V	N ₂ -N ₂	353	353	0.153	300	300
	34	1.0	0.061	0.024	0.018	22.7	8.8		300	300	100	0.39	1.01	T,V	1%H ₂ -1%F ₂	355	352	0.152	300	300
	35	2.0	0.066	0.026	0.020	22.7	8.9		300	300	100	0.39	1.02	T,V	2%H ₂ -1%F ₂	356	352	0.157	300	300
	37	8.0	0.061	0.024	0.018	23.2	8.8		300	300	100	0.38	1.08	T,V	8%H ₂ -1%F ₂	367	352	0.155	300	300
	38	4.0	0.066	0.026	0.020	22.9	9.0		300	300	100	0.39	1.04	T,V	4%H ₂ -1%F ₂	360	352	0.161	300	300
	88	8.0	0.061	0.024	0.018	24.0	8.8		300	300	100	0.37	1.18	T,V	16%H ₂ -2%F ₂	383	352	0.158	300	300
	90	2.0	0.066	0.026	0.020	22.0	8.2		300	300	100	0.37	1.05	T,V	4%H ₂ -2%F ₂	360	352	0.146	300	300
	91	1.0	0.061	0.024	0.018	20.9	8.2		300	300	100	0.39	1.04	T,V	3%H ₂ -3%F ₂	358	351	0.160	300	300
	119	1.0	0.066	0.026	0.020	21.1	8.3		300	300	100	0.39	1.07	T,V	5%H ₂ -5%F ₂	362	350	0.165	300	300
	123	4.0	0.061	0.024	0.018	21.2	7.9		300	300	100	0.37	1.00	T,V	16%H ₂ -4%F ₂	383	351	0.139	300	300
	125	1.0	0.066	0.026	0.020	21.0	8.0		300	300	100	0.38	1.03	T,V	2%H ₂ -2%F ₂	356	352	0.148	300	300
	130	1.0	0.061	0.024	0.018	21.2	8.1		300	300	100	0.38	1.00	T,V	6%H ₂ -6%F ₂	363	349	0.146	300	300
	150	2.0	0.066	0.026	0.020	21.5	8.1		300	300	100	0.38	1.00	T,V	8%H ₂ -4%F ₂	367	351	0.143	300	300
	152	4.0	0.061	0.024	0.018	21.6	8.3		300	300	100	0.36	1.00	T,V	8%H ₂ -2%F ₂	367	352	0.147	300	300
	157	2.0	0.066	0.026	0.020	21.9	8.0		300	300	100	0.44	1.05	T,V	12%H ₂ -6%F ₂	375	349	0.132	300	300
	96	1.0	0.061	0.024	0.018	23.0	10.2		300	300	100	0.48	1.03	T,V	4%H ₂ -4%F ₂	360	351	0.209	300	300
	97	1.0	0.066	0.026	0.020	22.8	10.9		300	300	100	0.48	1.03	T,V	2%H ₂ -2%F ₂	356	352	0.235	300	300
	156	1.0	0.061	0.024	0.018	22.3	10.3		300	300	100	0.46	1.00	T,V	6%H ₂ -6%F ₂	363	349	0.213	300	300
Papamoschou and Roshko (1986)		0.0	3.30	1.90	0.30	654	511	1.5	300	300	14	0.78	0.54	Sch	N ₂ -N ₂	198	269	0.331	94	174
		0.0	2.00	3.30	0.77	1335	654	1.5	300	300	14	0.49	9.53	Sch	He-N ₂	667	198	2.286	129	94
		0.0	4.00	0.40	0.80	512	126	1.5	300	300	8	0.25	0.17	Sch	Ar-Ar	128	314	0.010	47	285
		0.0	2.30	3.50	0.90	1410	665	1.5	300	300	10	0.47	8.74	Sch	He-N ₂	613	190	1.945	109	87
		0.0	3.00	3.00	1.21	1529	633	1.5	300	300	22	0.41	4.90	Sch	He-N ₂	510	211	0.840	75	107
		0.0	4.00	1.90	1.57	1620	511	1.5	300	300	8	0.32	1.90	Sch	He-N ₂	405	269	0.189	47	174
Brown and Roshko (1974)		0.0	0.005	0.004	3E-4	5.0	1.4		300	300	404	0.28	10.0	Sch	He-Ar	1019	322	0.784	300	300

Table 1: (Concluded)

Source	Case	Φ	M_1	M_2	M_c	U_1 m/s	U_2 m/s	Time s	T_{01} K	T_{02} K	P kPa	r	s	Tools	Reactants	a_1 m/s	a_2 m/s	$s_1 r^2$	T_1 K	T_2 K
Wallace (1981)		0.07	0.014	0.028	25	5	3		300	300		0.20	1.00	V, Image	NO/N ₂ -O ₃ /N ₂	353	353	0.040	300	300
Chang et al. (1993)	0	0.72	0.39	0.29		394	134	2400	820	300	98	0.34	2.55	Sch, V, T	air-air	548	343	0.295	743	291
	1.6	0.71	0.30	0.26		390	137	2100	820	300	104	0.35	2.46	Sch, V, T	air-H ₂ /N ₂	549	350	0.303	745	295
Oster and Wygnanski (1982)	0.0	0.039	0.012	0.014		13.5	4.0	cont	300	300	101	0.30	1.00		air-air	348	348	0.090	300	300
	0.0	0.039	0.016	0.012		13.5	5.4	cont	300	300	101	0.40	1.00		air-air	348	348	0.160	300	300
	0.0	0.039	0.019	0.010		13.5	6.7	cont	300	300	101	0.50	1.00		air-air	348	348	0.250	300	300
	0.0	0.039	0.019	0.010		13.5	6.7	cont	300	300	101	0.50	1.00		air-air	348	348	0.250	300	300
Spencer and Jones (1971)	0.0	0.039	0.052	-0.006		30.0	18.0	cont	300	300	101	0.60	1.00		air-air	348	348	0.360	300	300
	0.0	0.039	0.026	0.007		30.0	9.0	cont	300	300	101	0.30	1.00		air-air	348	348	0.090	300	300

Notes:

1. These parameters are gathered from known references. Derived and estimated values are shown in italic. Unknown are left blank.
2. Ratios: $r=U_2/U_1$, speed ratio; $s=p_2/p_1$, density ratio; $s_1 r^2$, momentum flux ratio.
3. Tools are diagnostic techniques used. Mie, Mie scattering; Sch, Schlieren imaging, T, temperature measurement; V, LDV.
4. T_{01} and T_{02} are total temperatures in the air and fuel streams, respectively.

Table 2: Laser Doppler Velocimetry System Characteristics

Item	Blue	Green
Transmission parameters:		
Wavelength, mm	488.0	514.5
Component direction	u	v
Beam diameter, mm	1.5	1.5
Beam splitter type	compound crystal	compound crystal
Beam spacing, mm	50	50
Frequency shift, MHz	40	40
Effective shift, MHz	0	10
Shift mechanism	Bragg cell	Bragg cell
Power split, %	60-40	50-50
Frindge width, μm	5.86	6.18
Minor axis dia., μm	250	262
Major axis length, μm	6000	6300
No. of fringes	42	42
Focus lens focal distance, mm	602	602
Receiving parameters:		
Scattering	10° forward off axis	10° forward off axis
Lens aperature	$f9$	$f11$
Lens focal length, mm	350	450
Counter processor setting:		
Lower freq. limit, MHz	20	2
Higher freq. limit, MHz	100	20
No. of cycles	8	8
Exponent	1	3
Validation variation limit, %	7	7
Filter gain	1 to 2	1 to 2

Table 3: Flow Conditions

Nominal values	Nonreacting	Reacting
Air stream flow rate, kg/s	1.87 at 824 K	1.94 at 817 K
Fuel stream air flow rate, kg/s	1.62 at 303 K	----
Fuel stream N ₂ flow rate, kg/s	----	1.00 at 348 K
Fuel stream H ₂ flow rate, kg/s	----	0.032 at 348 K
Pressure, Pa	1.000 x10 ⁵	1.063 x10 ⁵
Upper flapper angle, deg	Parallel	1.3 divergent
Lower flapper angle, deg	Parallel	1.3 divergent
Measured and derived values*		
Air speed, U ₁ , m/s	394	390
Fuel speed, U ₂ , m/s	134	137
Air side density, ρ_1 , kg/m ³	0.46	0.50
Fuel side density, ρ_2 , kg/m ³	1.18	0.74
Air stream Mach no., M ₁	0.72	0.71
Fuel stream Mach no., M ₂	0.39	0.30
Air stream sonic speed, a ₁ , m/s	547	549
Fuel stream sonic speed, a ₂ , m/s	343	457
Air stream molecular weight, Mo ₁ , g/mole	28.8	28.8
Fuel stream molecular weight, Mo ₂ , g/mole	28.8	20.3
Speed ratio, $r=U_2/U_1$	0.34	0.34
Density ratio, $s=\rho_2/\rho_1$	2.57	1.48
Mass flux ratio, $(\rho_2 U_2)/(\rho_1 U_1)$	0.87	0.51
Momentum flux ratio, $(\rho_2 U_2^2)/(\rho_1 U_1^2)$	0.30	0.18
Convective Mach number, M _c	0.29	0.26
Equal volume. equivalenc. ratio, Φ^\dagger	0	1.60
Layer spreading angles, deg.:		
Measured	6.1	8.1
Projected	5.5	4.9
$\Delta U/U_m$	0.98	0.98
$\Delta T_{max}/T_{mean}$	0	1.46
Data rate, kHz	3 to 18	2 to 16
Sampling time, s	2	4

*Derived values are in *italic* form.

[†]Equal volume equivalence ratio: Ratio of the actual fuel-to-air ratio to that of the stoichiometric mixture based on two equal unit volumes of gases at the inlet temperatures, pressures, and species concentrations.

Table 4: Nonreacting Planar Shear Layer Velocimetry Statistics

File Title	x mm	y mm	U m/s	V m/s	u' m/s	v' m/s	R_{uv}	f_u Hz	f_v Hz
9205270059	75.0	25.0	131.33	3.0	2.1	2.2	0.0158	6572	13918
9205270060	75.0	20.0	131.57	2.7	2.2	1.8	0.0151	8081	14077
9205270061	75.0	15.0	132.17	1.5	2.9	2.3	-0.0026	9260	13852
9205270062	75.0	10.0	132.90	-0.3	4.2	3.8	0.0156	9901	13631
9205270063	75.0	8.0	133.42	-2.1	5.2	5.3	0.0219	7201	15262
9205270064	75.0	6.0	133.46	-2.1	7.1	5.9	0.0230	6637	16134
9205270065	75.0	4.0	133.76	-2.0	10.5	7.4	0.0485	7814	17495
9205270066	75.0	2.0	141.80	-4.0	18.9	9.2	0.0467	6936	18288
9205270067	75.0	0.0	171.74	-6.1	34.4	10.8	0.0388	9598	18560
9205270068	75.0	-2.0	229.81	-9.7	49.4	13.3	0.0706	10333	17738
9205270069	75.0	-4.0	303.36	-11.5	50.6	14.9	0.0831	9289	17082
9205270070	75.0	-6.0	357.09	-8.4	34.0	14.3	0.0651	6740	15013
9205270071	75.0	-8.0	371.49	-2.4	21.0	10.3	-0.0016	5680	13209
9205270072	75.0	-10.0	373.18	0.7	13.3	7.9	-0.0086	3628	9380
9205270073	75.0	-15.0	373.27	1.8	14.6	8.1	-0.0195	3251	8094
9205270074	75.0	-20.0	373.76	-0.3	12.5	9.2	-0.0049	1644	3964
9205270075	75.0	-25.0	374.61	-2.5	12.8	10.0	-0.0101	1521	3570
9205270076	100.0	-25.0	371.09	-2.9	19.7	10.0	0.0339	1035	2695
9205270077	100.0	-20.0	371.82	0.6	14.6	9.2	-0.0105	2059	4660
9205270078	100.0	-15.0	372.04	2.3	15.4	8.1	-0.0160	3512	7726
9205270079	100.0	-13.0	372.12	1.6	15.5	8.0	-0.0481	2800	7116
9205270080	100.0	-10.4	371.54	-1.2	17.5	10.5	-0.0085	4363	10618
9205270081	100.0	-7.8	358.97	-8.6	31.4	15.2	0.0692	5294	12460
9205270082	100.0	-5.2	309.52	-11.6	50.4	15.6	0.0823	7358	15693
9205270083	100.0	-2.6	239.58	-8.9	50.7	13.5	0.0632	10121	17926
9205270084	100.0	0.0	173.97	-6.7	36.5	12.1	0.0460	8081	17209
9205270085	100.0	2.6	143.31	-3.9	20.2	10.3	0.0249	6853	16933
9205270086	100.0	5.2	133.09	-2.0	10.6	7.8	0.0399	6223	16804
9205270087	100.0	7.8	131.87	-2.1	7.4	6.3	0.0412	7517	16833
9205270088	100.0	10.4	131.48	-0.2	5.2	5.0	-0.0205	10214	14863
9205270089	100.0	13.0	131.02	0.8	4.3	4.0	-0.0332	10752	14991
9205270090	100.0	15.0	130.87	0.8	3.4	3.8	-0.0106	9741	15712
9205270091	100.0	20.0	130.51	2.4	2.6	2.6	-0.0245	9283	14889
9205270092	100.0	25.0	130.09	1.4	2.3	4.0	0.0096	6237	15728
9205270093	150.0	25.0	130.25	0.7	2.9	4.6	0.0337	6978	16716
9205270094	150.0	20.0	130.70	2.5	3.8	3.5	-0.0449	11946	16380
9205270095	150.0	18.0	130.65	1.8	4.5	4.2	-0.0371	12184	16777
9205270096	150.0	14.4	131.66	0.6	6.1	5.6	-0.0098	11998	16584
9205270097	150.0	10.8	132.46	-0.4	9.1	7.1	0.0438	10551	16765
9205270098	150.0	7.2	137.78	-2.2	14.7	8.9	0.0521	10859	17460
9205270099	150.0	3.6	152.98	-5.3	25.4	10.2	0.0351	8327	17584
9205270100	150.0	0.0	197.98	-6.8	42.9	11.6	0.0575	10119	18107
9205270101	150.0	-3.6	255.24	-10.4	52.0	15.1	0.0693	7168	14256
9205270102	150.0	-7.2	322.61	-7.8	46.1	15.1	0.1157	8144	14468
9205270103	150.0	-10.8	363.81	-3.3	27.1	13.7	0.0738	7872	13595
9205270104	150.0	-14.4	371.56	2.6	15.8	9.8	-0.0175	7682	13715
9205270105	150.0	-18.0	371.56	2.9	15.0	9.3	-0.0326	3536	7087
9205270106	150.0	-20.0	371.45	3.4	15.6	9.2	0.0170	3675	7305

Table 4: (Continued)

File Title	x mm	y mm	U m/s	V m/s	u' m/s	v' m/s	R_{uv}	f_u Hz	f_v Hz
9205270107	150.0	-25.0	371.98	2.1	13.5	9.6	-0.0016	2359	5378
9205270108	300.0	-34.0	365.69	2.3	0.3	3.3	-0.0293	33	187
9205270109	300.0	-27.2	381.68	3.0	10.2	10.3	-0.0031	875	1424
9205270110	300.0	-20.4	378.59	6.1	13.8	9.7	0.0262	9027	11639
9205270111	300.0	-13.6	358.97	-0.3	33.8	12.9	0.1094	8035	12328
9205270112	300.0	-6.8	305.68	-1.8	45.7	12.6	0.1151	11262	16045
9205270113	300.0	0.0	251.90	-4.2	42.3	12.5	0.1022	14742	16440
9205270114	300.0	6.8	207.31	-8.6	36.5	15.7	0.0600	18104	11457
9205270115	300.0	13.6	171.67	-3.7	27.9	12.3	0.0578	16671	14820
9205270116	300.0	20.4	150.15	0.0	19.2	9.8	0.0406	14771	16022
9205270117	300.0	27.2	137.13	1.0	12.7	7.8	0.0205	8738	15622
9205270118	300.0	34.0	132.61	-0.2	9.6	10.0	0.0556	1498	495
9205270119	330.0	35.0	132.95	1.4	11.8	9.0	-0.0174	1168	210
9205270120	330.0	25.0	145.05	0.5	18.2	8.0	0.0572	11168	17629
9205270121	330.0	15.0	175.45	-3.0	29.2	11.9	0.0669	16696	15737
9205270122	330.0	5.0	220.34	-4.9	38.4	12.4	0.0554	13395	16105
9205270123	330.0	0.0	252.02	-3.2	42.6	11.6	0.0700	10764	16882
9205270124	330.0	-5.0	281.63	-2.3	45.8	11.1	0.0610	7221	15717
9205270125	330.0	-15.0	355.31	-1.5	37.7	12.2	0.0787	3071	9550
9205270126	330.0	-25.0	381.83	-1.9	15.0	13.8	0.0619	598	1586
9205270127	330.0	-35.0	382.36	-0.1	8.7	11.9	0.0959	494	1369
9205270128	0.0	-25.0	396.11	0.3	8.4	12.8	-0.0231	939	994
9205270129	0.0	-20.0	393.22	2.2	9.0	12.9	-0.0152	1408	1121
9205270130	0.0	-15.0	390.82	1.5	9.8	12.7	0.0051	1585	1940
9205270131	0.0	-10.0	387.67	4.2	8.0	12.0	-0.0179	4543	6358
9205270132	0.0	-5.0	384.92	6.7	8.6	10.4	-0.0010	4101	11077
9205270133	5.2	-3.0	377.98	6.7	7.7	7.0	0.0117	7677	16273
9205270134	5.5	-2.4	376.49	6.6	9.7	7.3	0.0386	5238	14115
9205270135	5.7	-1.8	371.69	5.8	12.4	6.4	0.0353	7901	17378
9205270136	5.9	-1.2	356.85	3.5	24.3	8.6	0.0152	5993	14508
9205270137	6.0	-0.6	321.07	2.1	33.4	9.2	0.0047	7723	15952
9205270138	6.0	0.0	272.44	-0.4	39.6	9.8	0.0025	10094	16066
9205270139	6.0	0.6	188.83	-0.5	47.1	9.1	0.0247	9728	18269
9205270140	5.9	1.2	118.94	2.6	21.7	8.0	0.0195	2026	18748
9205270141	5.7	1.8	115.04	0.5	8.1	8.0	-0.0127	1362	16806
9205270142	5.5	2.4	125.30	-1.8	10.8	6.3	0.0015	129	16322
9205270143	0.0	5.0	134.86	-1.5	3.4	8.9	-0.0104	2908	11955
9205270144	0.0	10.0	134.90	-0.8	3.1	3.7	0.0597	6397	11018
9205270145	0.0	15.0	133.60	-0.1	2.7	2.4	0.0009	7379	6008
9205270146	0.0	20.0	134.32	0.8	2.2	2.0	0.0260	7109	9079
9205270147	0.0	25.0	134.87	1.2	2.2	4.5	0.0085	4703	15129
9205270148	25.0	25.0	133.76	2.7	2.1	4.5	0.0290	3872	14376
9205270149	25.0	20.0	133.84	3.1	2.3	3.7	0.0188	6250	14610
9205270150	25.0	15.0	134.01	2.3	2.7	3.4	0.0181	7200	12712
9205270151	25.0	10.0	134.77	0.6	3.1	4.2	0.0348	6124	12783
9205270152	25.0	5.0	135.71	-1.0	4.5	6.0	-0.0135	2890	13606
9205270153	25.0	4.0	134.86	-1.3	5.0	5.6	0.0045	1625	12930
9205270154	25.0	3.0	133.82	-1.2	5.5	6.4	0.0054	2653	12903
9205270155	25.0	2.0	130.40	0.3	12.6	7.7	-0.0073	5795	18269

Table 4: (Concluded)

File Title	x mm	y mm	U m/s	V m/s	u' m/s	v' m/s	R_{uv}	f_u Hz	f_v Hz
9205270156	25.0	1.0	140.80	-2.2	23.6	10.8	0.0071	6114	15299
9205270157	25.0	0.0	188.76	-5.2	44.0	12.1	0.0150	7600	14972
9205270158	25.0	-1.0	263.01	-10.2	48.8	13.2	0.0264	6896	11619
9205270159	25.0	-2.0	335.94	-8.4	41.0	13.5	0.0137	4539	8436
9205270160	25.0	-3.0	371.43	-2.1	14.6	9.6	0.0130	1907	4522
9205270161	25.0	-4.0	375.09	0.2	11.1	8.2	0.0047	1246	3161
9205270162	25.0	-5.0	376.49	1.4	7.3	8.9	-0.0133	2403	4729
9205270163	25.0	-10.0	378.96	-0.1	8.2	10.9	0.0191	1146	1645
9205270164	25.0	-15.0	381.09	-1.6	5.8	11.2	-0.0832	407	617
9205270165	25.0	-20.0	382.53	2.8	6.7	9.7	-0.0435	795	1945
9205270166	25.0	-25.0	384.56	0.8	7.3	10.5	0.0915	350	923
9205270167	50.0	-25.0	379.17	0.1	5.8	8.9	-0.0043	215	808
9205270168	50.0	-20.0	376.66	-1.1	13.9	10.2	0.0907	300	638
9205270169	50.0	-15.0	377.23	0.8	14.8	10.2	0.0475	261	651
9205270170	50.0	-10.0	375.35	1.9	8.4	8.6	-0.0216	959	3356
9205270171	50.0	-8.0	375.30	0.4	8.4	8.1	0.0098	940	2991
9205270172	50.0	-6.4	375.42	-1.1	8.9	8.9	-0.0529	1154	4080
9205270173	50.0	-4.8	369.33	-8.1	23.3	13.7	0.0701	1566	4890
9205270174	50.0	-3.2	315.19	-10.6	49.7	14.7	0.0387	6456	13544
9205270175	50.0	-1.6	238.99	-3.6	46.7	11.1	0.0541	13906	18369
9205270176	50.0	0.0	168.03	-5.4	34.0	12.4	0.0278	6812	15945
9205270177	50.0	1.6	138.47	-2.2	15.5	10.0	0.0152	5743	15265
9205270178	50.0	3.2	134.73	-1.6	7.6	7.7	0.0238	3756	12956
9205270179	50.0	4.8	134.38	-1.2	5.1	5.6	0.0249	4086	14001
9205270180	50.0	6.4	134.63	-0.8	4.7	5.4	0.0087	5103	14783
9205270181	50.0	8.0	134.52	-0.7	3.9	6.1	0.0317	6050	14842
9205270182	50.0	10.0	134.06	0.2	3.1	4.9	0.0314	6335	13859
9205270183	50.0	15.0	133.20	2.2	2.6	3.6	0.0395	7182	13890
9205270184	50.0	20.0	132.73	3.1	2.3	3.3	0.0223	6494	14825
9205270185	50.0	25.0	132.47	2.8	2.2	5.1	0.0010	3128	12405

Table 5: Reacting Planar Shear Layer Velocimetry Statistics

File Title	x mm	y mm	U m/s	V m/s	u' m/s	v' m/s	R_{uv}	f_u Hz	f_v Hz
9206100001	0.0	-27.8	378.74	16.1	24.2	13.3	-0.0993	13717	9957
9206100002	0.0	-22.8	385.83	12.1	21.1	18.4	-0.0081	9131	3907
9206100003	0.0	-17.8	390.92	10.5	22.7	18.5	-0.0097	4375	2247
9206100004	0.0	-12.8	392.75	13.9	26.3	17.2	-0.0245	6306	2897
9206100005	0.0	-7.8	398.81	16.9	28.7	16.0	-0.0129	6095	2871
9206100006	5.2	-5.8	400.90	18.4	28.5	16.7	-0.0213	8208	3773
9206100007	5.5	-5.2	398.80	20.5	33.7	14.6	-0.0121	10713	5458
9206100008	5.7	-4.6	398.08	20.8	39.7	13.8	0.0000	0	5859
9206100009	5.9	-4.0	394.53	21.3	39.7	14.1	-0.0581	13999	7344
9206100010	6.0	-3.4	396.46	22.2	38.0	13.9	-0.0375	13220	5750
9206100011	6.0	-2.8	392.42	9.4	37.1	19.7	-0.0358	12530	3600
9206100012	6.0	-2.2	384.87	-11.1	37.3	18.9	-0.0197	13889	2755
9206100013	5.9	-1.6	359.61	-12.9	41.4	13.6	-0.0015	16453	5762
9206100014	5.7	-1.0	330.34	-13.4	43.0	13.4	0.0036	13575	5680
9206100015	5.5	-0.4	199.19	-35.0	34.9	0.1	-0.0625	1928	2126
9206100016	0.0	2.2	132.79	-3.6	9.5	11.4	-0.0081	7767	11112
9206100017	0.0	7.2	137.48	1.6	6.8	4.3	0.0025	9348	14493
9206100018	0.0	12.2	137.43	1.0	6.3	3.7	-0.0052	10227	9167
9206100019	0.0	17.2	137.41	2.0	5.9	2.4	-0.0283	8573	7077
9206100020	0.0	22.2	139.06	3.1	6.1	2.0	-0.0379	9176	11491
9206100021	25.0	22.2	135.11	6.3	6.0	2.2	-0.0399	9463	12906
9206100022	25.0	17.2	134.14	5.7	6.0	2.7	-0.0228	9478	9471
9206100023	25.0	12.2	134.57	4.9	6.5	4.0	-0.0320	9673	9847
9206100024	25.0	7.2	135.70	6.4	7.6	4.8	-0.0894	12103	15277
9206100025	25.0	2.2	152.97	15.3	22.7	10.3	0.0761	18794	17236
9206100026	25.0	1.2	203.58	13.4	40.7	11.0	0.0858	18807	18340
9206100027	25.0	0.2	289.36	13.8	44.8	12.3	0.0626	19009	17206
9206100028	25.0	-0.8	348.81	15.7	40.9	13.0	0.0607	18440	16713
9206100029	25.0	-1.8	377.61	19.0	35.4	13.3	-0.0106	14964	12739
9206100030	25.0	-2.8	377.48	19.2	37.5	12.0	-0.0701	17582	16610
9206100031	25.0	-3.8	382.10	18.0	35.7	11.8	-0.1130	17067	17867
9206100032	25.0	-4.8	386.41	16.9	33.2	11.9	-0.1336	15021	18223
9206100033	25.0	-5.8	386.92	17.0	31.1	12.9	-0.1332	14391	17681
9206100034	25.0	-6.8	381.52	16.6	33.7	13.5	-0.1433	15868	17272
9206100035	25.0	-7.8	373.78	16.8	37.4	14.1	-0.1396	16598	15712
9206100036	25.0	-12.8	375.66	14.3	31.3	14.4	-0.1481	15113	17684
9206100037	25.0	-17.8	374.50	13.5	25.6	13.3	-0.1295	12615	14833
9206100038	25.0	-22.8	370.24	12.3	24.3	11.8	-0.0849	12287	10500
9206100039	25.0	-27.8	370.50	9.9	22.9	9.8	-0.0841	10231	14408
9206100040	50.0	-27.8	360.14	4.9	24.2	10.7	-0.0400	11050	8483
9206100041	50.0	-22.8	366.51	8.6	23.8	10.8	-0.0995	10239	14904
9206100042	50.0	-17.8	366.73	11.0	26.6	12.7	-0.1275	13614	16114
9206100043	50.0	-12.8	370.86	12.3	28.1	13.7	-0.1672	14882	17953
9206100044	50.0	-10.8	375.62	12.3	28.5	13.5	-0.1551	13600	18651
9206100045	50.0	-9.2	372.66	13.2	30.5	14.1	-0.1752	15950	17779
9206100046	50.0	-7.6	375.95	13.4	31.6	13.8	-0.1563	15156	17690
9206100047	50.0	-6.0	385.95	13.6	24.5	14.9	-0.0513	4085	4483
9206100048	50.0	-4.4	378.45	15.3	33.0	13.9	-0.1299	14040	15565

Table 5: (Continued)

File Title	x mm	y mm	U m/s	V m/s	u' m/s	v' m/s	R_{uv}	f_u Hz	f_v Hz
9206100049	50.0	-2.8	370.32	15.0	37.6	12.3	-0.0490	17843	18073
9206100050	50.0	-1.2	363.09	15.2	39.6	13.8	0.0836	16409	14299
9206100051	50.0	0.4	322.40	13.2	48.0	14.0	0.1141	18013	15296
9206100052	50.0	2.0	254.01	12.2	46.6	13.8	0.0551	18942	13585
9206100053	50.0	3.6	194.99	13.2	38.8	12.3	0.0921	19165	16292
9206100054	50.0	5.2	151.84	13.6	25.0	10.8	0.1383	18548	16769
9206100055	50.0	7.2	132.14	11.4	11.5	8.7	-0.0045	16807	17262
9206100056	50.0	12.2	130.13	8.1	7.0	5.0	-0.1275	13207	14389
9206100057	50.0	17.2	129.79	7.8	6.3	3.5	-0.1002	11695	13744
9206100058	50.0	22.2	130.32	8.1	6.1	2.8	-0.0471	10615	14974
9206100059	75.0	22.2	123.84	9.2	6.3	4.0	-0.0838	12933	16014
9206100060	75.0	17.2	123.25	9.8	7.0	5.7	-0.1331	14439	15789
9206100061	75.0	12.2	125.39	11.5	10.4	8.9	-0.0516	16331	16513
9206100062	75.0	7.2	165.51	12.6	35.7	11.8	0.2074	18839	17611
9206100063	75.0	5.2	207.47	10.6	49.1	12.3	0.1742	17597	18503
9206100064	75.0	3.2	258.81	10.4	54.2	13.6	0.0902	16695	14931
9206100065	75.0	1.2	313.01	11.3	55.5	12.7	0.1293	14456	18709
9206100066	75.0	-0.8	355.23	14.2	45.1	13.4	0.0406	13888	15279
9206100067	75.0	-2.8	376.87	13.3	33.5	12.6	-0.0170	13583	18195
9206100068	75.0	-4.8	378.60	12.7	31.0	13.5	-0.1148	14375	17296
9206100069	75.0	-6.8	383.26	10.6	27.2	11.8	-0.0761	7806	19352
9206100070	75.0	-8.8	380.90	9.2	25.5	11.5	-0.0610	5882	19319
9206100071	75.0	-10.8	375.95	10.6	25.6	12.5	-0.0971	9559	19014
9206100072	75.0	-12.8	376.04	9.9	24.7	12.1	-0.0787	8383	19281
9206100073	75.0	-17.8	369.81	8.9	24.5	11.1	-0.0536	6124	18688
9206100074	75.0	-22.8	364.62	7.9	28.0	10.1	-0.0517	7262	15825
9206100075	75.0	-27.8	361.37	6.3	25.8	9.0	-0.0570	5572	11383
9206100076	100.0	-27.8	364.24	3.3	20.6	6.1	-0.0080	2216	18934
9206100077	100.0	-22.8	366.79	5.0	21.0	7.5	-0.0169	2573	18770
9206100078	100.0	-17.8	370.85	7.3	23.3	10.4	-0.0334	3790	18988
9206100079	100.0	-15.8	372.09	6.1	24.4	9.0	-0.0105	2887	19138
9206100080	100.0	-13.2	372.13	9.1	27.5	11.6	-0.0926	7991	18717
9206100081	100.0	-10.6	377.87	7.0	26.8	10.3	-0.0326	4253	19297
9206100082	100.0	-8.0	364.58	12.1	36.6	14.5	-0.1058	16466	11990
9206100083	100.0	-5.4	374.51	11.6	32.1	13.7	-0.1061	14163	16708
9206100084	100.0	-2.8	368.43	12.7	38.0	13.9	-0.0095	14839	15189
9206100085	100.0	-0.2	344.58	10.6	50.7	14.3	0.0888	13292	14969
9206100086	100.0	2.4	298.13	10.2	58.2	13.7	0.1490	14496	18283
9206100087	100.0	5.0	248.10	9.7	56.3	13.2	0.1443	15349	18376
9206100088	100.0	7.6	201.49	11.2	48.8	12.9	0.1902	16891	18009
9206100089	100.0	10.2	161.77	12.8	35.5	12.2	0.2072	17276	17299
9206100090	100.0	12.2	141.55	13.3	25.6	11.7	0.2094	17421	17325
9206100091	100.0	17.2	123.48	12.3	9.7	9.0	-0.0364	15552	16801
9206100092	100.0	22.2	122.29	10.7	7.5	6.1	-0.0126	13803	17209
9206100093	150.0	22.2	127.87	13.6	15.0	11.2	0.1395	15218	16574
9206100094	150.0	17.2	150.33	13.0	30.8	12.8	0.2015	16124	16470
9206100095	150.0	15.2	166.24	11.7	38.4	13.2	0.1967	14721	17589
9206100096	150.0	11.6	206.88	11.6	47.9	14.1	0.2125	18071	16356
9206100097	150.0	8.0	248.49	10.7	51.5	15.9	0.1460	17968	12922

Table 5: (Concluded)

File Title	x mm	y mm	U m/s	V m/s	u' m/s	v' m/s	R_{uv}	f_u Hz	f_v Hz
9206100098	150.0	4.4	292.68	10.9	52.4	16.1	0.1656	17168	13217
9206100099	150.0	0.8	328.29	13.1	49.0	15.9	0.1062	16036	10796
9206100100	150.0	-2.8	357.24	11.9	42.1	14.3	0.0514	12436	15150
9206100101	150.0	-6.4	362.13	11.6	39.3	14.1	-0.0484	13231	12370
9206100102	150.0	-10.0	367.28	11.2	33.0	14.4	-0.0648	9356	9032
9206100103	150.0	-13.6	370.34	8.5	30.7	12.2	-0.0956	10541	18775
9206100104	150.0	-17.2	371.83	7.5	23.9	10.7	-0.0242	4592	19066
9206100105	150.0	-20.8	369.74	7.8	21.9	10.0	-0.0427	4668	18876
9206100106	150.0	-22.8	364.74	8.3	24.2	10.8	-0.0646	8528	17131
9206100107	150.0	-27.8	363.85	7.4	20.7	8.9	-0.0479	5630	17857
9206100108	300.0	-36.8	366.88	10.3	22.5	7.7	-0.0208	10090	16912
9206100109	300.0	-30.0	366.47	9.9	26.0	9.8	-0.0401	12379	15895
9206100110	300.0	-23.2	372.91	9.2	26.9	11.1	-0.0752	12105	16658
9206100111	300.0	-16.4	373.92	8.7	29.0	11.9	-0.0397	11611	12883
9206100112	300.0	-9.6	372.58	9.7	32.5	13.7	-0.0038	15403	15070
9206100113	300.0	-2.8	365.20	10.9	37.2	14.1	0.1220	14894	17563
9206100114	300.0	4.0	336.30	10.3	46.2	15.8	0.1679	15317	15986
9206100115	300.0	10.8	294.55	8.7	49.2	16.8	0.1319	15959	13625
9206100116	300.0	17.6	254.77	8.8	47.8	15.1	0.2294	17111	18218
9206100117	300.0	24.4	214.20	9.4	42.4	14.4	0.2475	17779	18408
9206100118	300.0	31.2	176.76	10.5	32.9	13.4	0.2662	16939	18251
9206100119	330.0	37.2	166.55	-0.6	28.4	10.9	0.0256	15750	10682
9206100120	330.0	32.2	186.89	9.9	36.0	13.5	0.2713	16645	18802
9206100121	330.0	27.2	212.69	9.3	42.1	14.2	0.2543	16906	18810
9206100122	330.0	22.2	238.47	9.0	44.8	15.2	0.1910	16771	16408
9206100123	330.0	17.2	267.69	8.0	48.8	14.4	0.2099	15100	18949
9206100124	330.0	12.2	297.42	9.0	47.7	16.1	0.2165	17652	16129
9206100125	330.0	7.2	318.26	7.8	49.8	17.6	0.1201	13573	13602
9206100126	330.0	2.2	349.85	9.1	45.7	13.6	0.1375	11275	19019
9206100127	330.0	-2.8	364.93	10.2	38.8	14.2	0.0701	13882	15496
9206100128	330.0	-7.8	380.19	8.5	31.8	11.4	0.0181	8134	19228
9206100129	330.0	-12.8	384.31	8.4	28.0	11.1	-0.0294	9350	19079
9206100130	330.0	-17.8	381.23	7.8	27.6	11.2	-0.0510	9701	17593
9206100131	330.0	-22.8	381.02	8.2	24.4	9.5	-0.0485	6686	18692
9206100132	330.0	-27.8	370.52	8.8	29.3	9.9	-0.0262	9802	15185
9206100133	330.0	-32.8	372.62	9.1	23.3	8.3	-0.0290	8213	17664
9206100134	330.0	-37.8	369.80	10.0	22.9	7.7	-0.0078	8094	16984
9206100135	330.0	-40.0	366.12	9.6	24.8	7.7	0.0018	9122	15602

Table 6: Shear Layer Width Characteristics

	x mm	Nonreacting		Reacting	
		δ_w mm	y_c mm	δ_w mm	y_c mm
Velocity	300	31.9	-1.6	41.0	16.9
	150	13.5	-4.1	20.5	7.2
Thermal	300	37.6	8.7	54.2	9.4
	150	18.5	-5.1	29.4	-0.9
Prandtl number	300	0.85	-----	0.76	-----
	150	0.73	-----	0.70	-----

Table 7: Measured Temperature Distributions, K

x= 0 mm				x= 150 mm				x= 300 mm			
y	Air	Torch	Reacting	y	Air	Torch	Reacting	y	Air	Torch	Reacting
mm	K	K	K	mm	K	K	K	mm	K	K	K
36.00*	343.	350.	335.	36.00	343.	350.	335.	36.00	340.	410.	515.
35.00				35.00	343.	350.	335.	35.00	342.	421.	534.
34.00				34.00	343.	350.	335.	34.00	344.	434.	561.
33.00				33.00	343.	350.	335.	33.00	345.	444.	592.
32.00				32.00	343.	350.	334.	32.00	346.	455.	625.
31.00				31.00	343.	350.	335.	31.00	348.	464.	654.
30.00				30.00	343.	350.	336.	30.00	351.	472.	680.
29.00				29.00	344.	350.	335.	29.00	355.	481.	716.
28.00				28.00	343.	350.	335.	28.00	361.	490.	759.
27.00				27.00	343.	350.	336.	27.00	366.	501.	801.
26.00				26.00	344.	350.	336.	26.00	373.	511.	846.
25.00				25.00	343.	350.	336.	25.00	385.	520.	888.
24.00				24.00	344.	350.	337.	24.00	392.	530.	926.
23.00				23.00	344.	350.	338.	23.00	403.	538.	969.
22.00				22.00	344.	351.	339.	22.00	415.	548.	1011.
21.00				21.00	344.	351.	340.	21.00	424.	556.	1052.
20.00				20.00	344.	352.	342.	20.00	434.	564.	1094.
19.00				19.00	345.	354.	345.	19.00	445.	572.	1133.
18.00				18.00	345.	356.	347.	18.00	456.	580.	1177.
17.00				17.00	345.	359.	359.	17.00	468.	589.	1224.
16.00				16.00	346.	363.	378.	16.00	479.	597.	1266.
15.00				15.00	346.	368.	397.	15.00	491.	604.	1306.
14.00				14.00	347.	375.	431.	14.00	503.	611.	1341.
13.00				13.00	348.	386.	472.	13.00	514.	619.	1379.
12.00				12.00	349.	395.	546.	12.00	526.	627.	1413.
11.00				11.00	350.	411.	619.	11.00	538.	634.	1442.
10.00				10.00	352.	427.	693.	10.00	550.	641.	1469.
9.00				9.00	353.	447.	782.	9.00	562.	650.	1491.
8.00				8.00	355.	467.	878.	8.00	574.	658.	1510.
7.00				7.00	356.	492.	974.	7.00	586.	667.	1523.
6.00				6.00	360.	517.	1070.	6.00	598.	675.	1527.
5.00				5.00	365.	540.	1166.	5.00	610.	683.	1525.
4.00				4.00	374.	567.	1261.	4.00	622.	690.	1515.
3.00				3.00	385.	590.	1337.	3.00	634.	698.	1492.
2.00				2.00	398.	617.	1399.	2.00	646.	707.	1461.
1.00				1.00	413.	640.	1460.	1.00	658.	715.	1427.
0.00	802.	853.	1052.	0.00	436.	668.	1490.	0.00	670.	722.	1389.
-1.00	802.	896.	1052.	-1.00	460.	693.	1519.	-1.00	683.	729.	1354.

*Thermal expansion of the splitter plate tip prevented the thermocouple probe at $x=0$ mm from probing locations above the plate, from $x=26$ mm to $x=1.0$ mm. Since the flows in this region are unchanged throughout the duration of the experiments, and they are only affected by the upstream supply temperatures, these can be regarded as constants.

Table 7: (Concluded)

x= 0 mm				x= 150 mm				x= 300 mm			
y mm	Air Torch Reacting			y mm	Air Torch Reacting			y mm	Air Torch Reacting		
	K	K	K		K	K	K		K	K	K
-2.00	802.	956.	1060.	-2.00	487.	718.	1536.	-2.00	695.	737.	1320.
-3.00	802.	1016.	1070.	-3.00	513.	743.	1534.	-3.00	707.	744.	1286.
-4.00	802.	1076.	1073.	-4.00	537.	768.	1512.	-4.00	718.	752.	1249.
-5.00	802.	1091.	1074.	-5.00	563.	793.	1484.	-5.00	731.	760.	1217.
-6.00	802.	1087.	1074.	-6.00	587.	818.	1455.	-6.00	741.	767.	1188.
-7.00	802.	1080.	1069.	-7.00	614.	843.	1418.	-7.00	751.	774.	1159.
-8.00	802.	1073.	1064.	-8.00	641.	865.	1380.	-8.00	761.	781.	1131.
-9.00	802.	1065.	1059.	-9.00	665.	886.	1335.	-9.00	768.	787.	1103.
-10.00	802.	1055.	1051.	-10.00	687.	902.	1283.	-10.00	773.	793.	1078.
-11.00	802.	1042.	1045.	-11.00	708.	918.	1233.	-11.00	778.	799.	1053.
-12.00	802.	1035.	1038.	-12.00	727.	929.	1184.	-12.00	781.	806.	1032.
-13.00	802.	1028.	1032.	-13.00	744.	939.	1140.	-13.00	785.	813.	1011.
-14.00	802.	1018.	1022.	-14.00	758.	950.	1106.	-14.00	788.	818.	992.
-15.00	802.	1007.	1013.	-15.00	767.	955.	1075.	-15.00	790.	823.	977.
-16.00	802.	997.	1003.	-16.00	774.	958.	1055.	-16.00	791.	827.	964.
-17.00	802.	986.	992.	-17.00	780.	955.	1035.	-17.00	791.	831.	954.
-18.00	802.	975.	981.	-18.00	785.	954.	1018.	-18.00	791.	834.	943.
-19.00	802.	964.	970.	-19.00	787.	953.	1005.	-19.00	791.	835.	934.
-20.00	802.	953.	959.	-20.00	788.	950.	995.	-20.00	790.	837.	926.
-21.00	802.	941.	947.	-21.00	787.	945.	987.	-21.00	789.	838.	918.
-22.00	802.	930.	936.	-22.00	788.	940.	978.	-22.00	788.	838.	911.
-23.00	802.	919.	927.	-23.00	788.	934.	971.	-23.00	787.	837.	904.
-24.00	802.	907.	913.	-24.00	788.	927.	963.	-24.00	786.	837.	897.
-25.00	802.	896.	904.	-25.00	788.	921.	956.	-25.00	785.	835.	891.
-26.00	802.	886.	892.	-26.00	788.	914.	949.	-26.00	784.	832.	884.
-27.00	802.	875.	882.	-27.00	788.	907.	942.	-27.00	782.	829.	878.
-28.00	802.	865.	873.	-28.00	787.	900.	936.	-28.00	780.	827.	872.
-29.00	802.	854.	863.	-29.00	787.	893.	929.	-29.00	778.	824.	867.
-30.00	802.	845.	855.	-30.00	787.	886.	921.	-30.00	775.	822.	863.
-31.00	802.	836.	846.	-31.00	787.	878.	914.	-31.00	774.	819.	859.
-32.00	802.	829.	840.	-32.00	786.	872.	908.	-32.00	772.	815.	854.
-33.00	802.	822.	833.	-33.00	787.	865.	900.	-33.00	770.	810.	844.
-34.00	802.	816.	827.	-34.00	787.	859.	893.	-34.00	768.	803.	840.
-35.00	802.	810.	819.	-35.00	787.	853.	885.	-35.00	766.	796.	835.
-36.00	802.	805.	815.	-36.00	787.	847.	878.	-36.00	763.	789.	831.
-37.00	802.	802.	810.	-37.00	787.	841.	871.	-37.00	760.	782.	827.
-38.00	799.	799.	807.	-38.00	787.	837.	863.	-38.00	760.	782.	827.

Table 8: Microphone Measurement Intensities

Micro- phone	Date				<u>Mean</u>	<u>rms</u>	<u>Increase</u>
	93/5/18	93/5/25	93/6/11,15	93/6/17			
	rms noise levels, dB						
	<u>Air data</u>						
1	133.7	134.4	-----	-----	134.1	0.5	-----
2	148.5	147.9	144.2	142.4	145.8	2.9	-----
3	140.9	143.9	137.4	138.2	140.1	2.9	-----
5	-----	-----	132.7	133.7	133.2	0.5	-----
6	144.4	143.4	142.7	144.7	143.8	0.9	-----
7	150.9	152.8	149.4	151.7	151.2	1.4	-----
	<u>Torch Data</u>						
1	130.5	134.9	-----	-----	132.7	3.1	-----
2	147.1	147.9	139.5	137.4	143.0	5.3	-----
3	138.7	143.5	139.0	138.6	140.0	2.4	-----
5	-----	-----	136.5	137.4	137.0	0.6	-----
6	139.6	144.8	145.2	146.7	144.1	3.1	-----
7	144.0	153.8	151.3	149.9	149.8	4.2	-----
	<u>Combustion Data</u>						
1	140.0	140.6	-----	-----	140.3	0.4	2.04
2	157.0	155.2	145.7	147.3	151.3	5.6	4.88
3	143.2	142.1	138.0	140.1	140.9	2.3	1.1
5	-----	-----	141.9	144.5	143.2	1.8	3.16
6	153.1	152.9	151.6	152.6	152.6	0.7	2.75
7	154.9	156.0	154.7	155.5	155.3	0.6	1.43

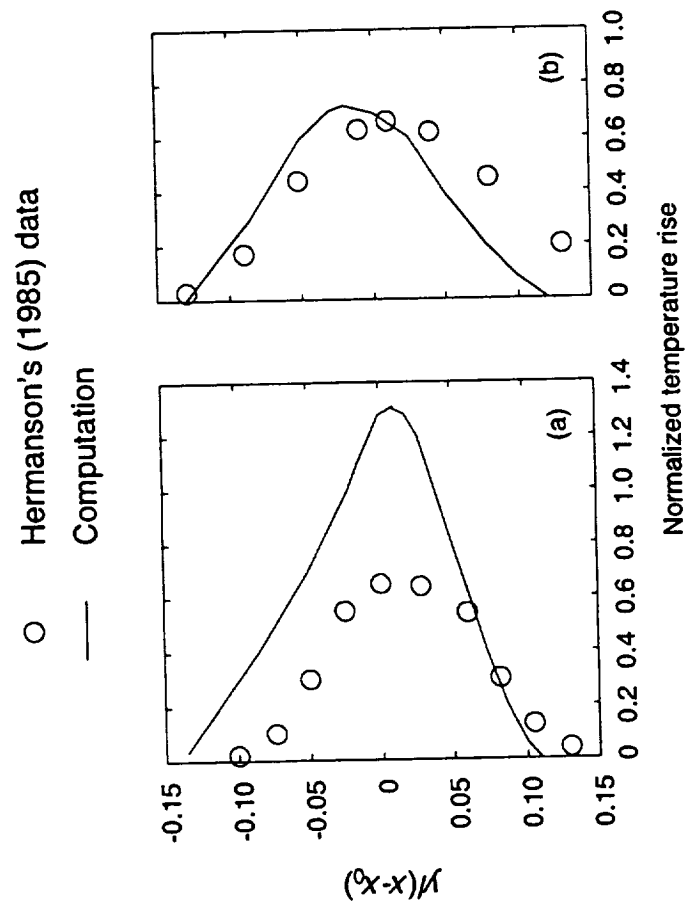


Figure 1. Computational fluid dynamics versus experiment:

(a) Claus (1986), eddy breakup model.

(b) Farshchi (1986), PDF model.

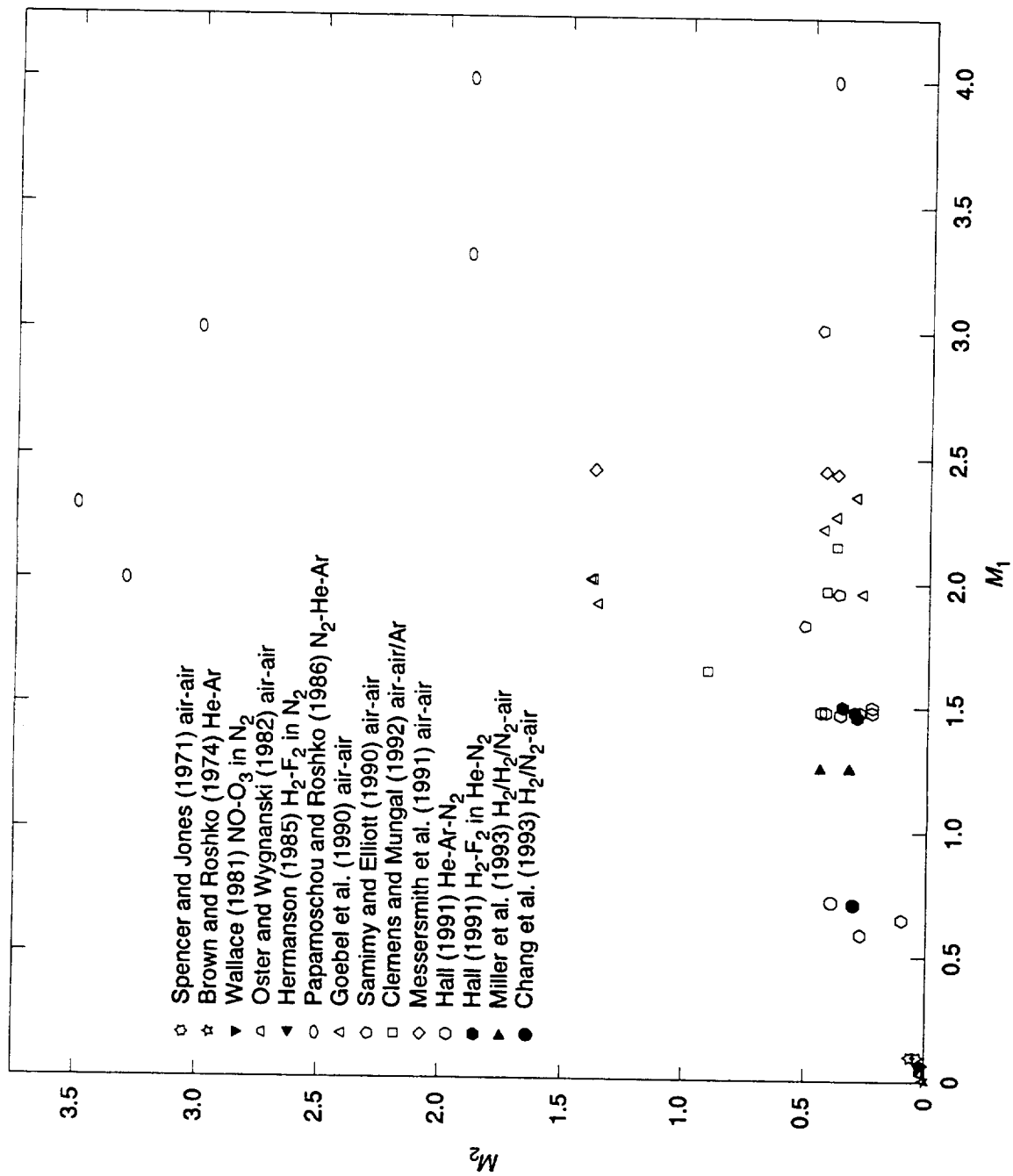


Figure 2. Mach number regimes of planar shear layer experiments.

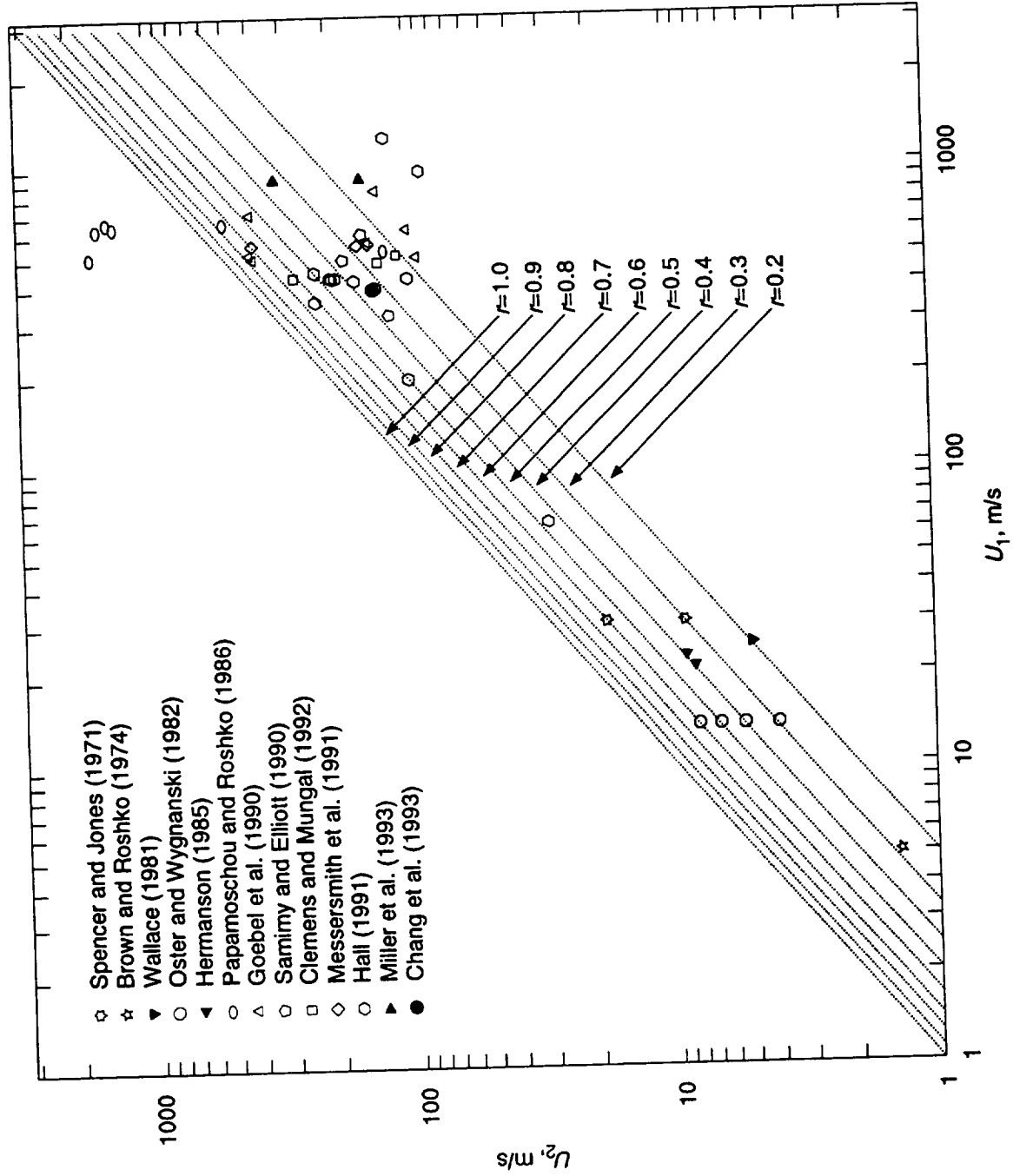


Figure 3. Absolute flow speed regimes of planar shear layer experiments. $r=U_2/U_1$.

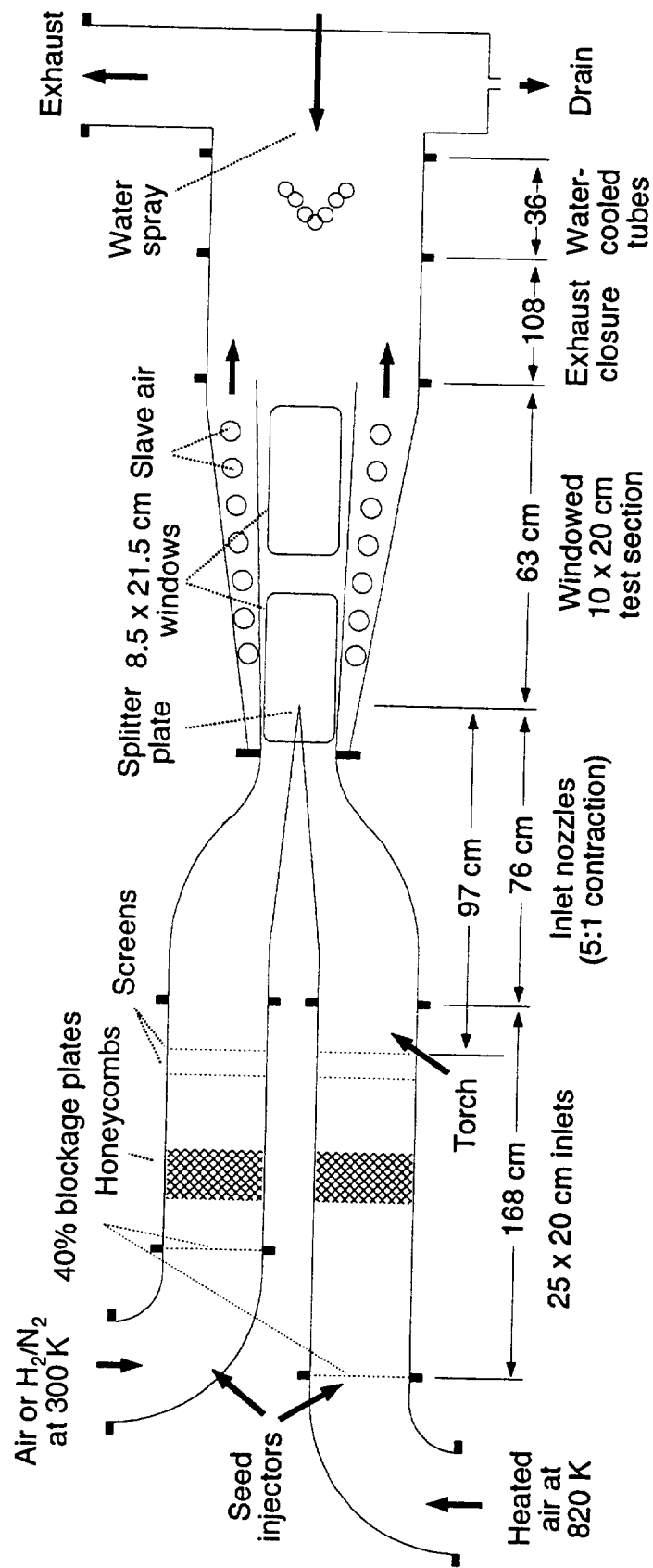


Figure 4. Schematic diagram of planar reacting shear layer wind tunnel.

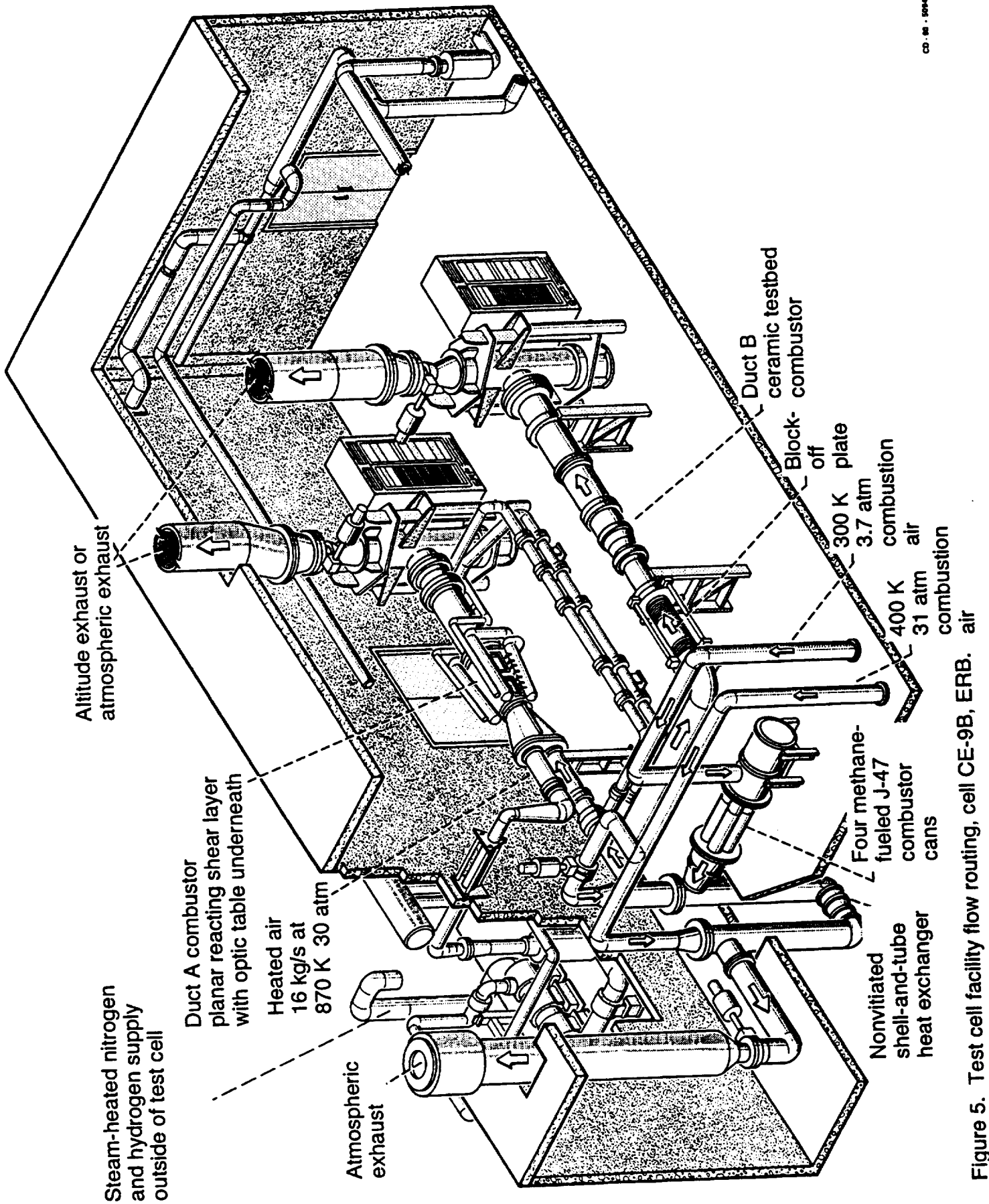


Figure 5. Test cell facility flow routing, cell CE-9B, ERB. air

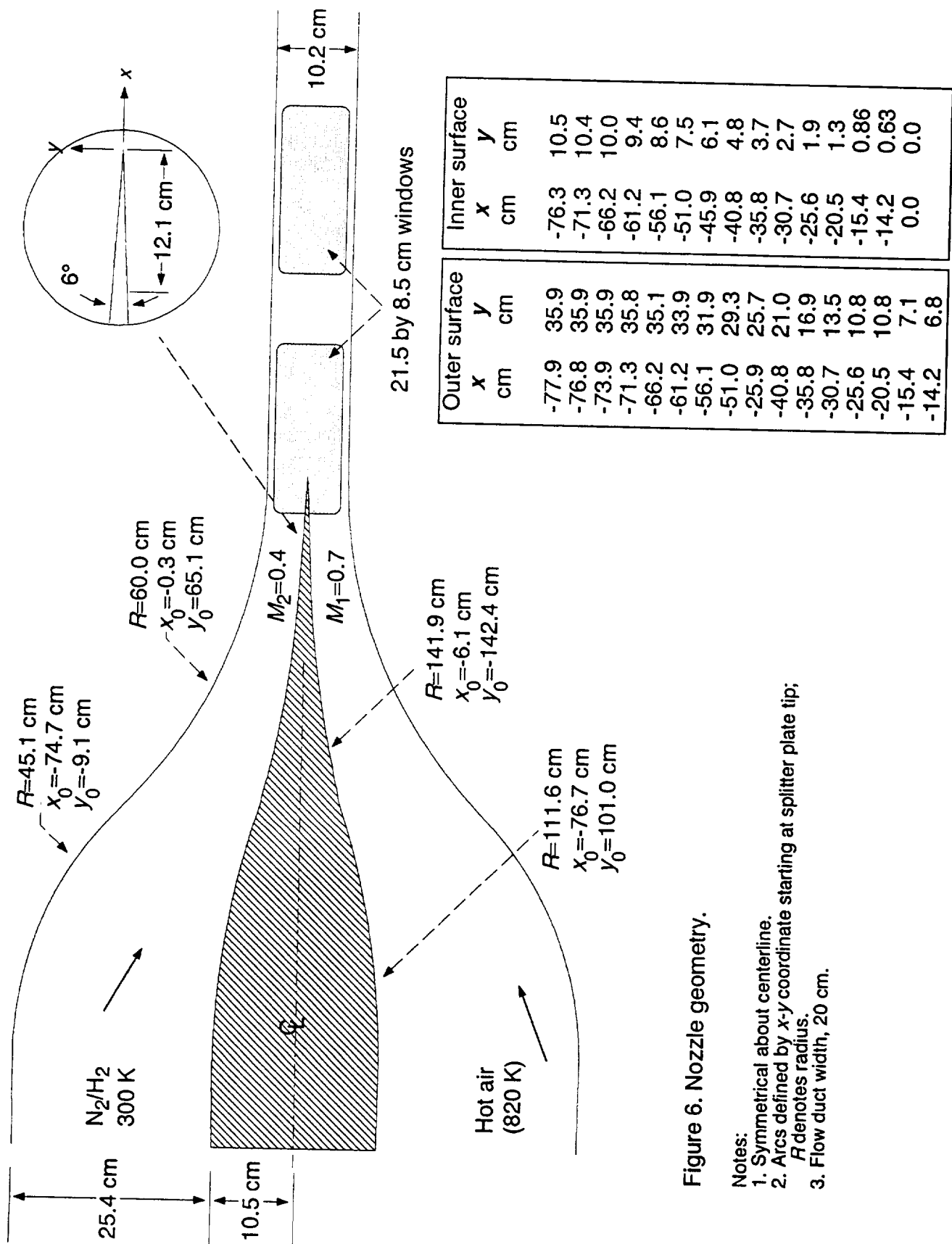


Figure 6. Nozzle geometry.

Notes:

1. Symmetrical about centerline.
2. Arcs defined by x-y coordinate starting at splitter plate tip; R denotes radius.
3. Flow duct width, 20 cm.

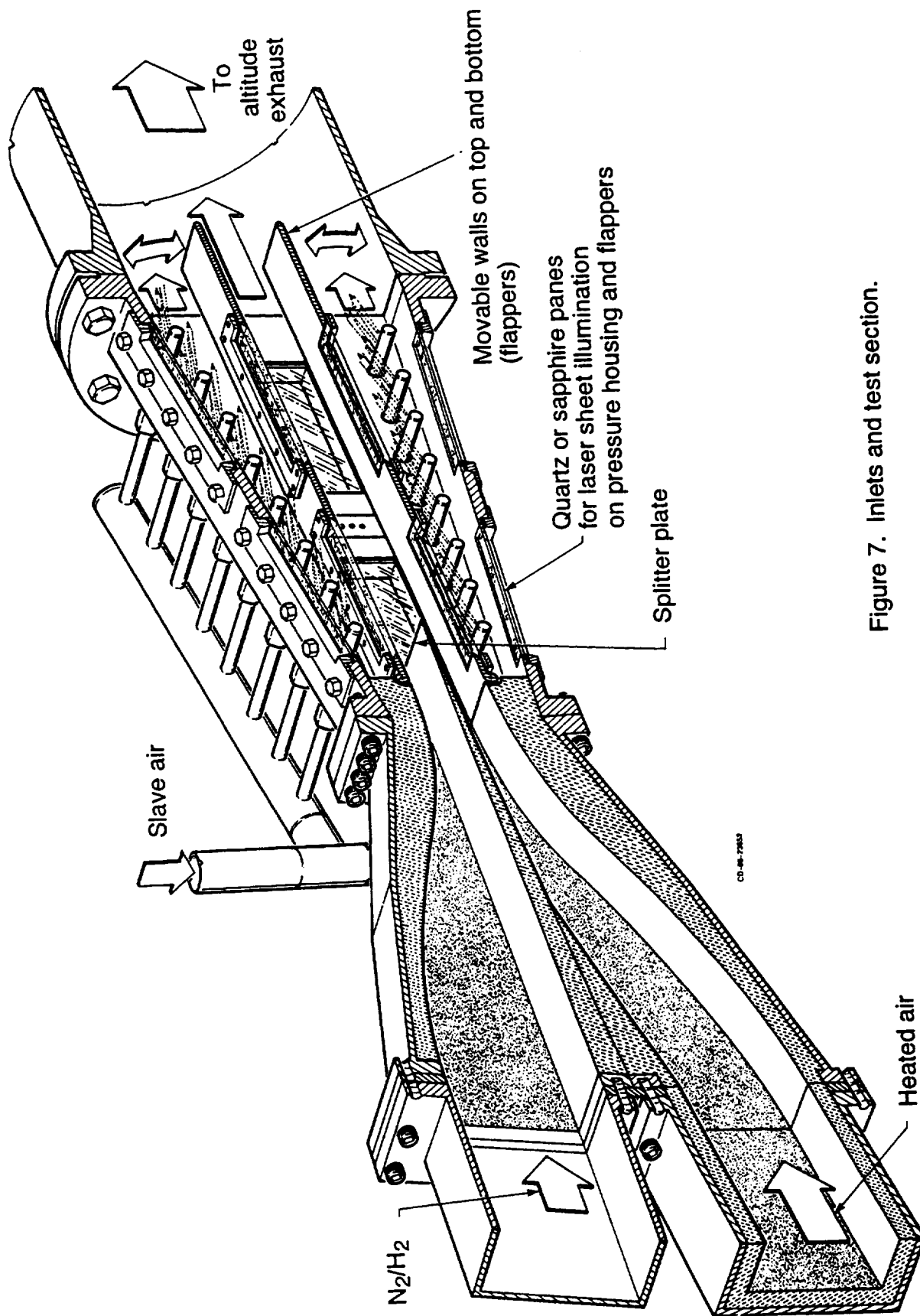


Figure 7. Inlets and test section.

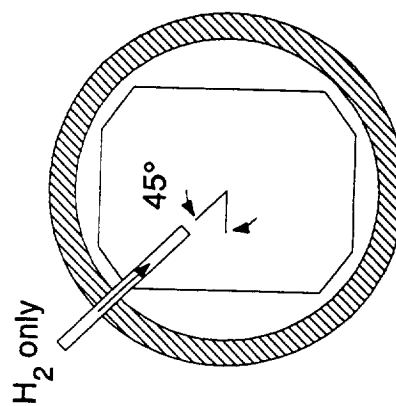
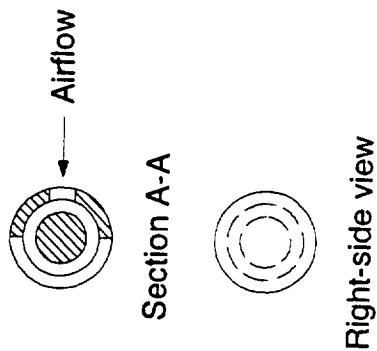
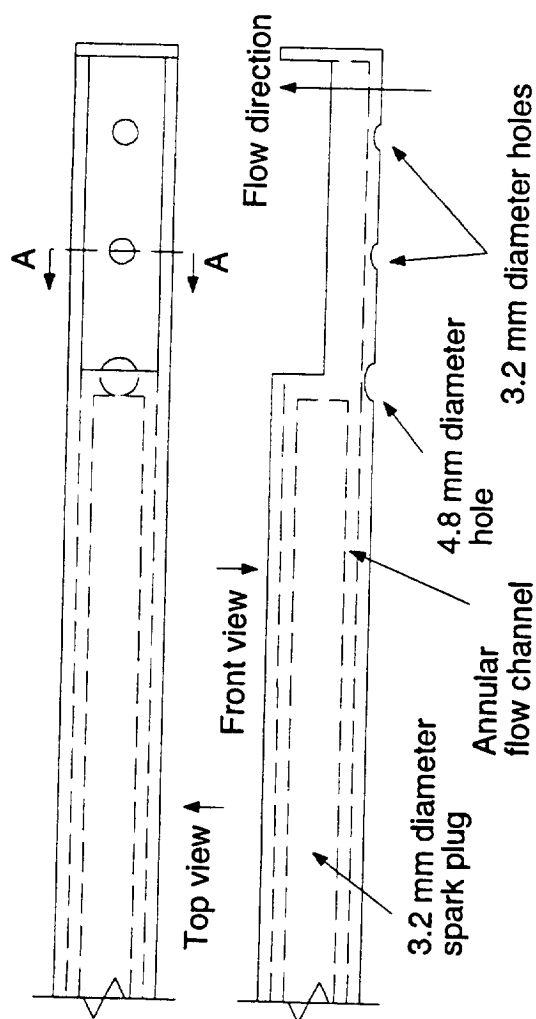


Figure 8. Details of hydrogen-fueled torch.

Notes:

1. Tube outside diameter, 12.7 mm, 1.6 mm wall thickness; 121 mm from tip to threaded fitting.
2. Thread fitting fits on outer surface of 36 cm diameter pipe.
3. One-half of tube cut open for 3.8 cm, starting from 3.2 mm thick splash plate at tip.
4. Holes are spaced at 11.1 mm, 26.2 mm, and 42.1 mm from tip end.
5. Torch is inserted 54.5 cm upstream of splitter plate tip.
6. Aircraft type 6.4 mm diameter spark plug for ignition, recessed 3.2 mm from opening, shut off after flame stabilized.
7. Thermocouple to monitor flame attachment to bluff body.
8. Torch is inserted 45° above horizontal plane with concave end facing downstream.

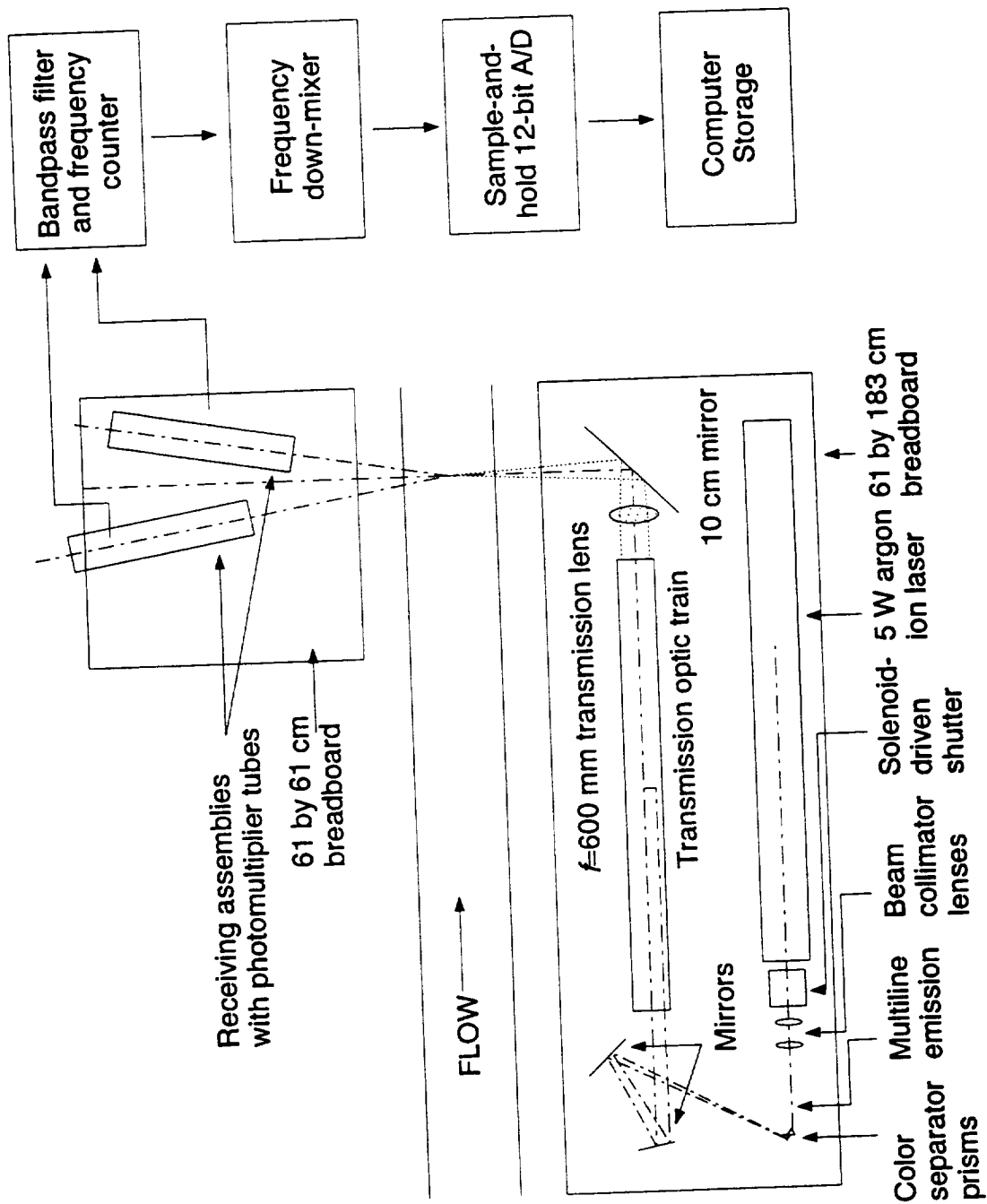


Figure 9. Layout of LDV table components.

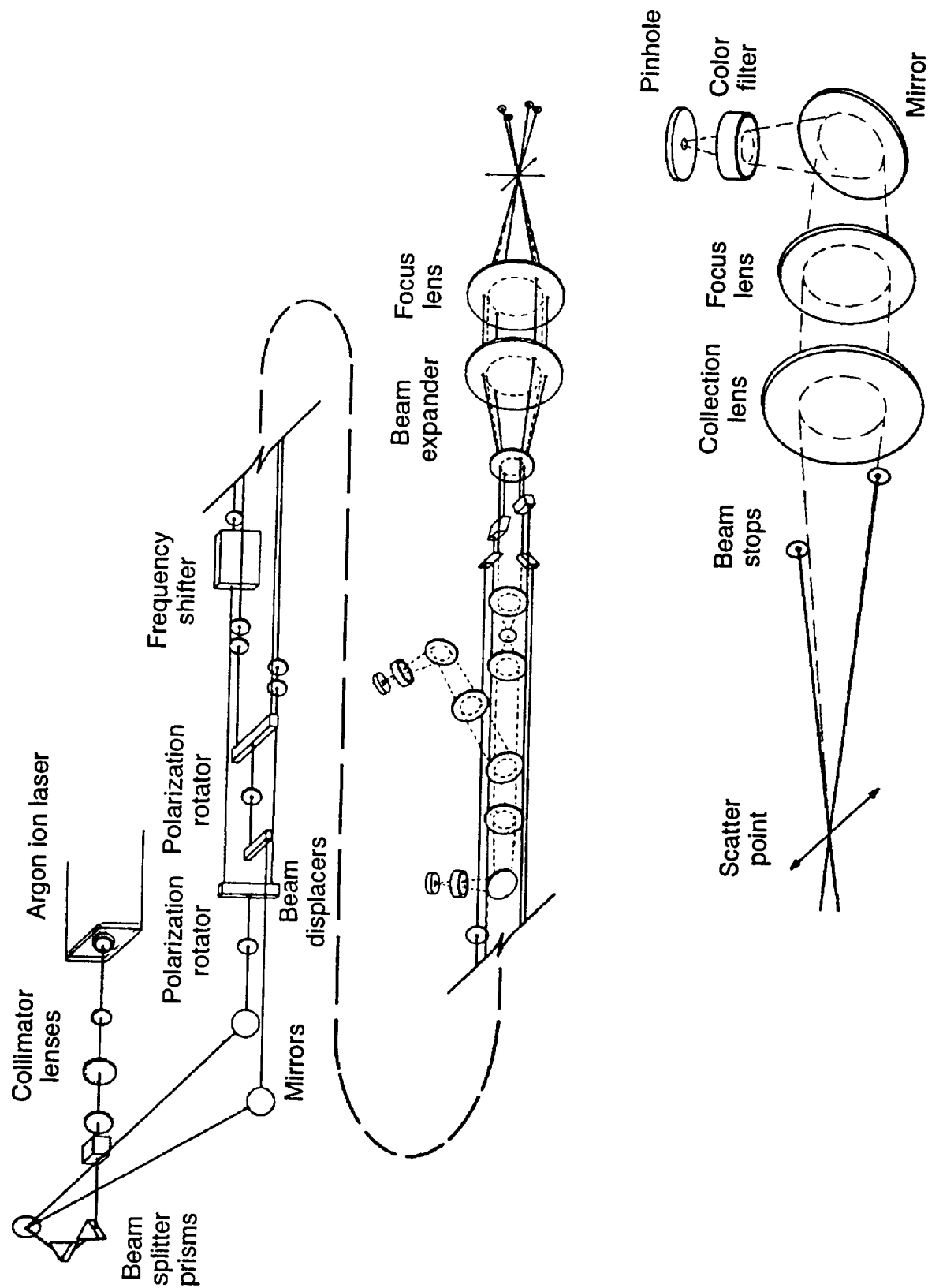


Figure 10. TSI 9100-7 four-beam, forward-scattered laser Doppler system.

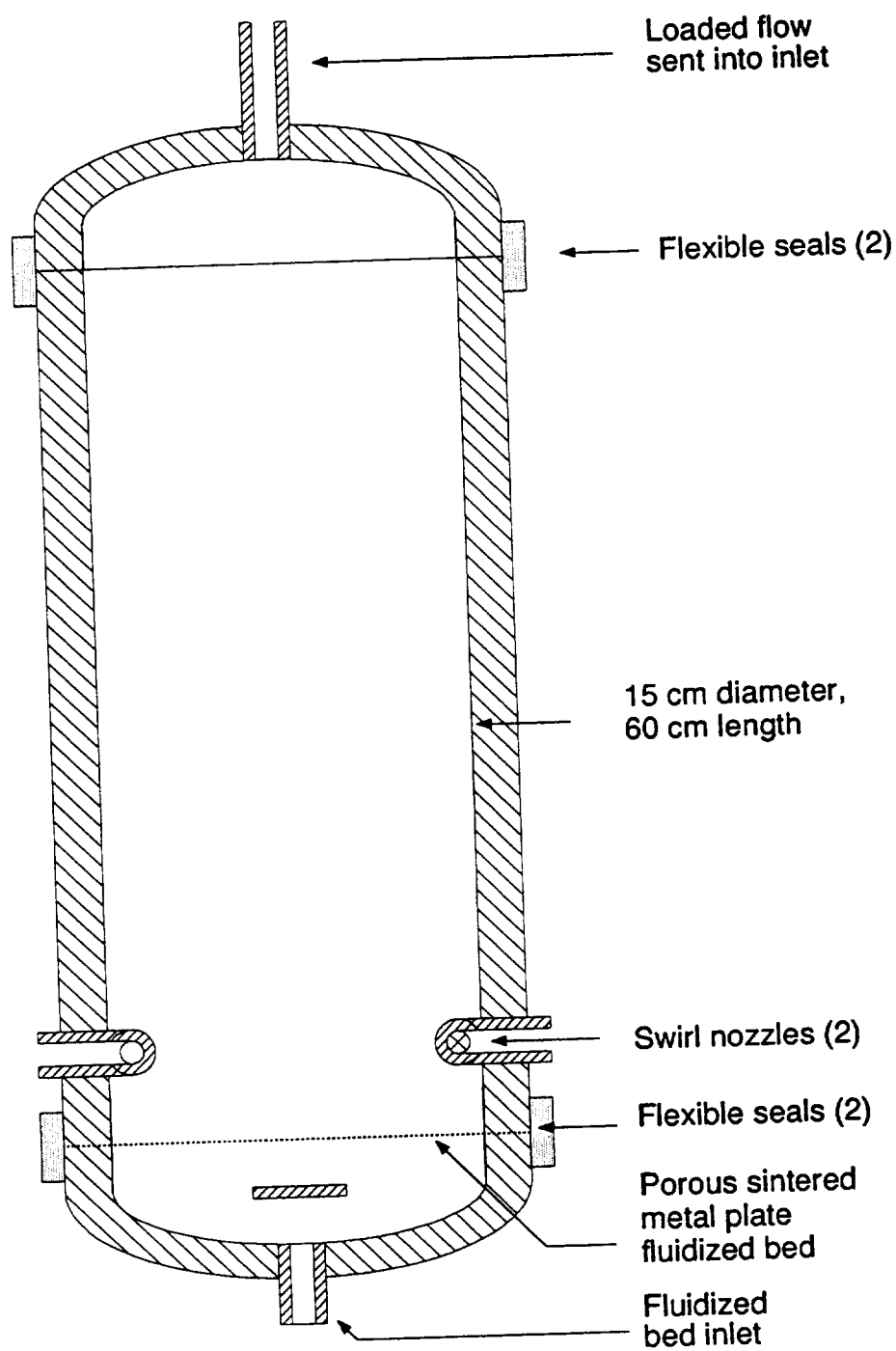


Figure 11. Seeder design.

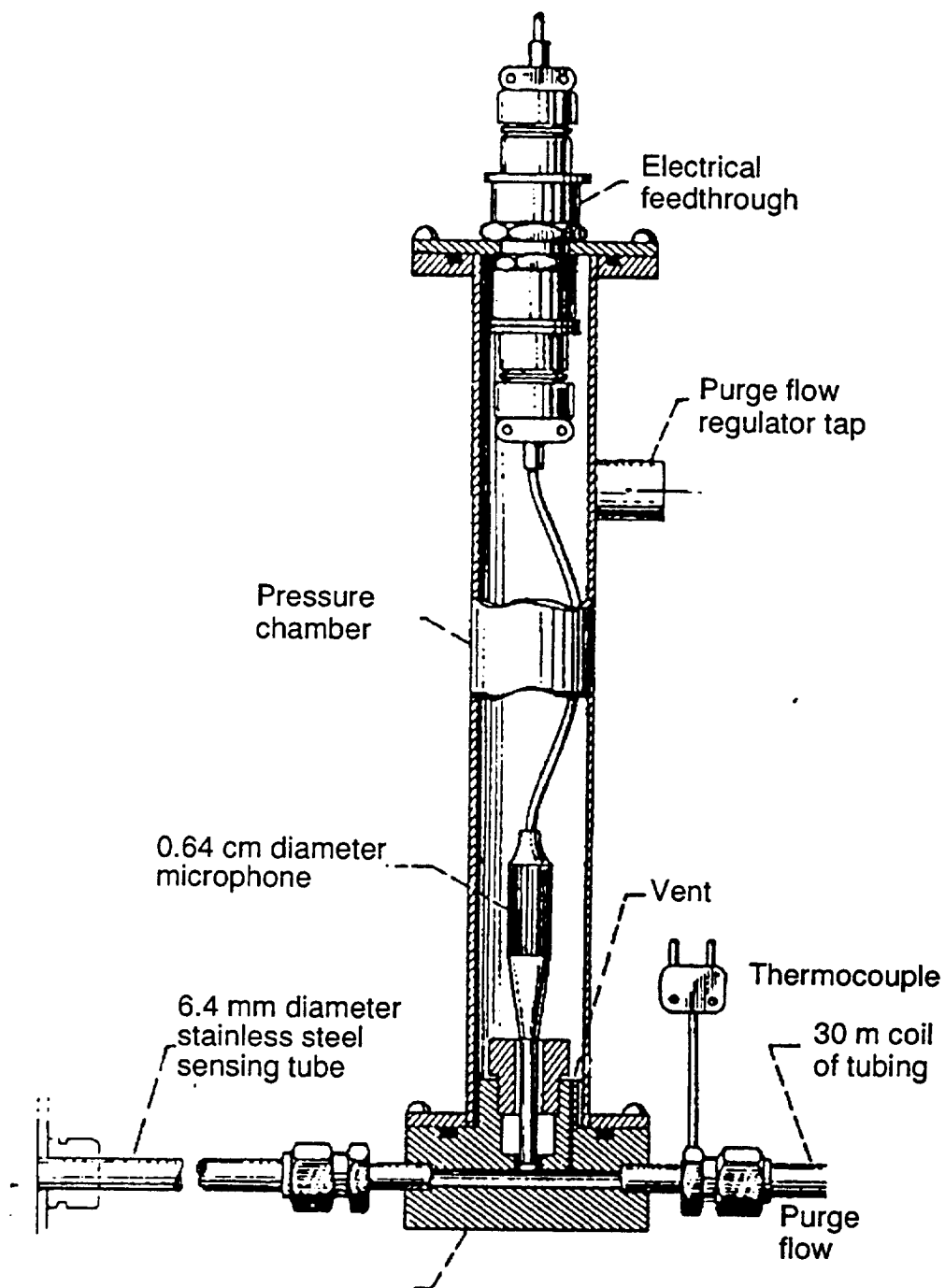


Figure 12. Infinite-line microphone assembly. The purge flow regulator tap is used to feed back the chamber pressure to a differential pressure loader that provides a 3 psi pressure across the 30 m tubing coil.

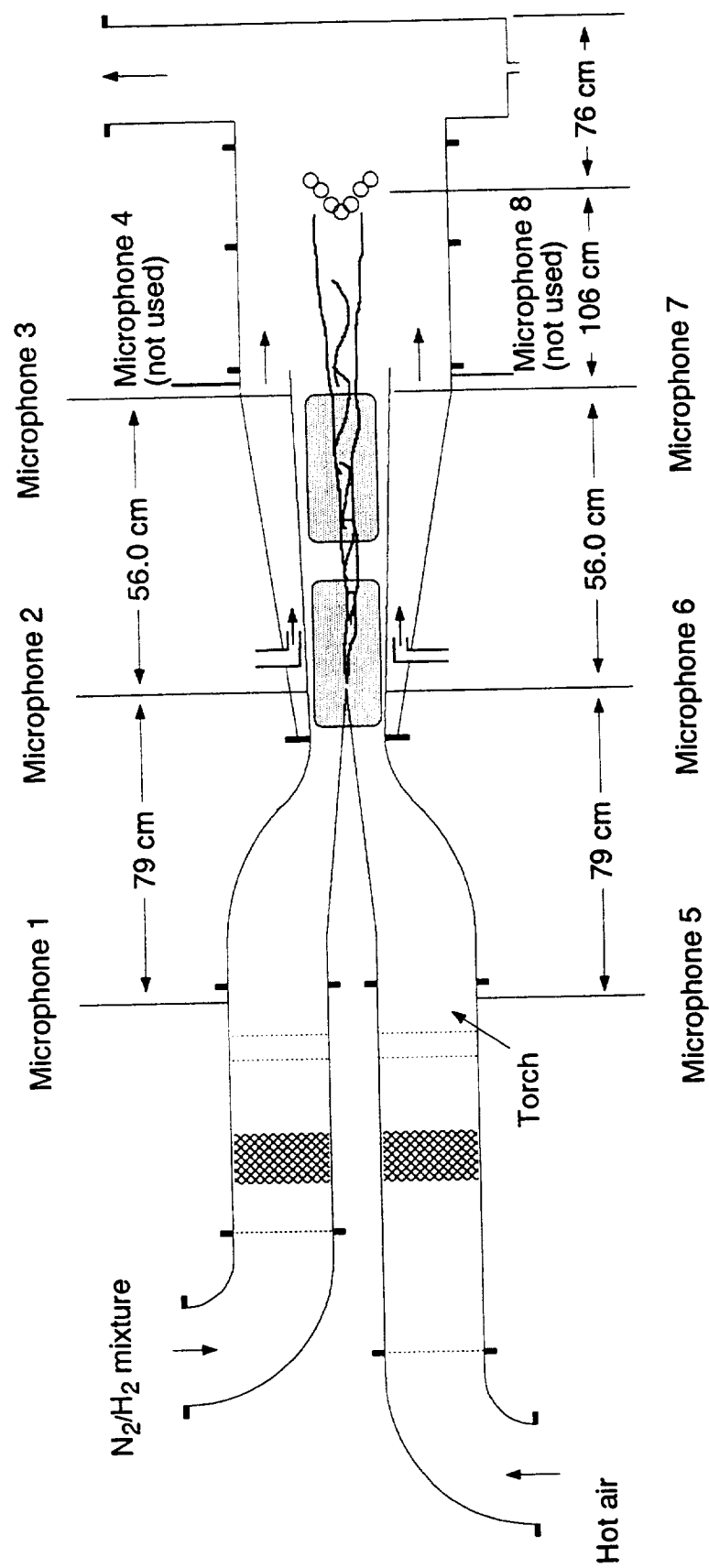


Figure 13. Microphone locations.

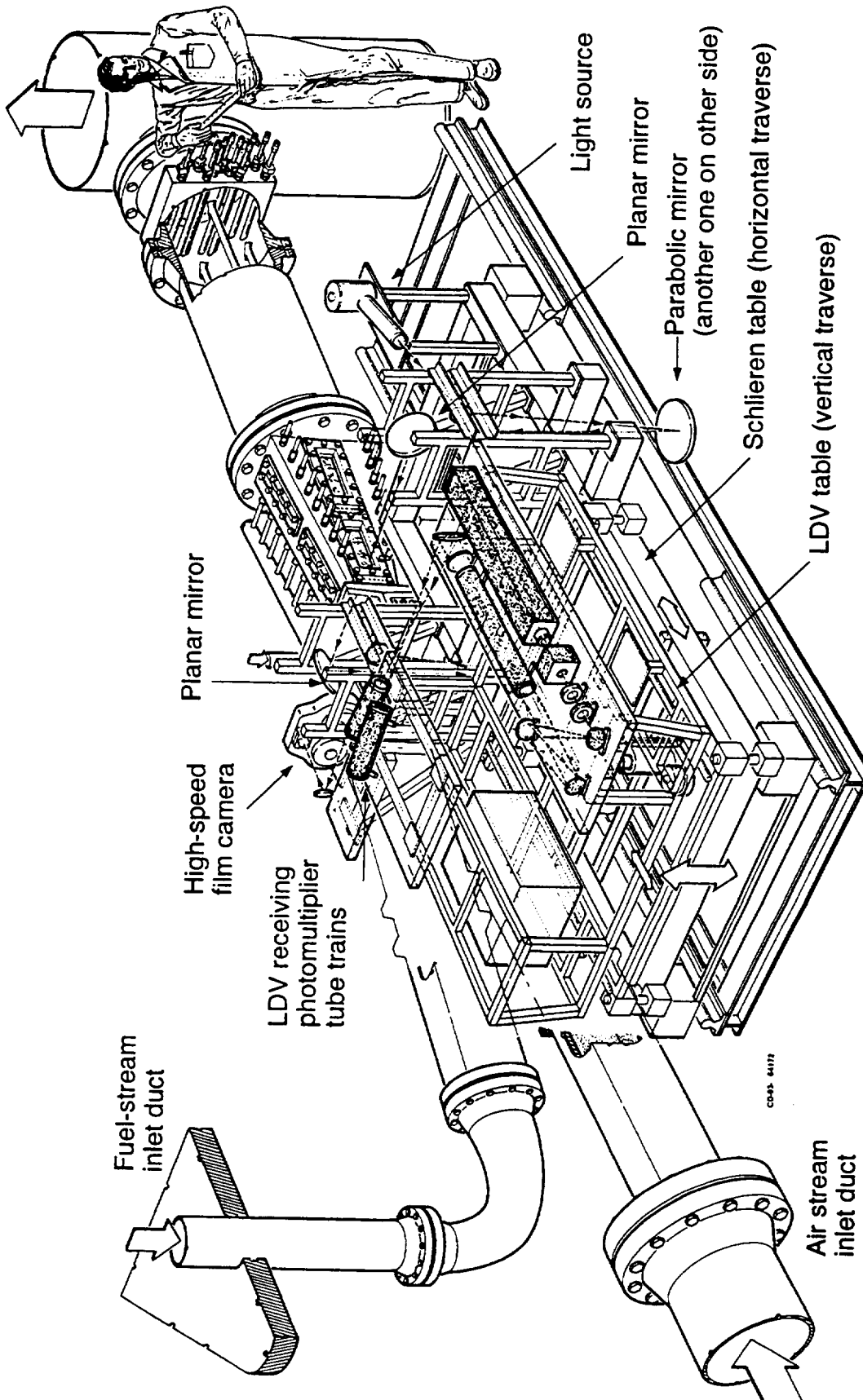


Figure 14. Schlieren and LDV table in three dimensions.

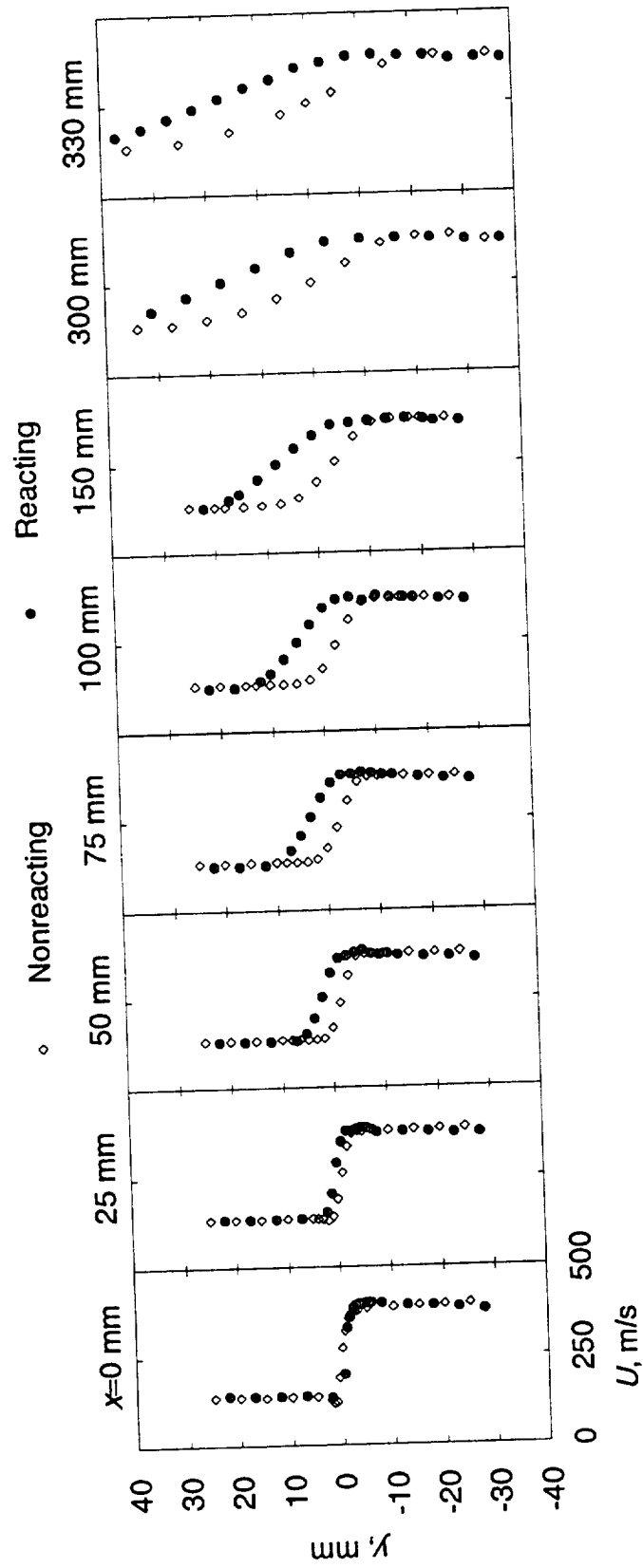


Figure 15. Streamwise mean flow distribution, $U(x, y)$.

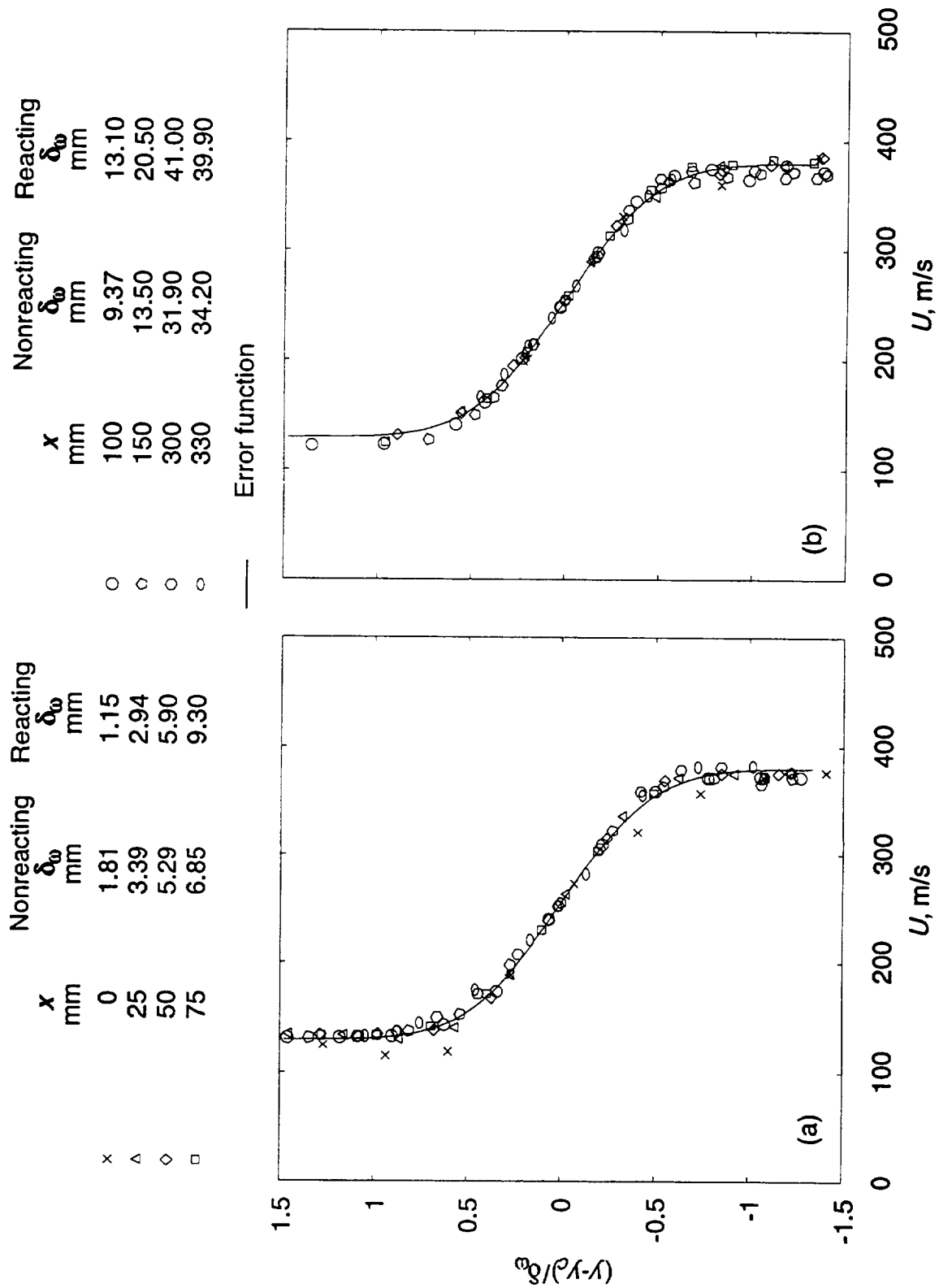


Figure 16. Streamwise mean flow velocity profiles normalized by vorticity width. (a) Nonreacting. (b) Reacting.

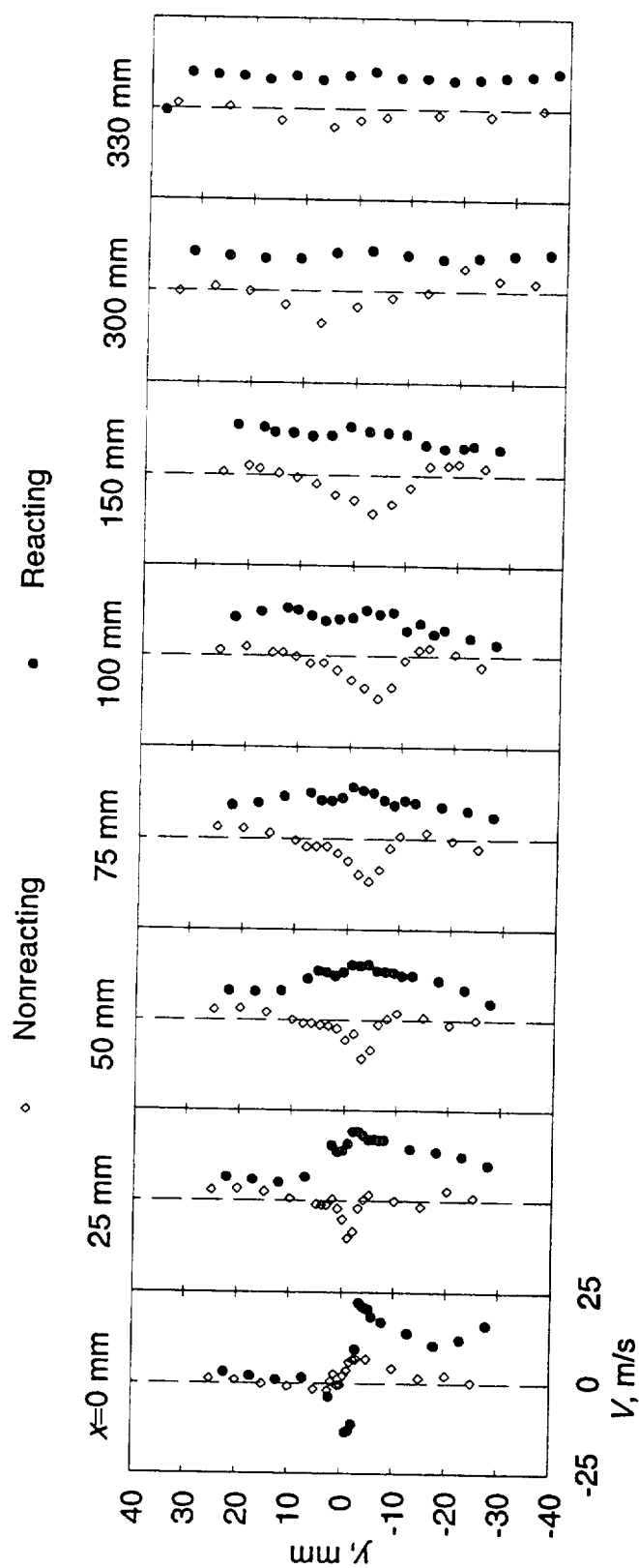


Figure 18. Cross-stream mean flow velocity in planar shear layer, $V(x,y)$.

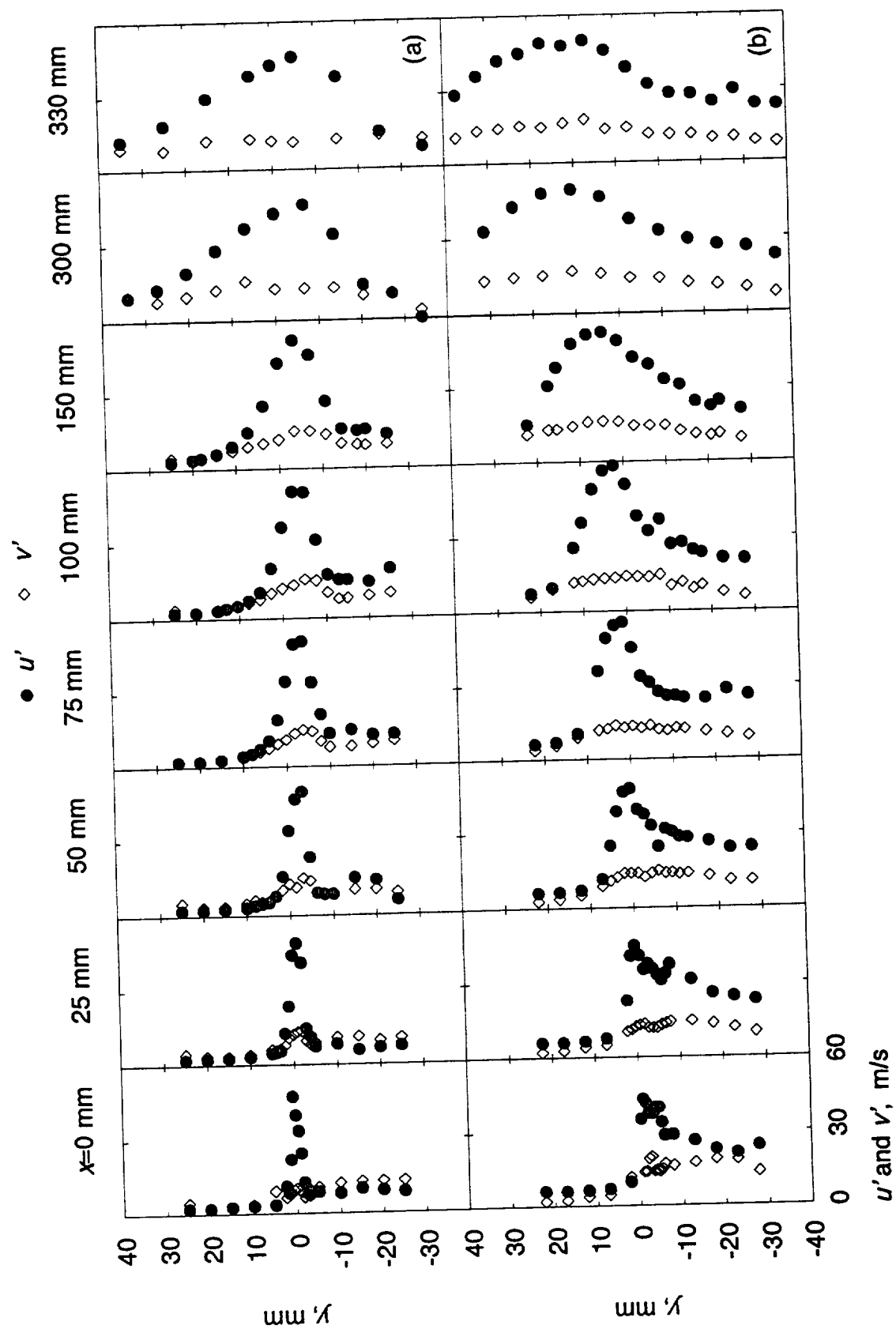


Figure 19. Streamwise and cross-stream absolute turbulence intensities, $u'(x,y)$, $v'(x,y)$. (a) Nonreacting. (b) Reacting.

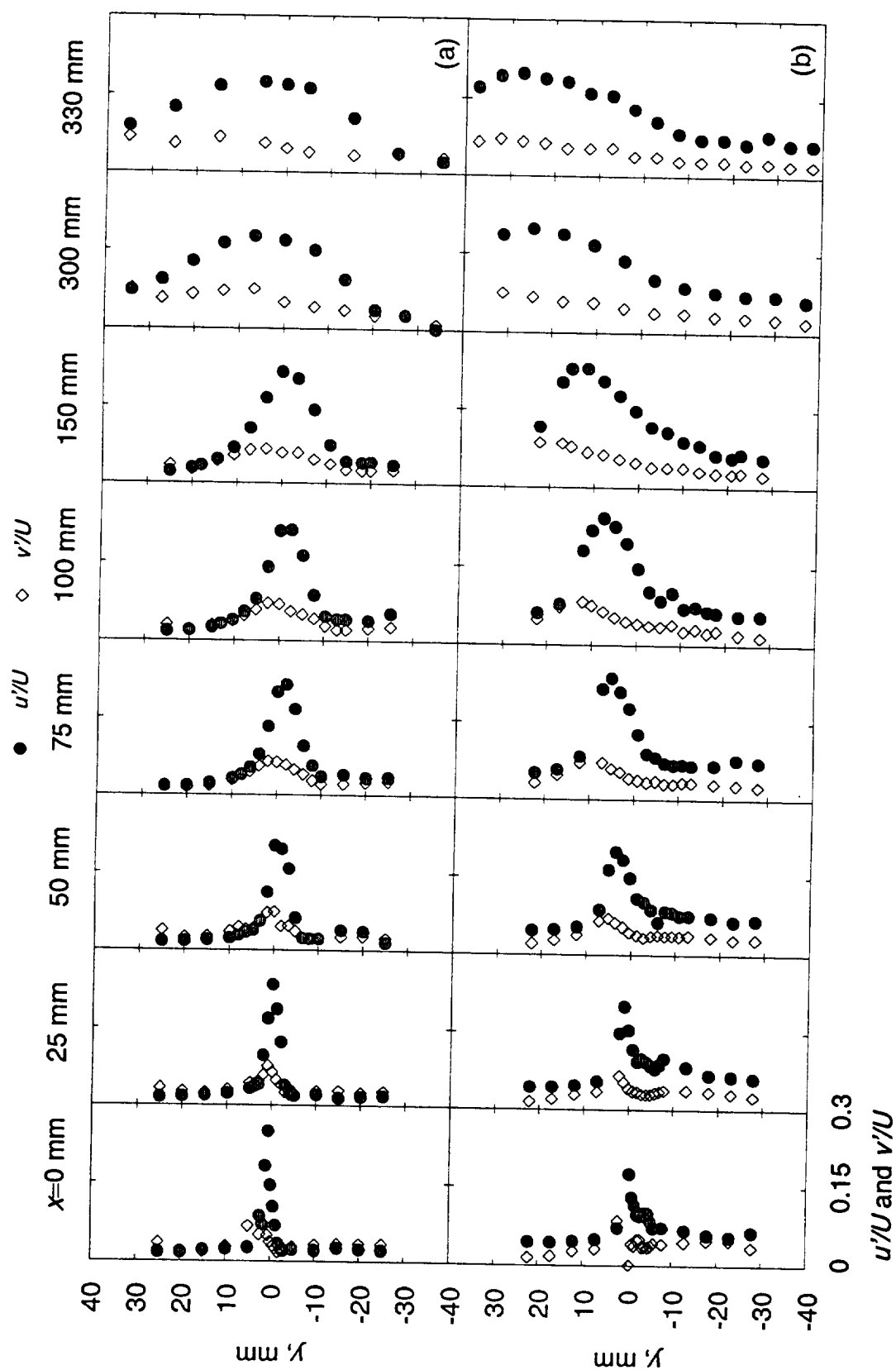


Figure 20. Streamwise and cross-stream fluctuations normalized by streamwise mean speed.
(a) Nonreacting. (b) Reacting

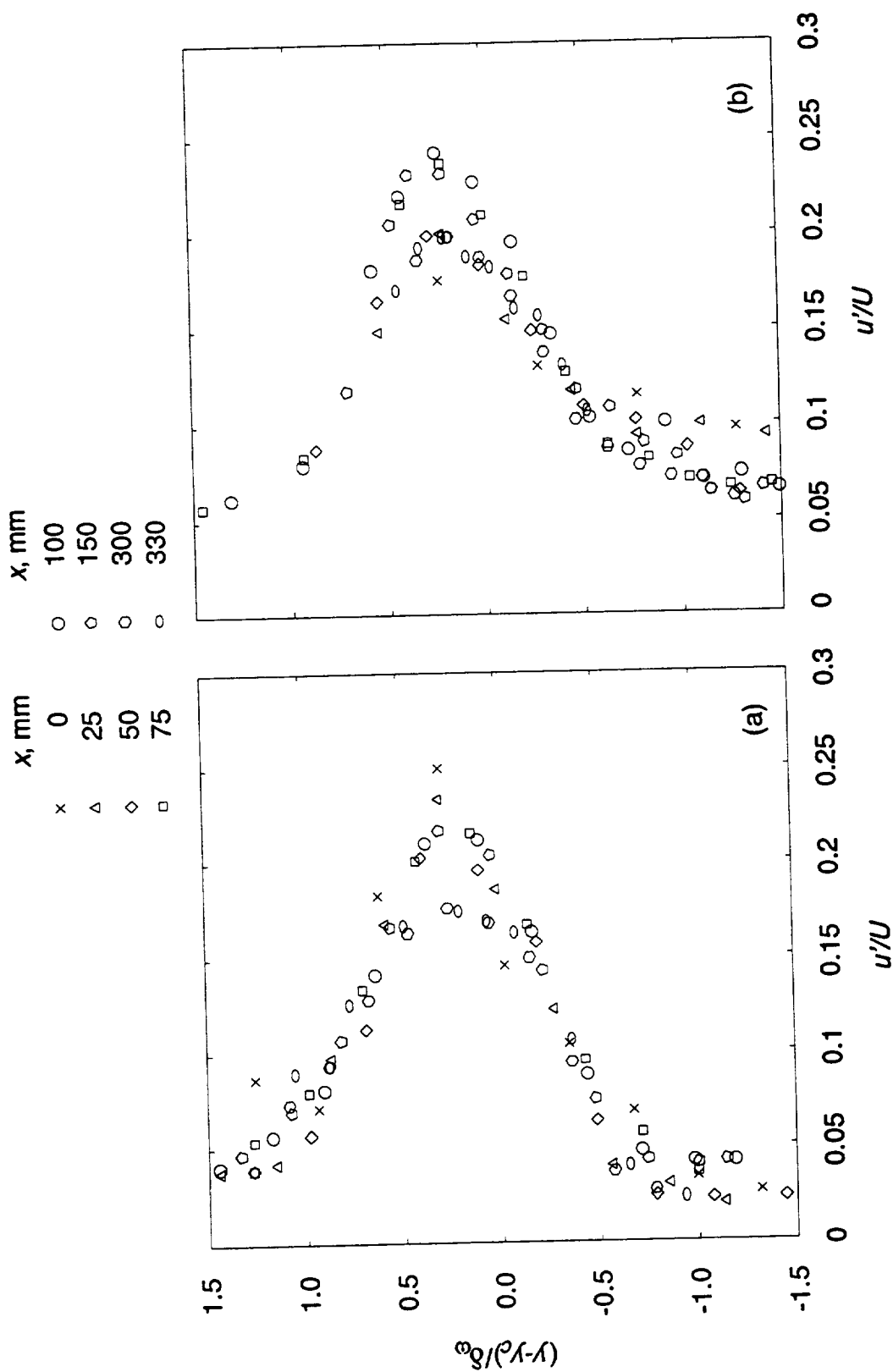


Figure 21. Streamwise turbulence intensity normalized by local mean flow speed. (a) Nonreacting. (b) Reacting.

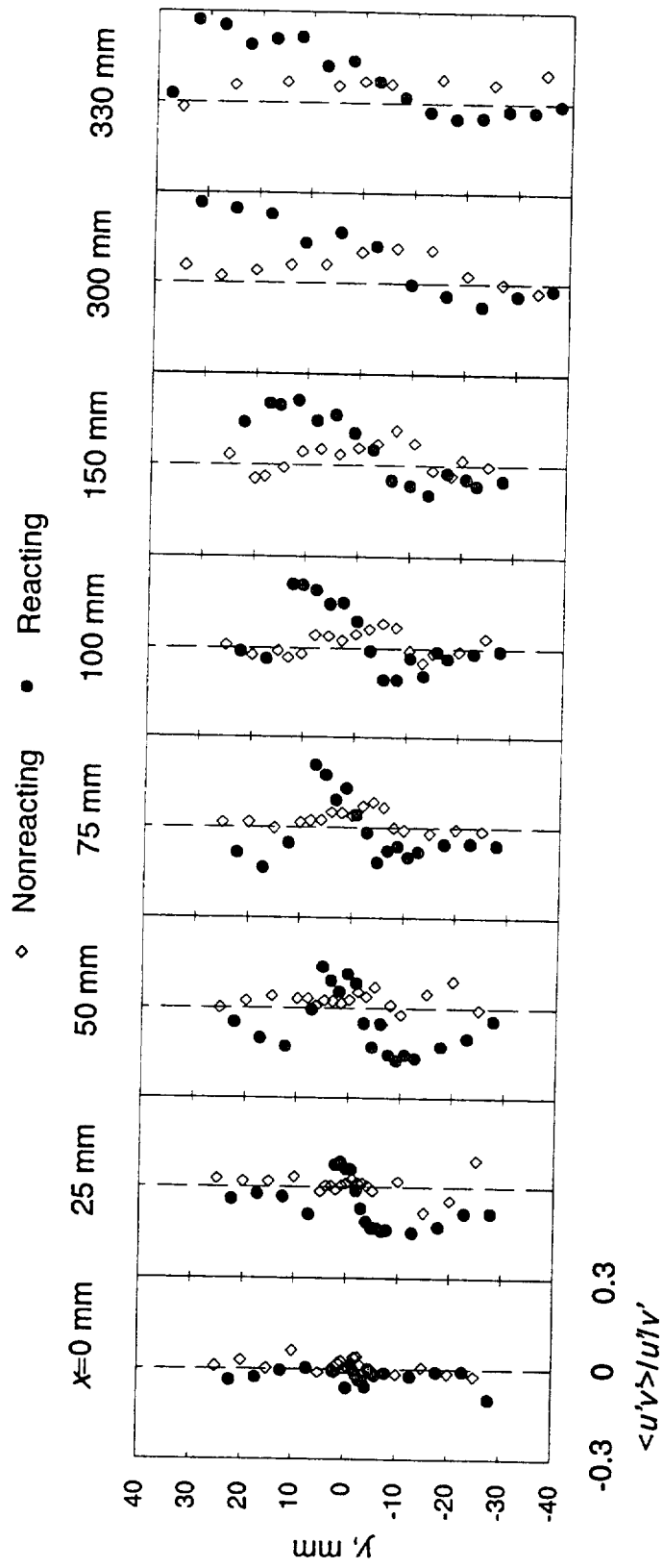


Figure 22. Reynolds stress normalized by local turbulence intensities u' and v' .

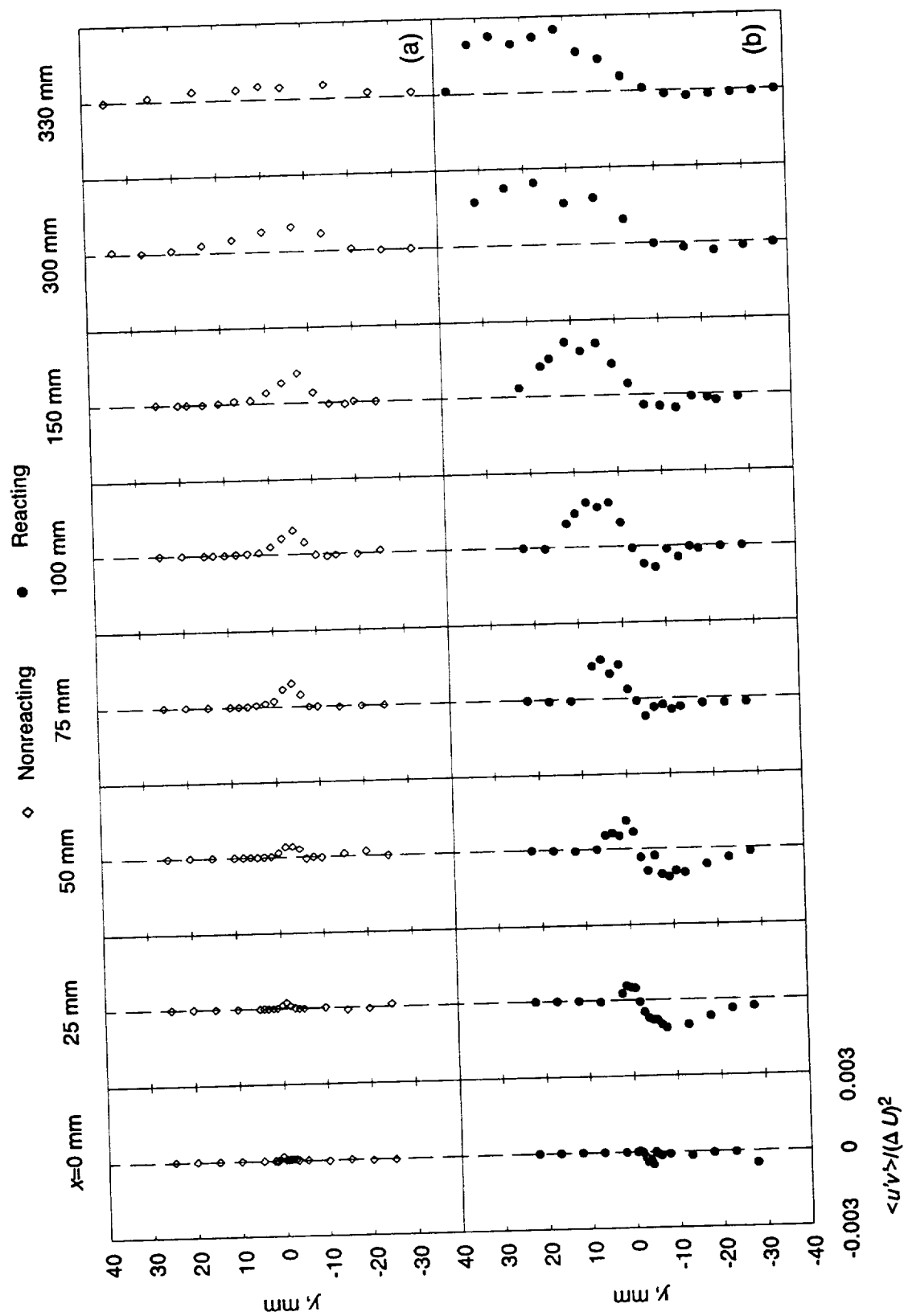


Figure 23. Reynolds stress normalized by slip speed squared. (a) Nonreacting. (b) Reacting.

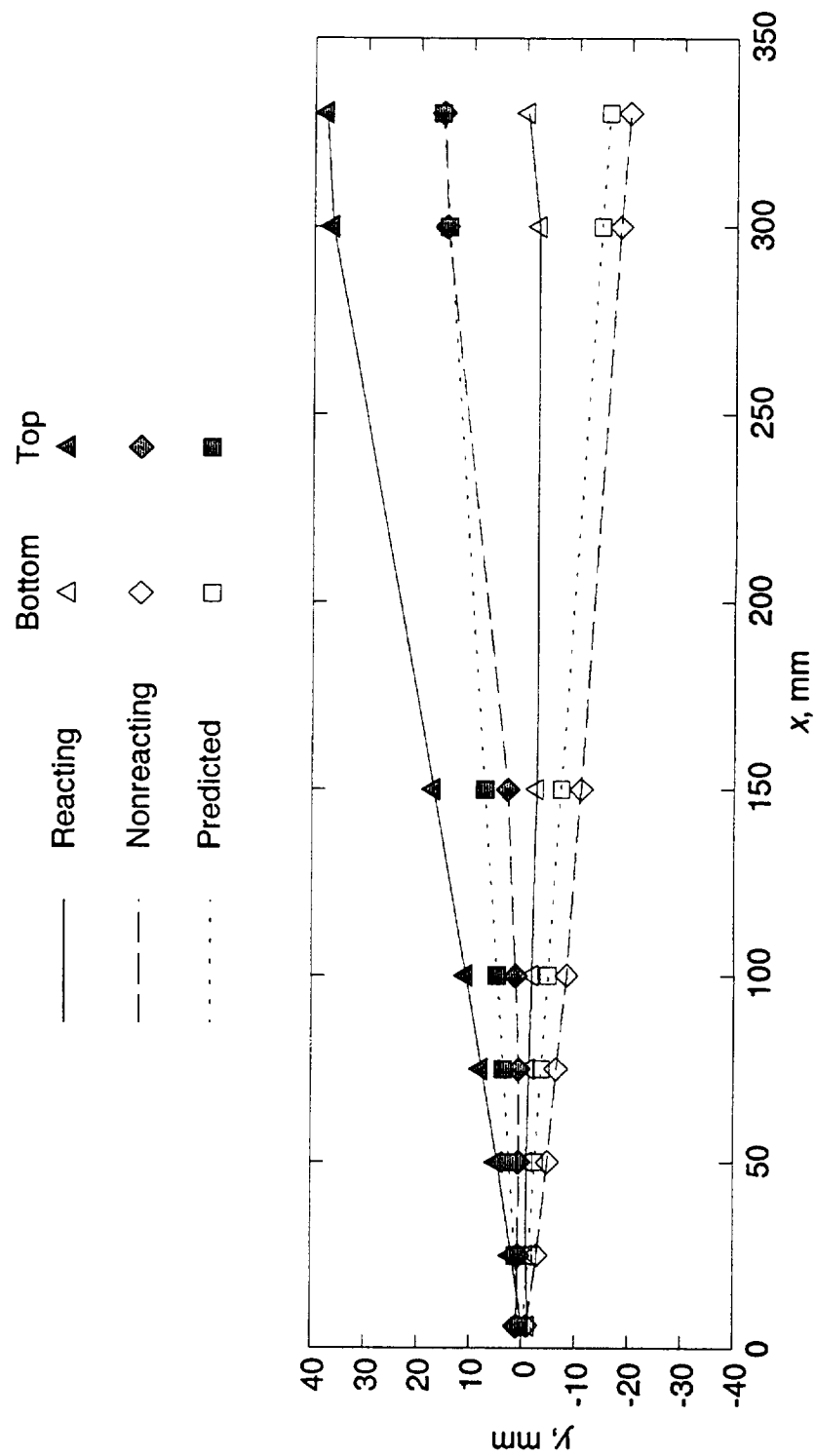


Figure 24. Shear layer vorticity width boundaries.

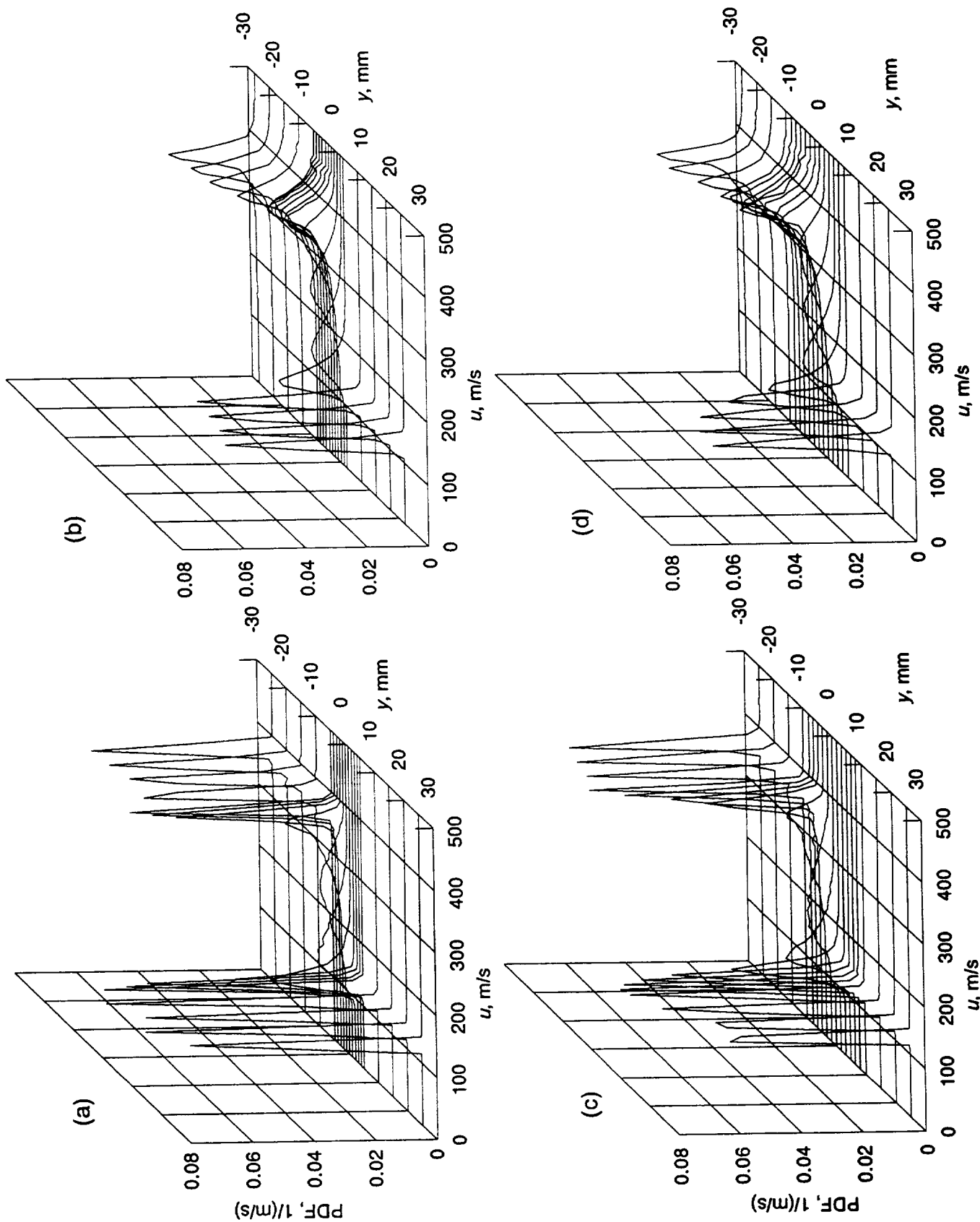


Figure 25. Probability density functions of streamwise velocity component, u .
 (a) $x=25$ mm, nonreacting. (b) $x=25$ mm, reacting. (c) $x=50$ mm, nonreacting. (d) $x=50$ mm, reacting.

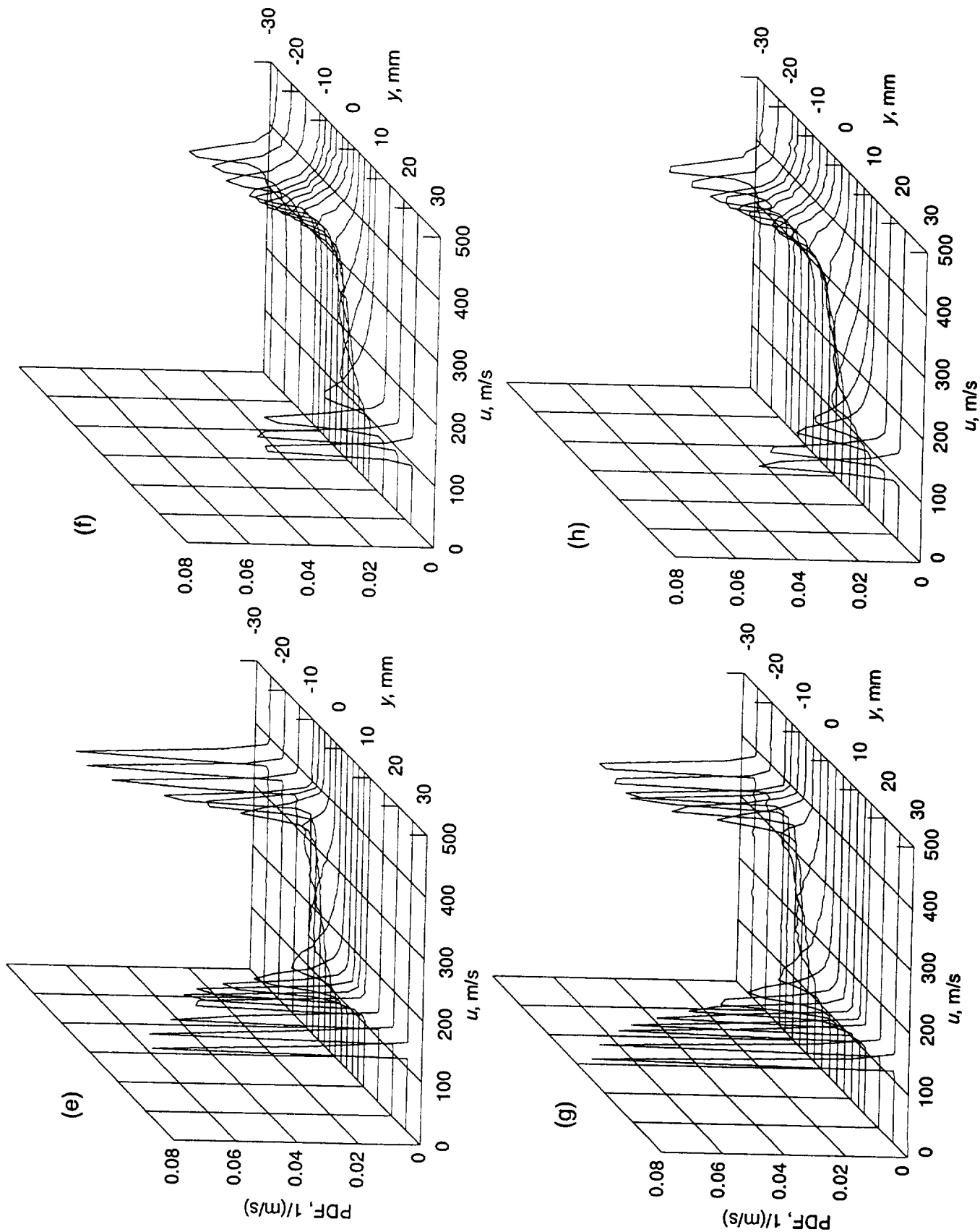


Figure 25. Continued. (e) $x=75$ mm, nonreacting. (f) $x=150$ mm, nonreacting. (g) $x=75$ mm, reacting. (h) $x=150$ mm, reacting.

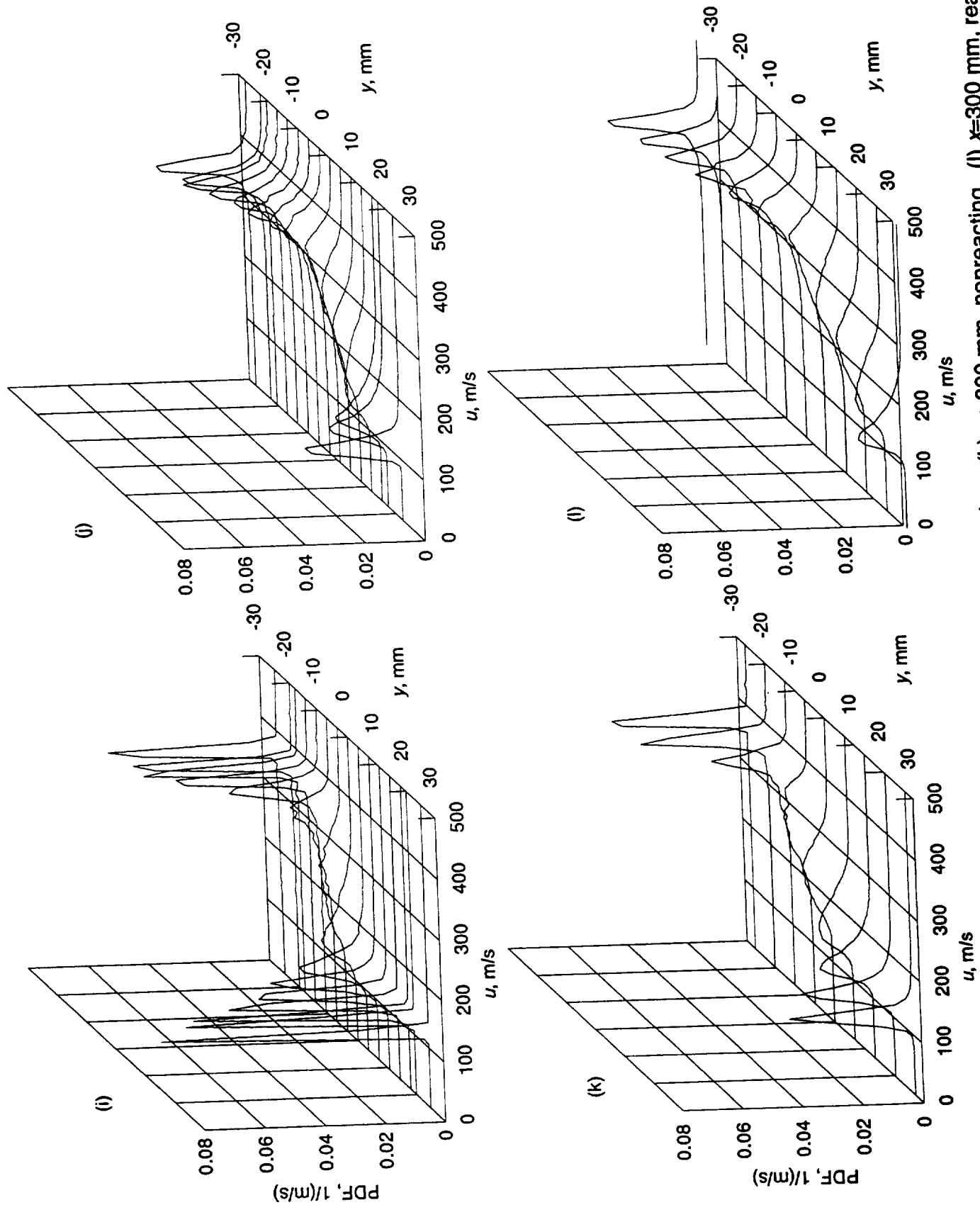


Figure 25. Concluded. (i) $x=150$ mm, nonreacting. (j) $x=150$ mm, reacting. (l) $x=300$ mm, nonreacting. (k) $x=300$ mm, reacting.

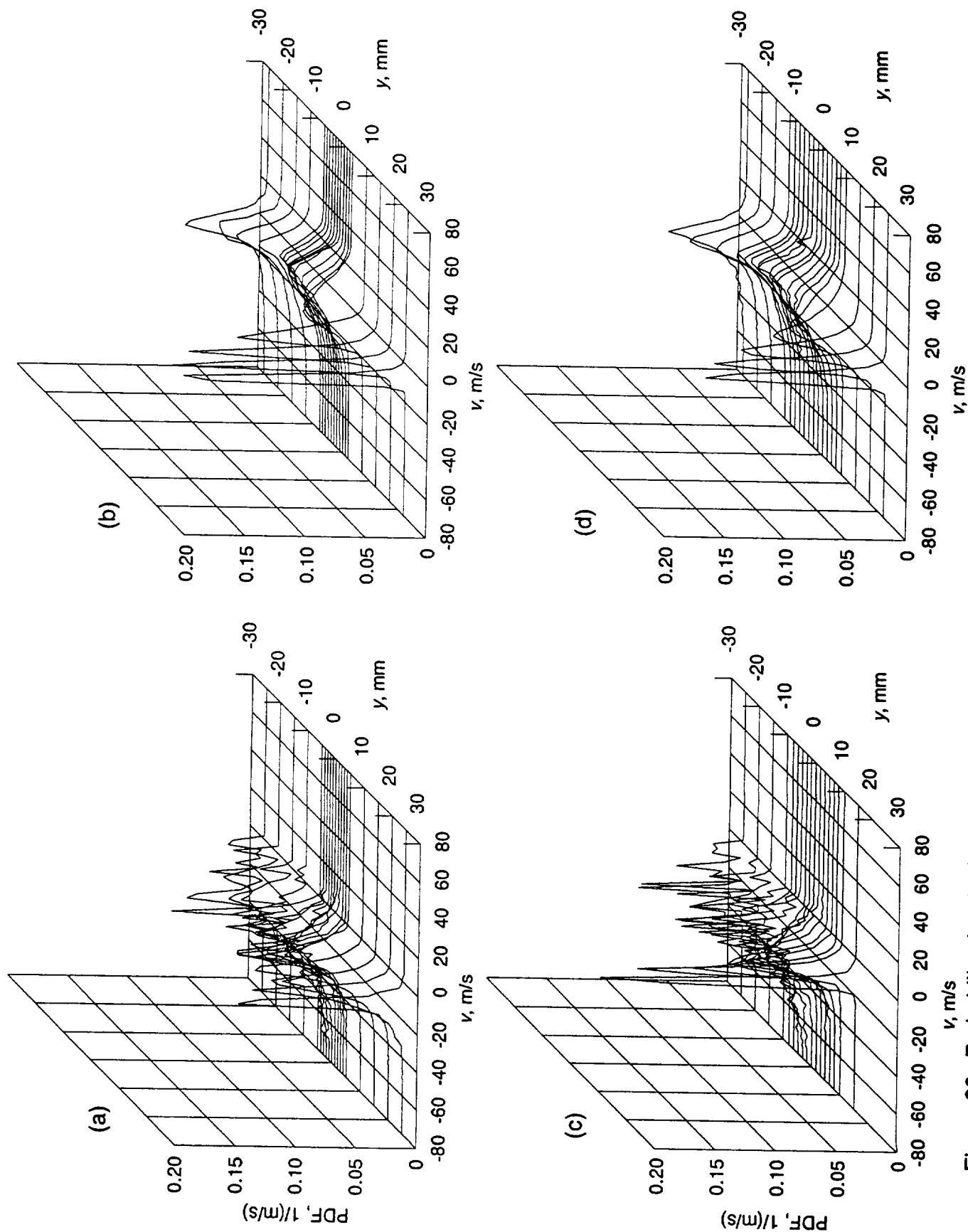
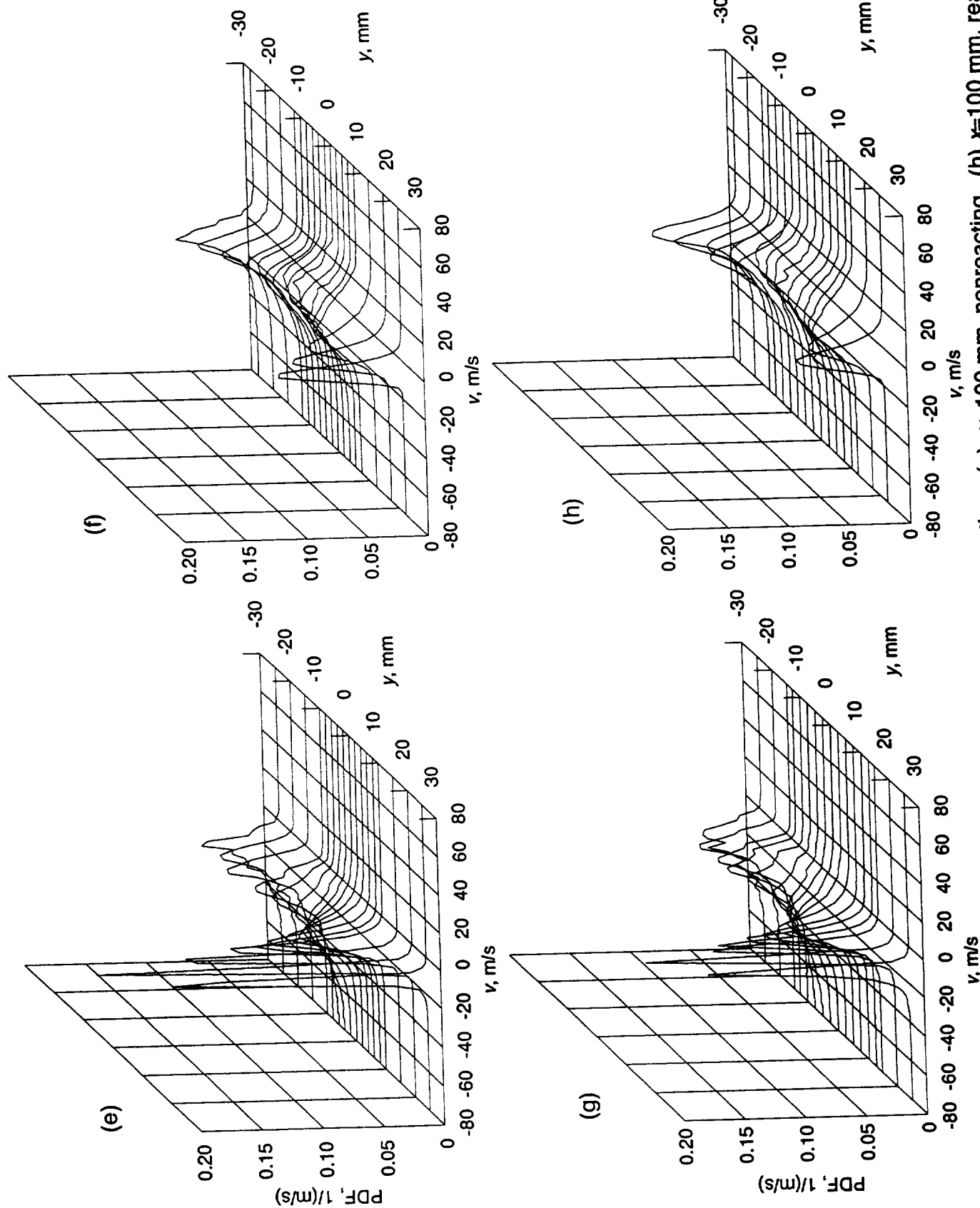


Figure 26. Probability density functions of cross-stream velocity component, v .
(a) $x=25$ mm, nonreacting. (b) $x=25$ mm, reacting. (c) $x=50$ mm, nonreacting. (d) $x=50$ mm, reacting.



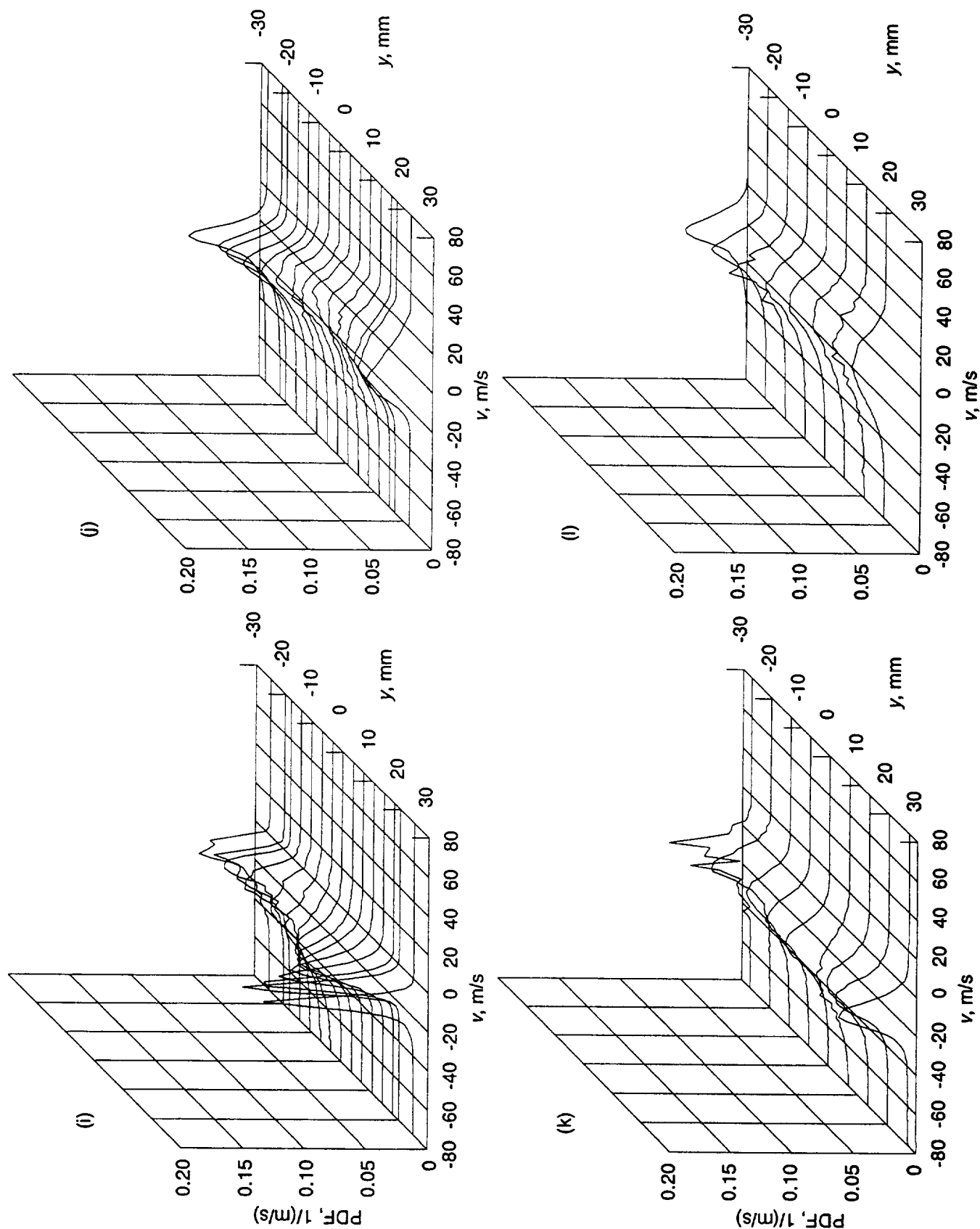


Figure 26. Concluded. (i) $x=150$ mm, nonreacting. (j) $x=150$ mm, reacting. (k) $x=300$ mm, nonreacting. (l) $x=300$ mm, reacting.

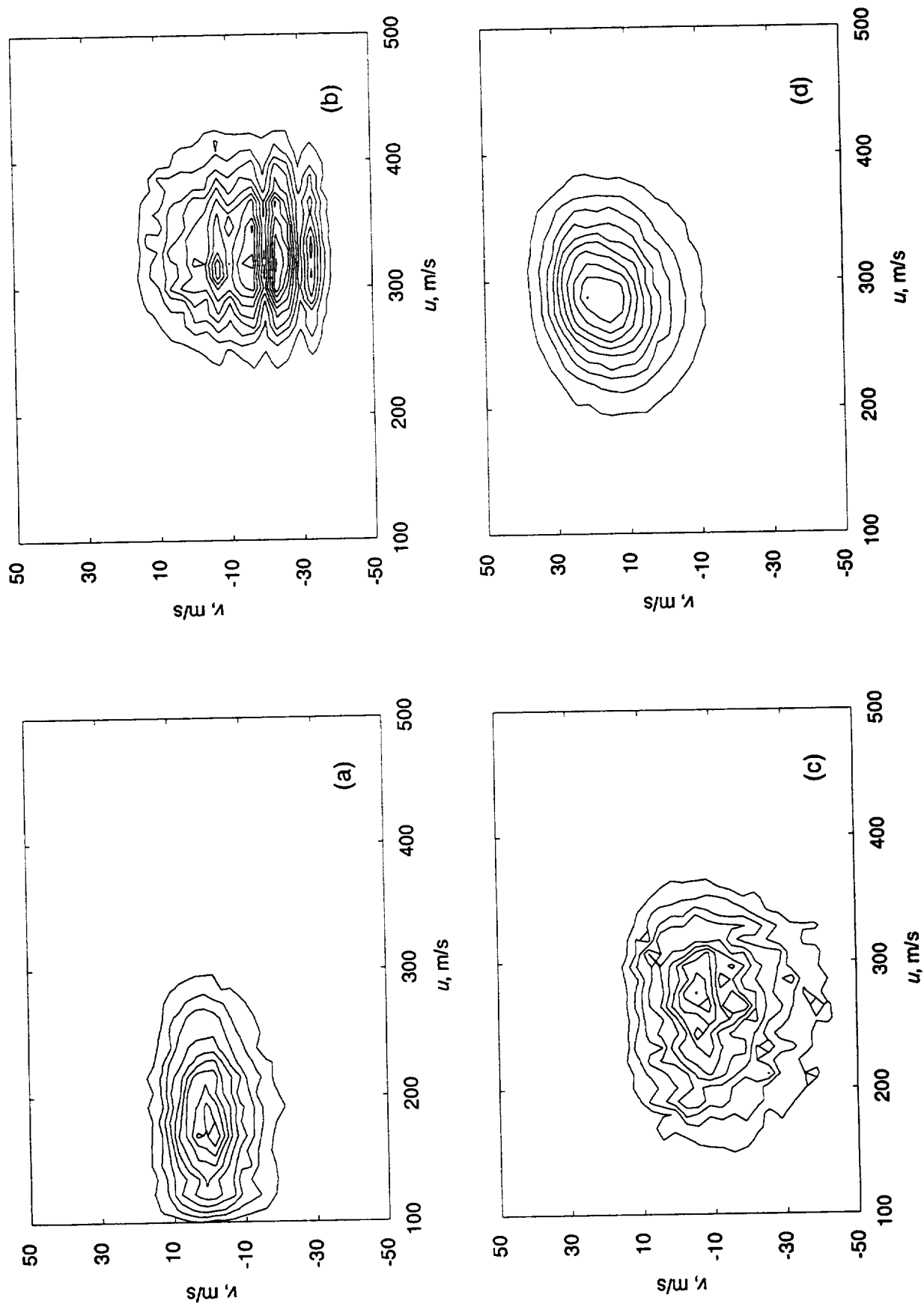


Figure 27. Joint probability density function contours of streamwise and cross-stream flow velocities, u and v . (a) $x=6$ mm, $y=0.6$ mm, nonreacting. (b) $x=5.7$ mm, $y=-1.0$ mm, reacting. (c) $x=25$ mm, $y=-1.0$ mm, nonreacting. (d) $x=25$ mm, $y=0.2$ mm, reacting.

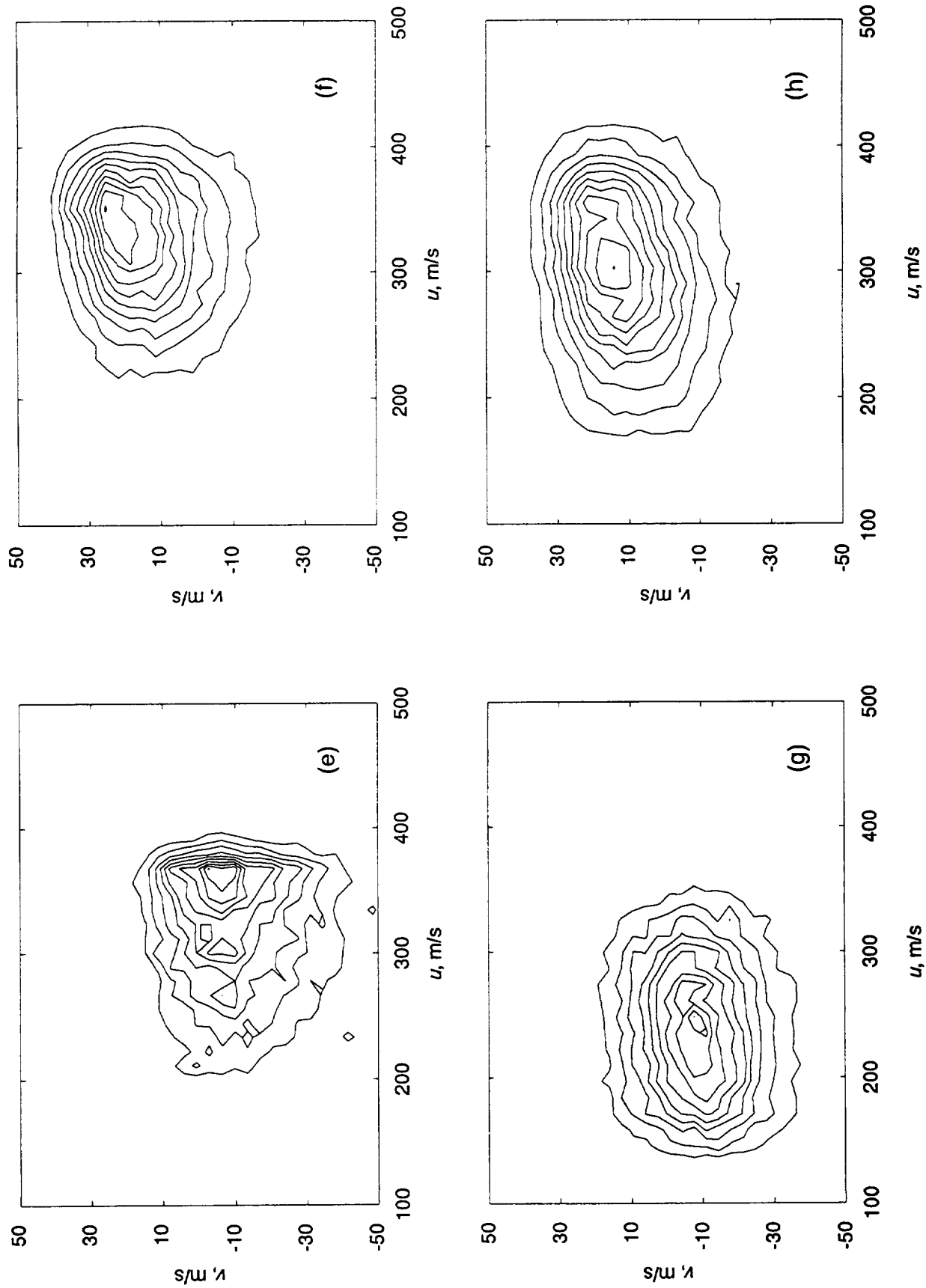


Figure 27. Continued. (e) $x=50$ mm, $y=-3.2$ mm, nonreacting. (f) $x=50$ mm, $y=0.4$ mm, reacting. (g) $x=100$ mm, $y=-2.6$ mm, nonreacting. (h) $x=100$ mm, $y=2.4$ mm, reacting.

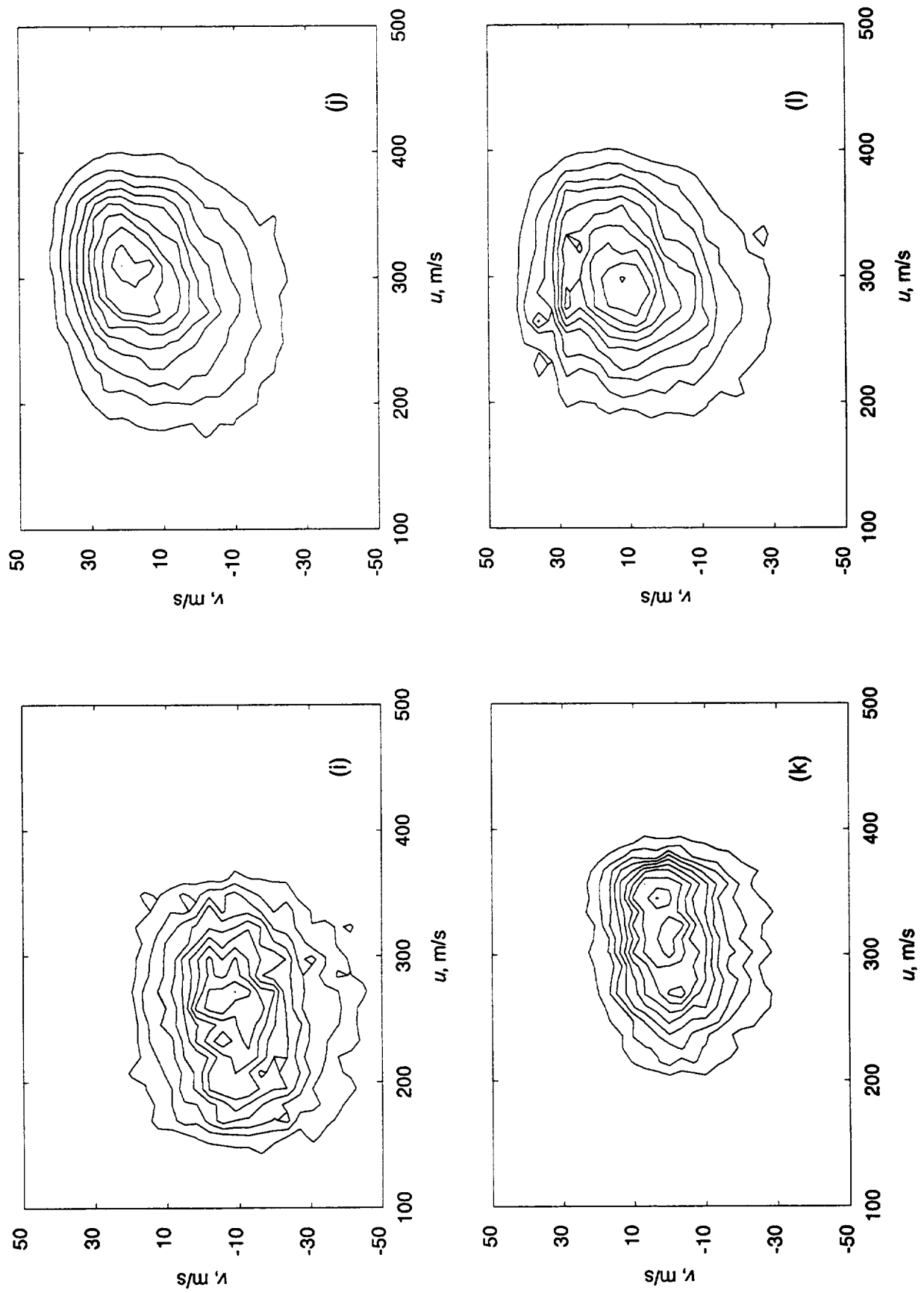


Figure 27. Concluded. (i) $x=150$ mm, $y=-3.6$ mm, nonreacting. (j) $x=150$ mm, $y=-4.4$ mm, reacting. (k) $x=300$ mm, $y=-6.8$ mm, nonreacting. (l) $x=300$ mm, $y=-10.8$ mm, reacting.

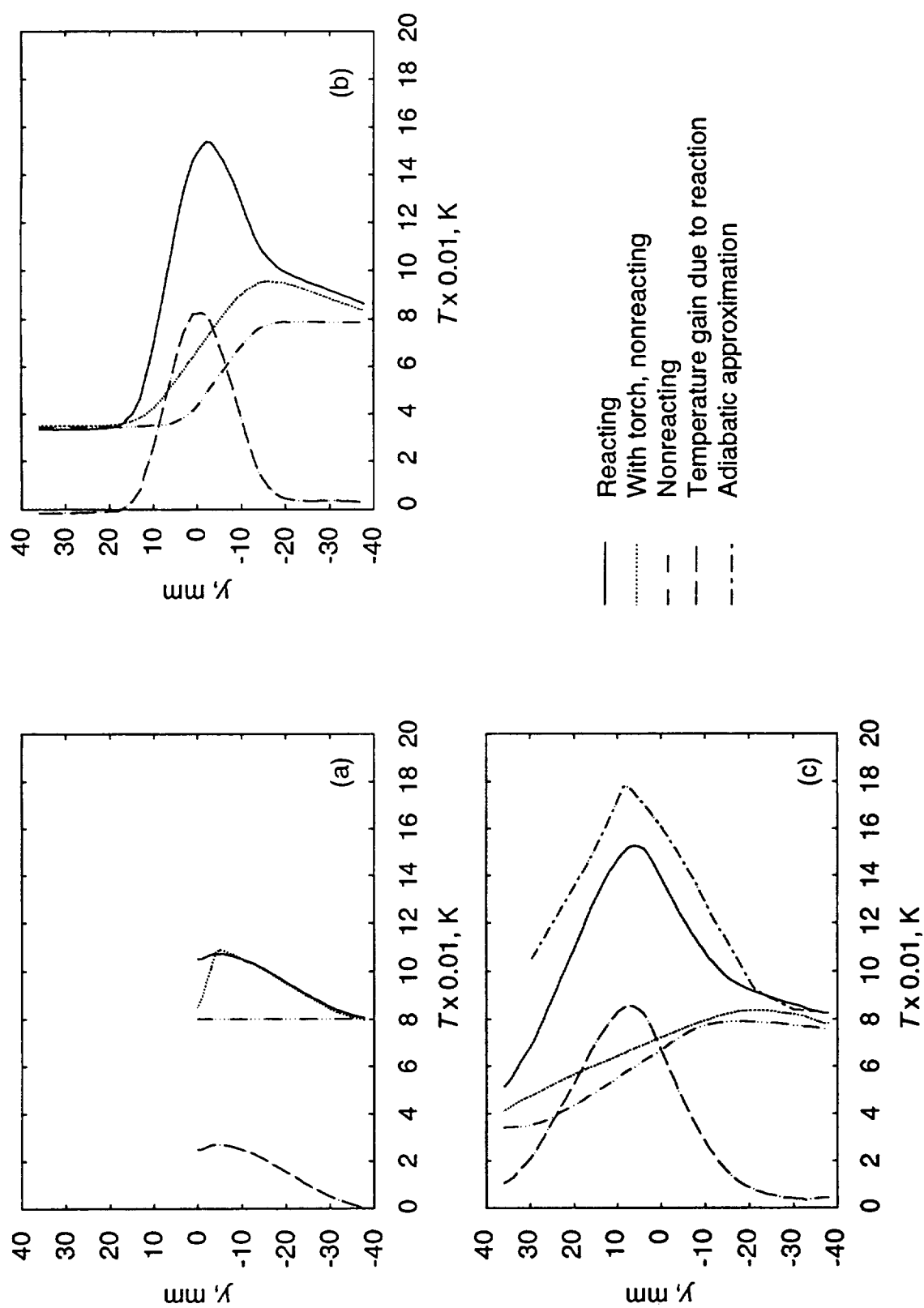


Figure 28. Temperature distribution, uncompensated for radiation loss, for planar shear layer at three downstream locations from splitter plate tip. (a) $x=0$ mm. (b) $x=150$ mm. (c) $x=300$ mm.

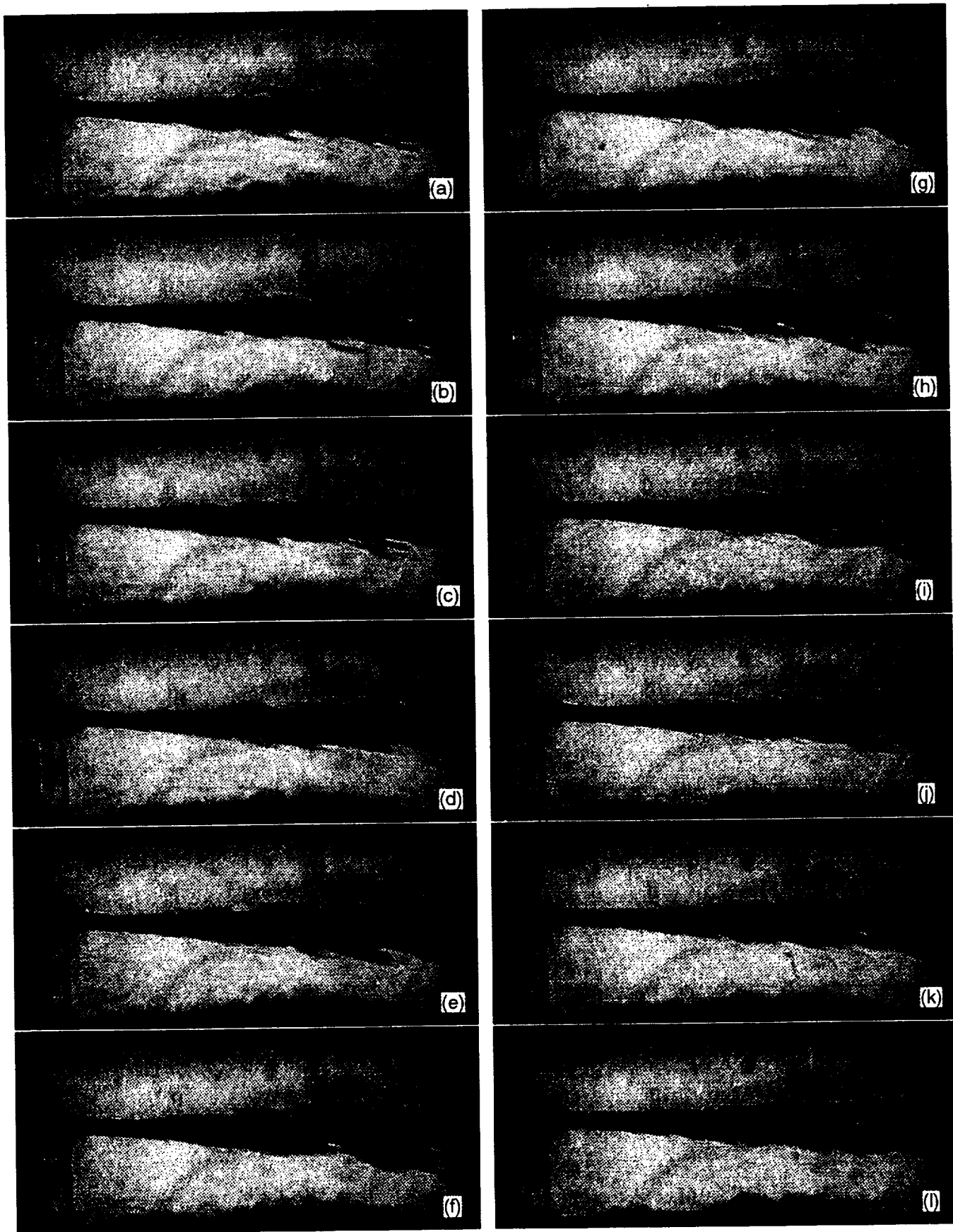


Figure 29. Schlieren images of nonreacting planar shear layer flows. Frames are 0.1 ms apart, start at top left downward and then shift right.

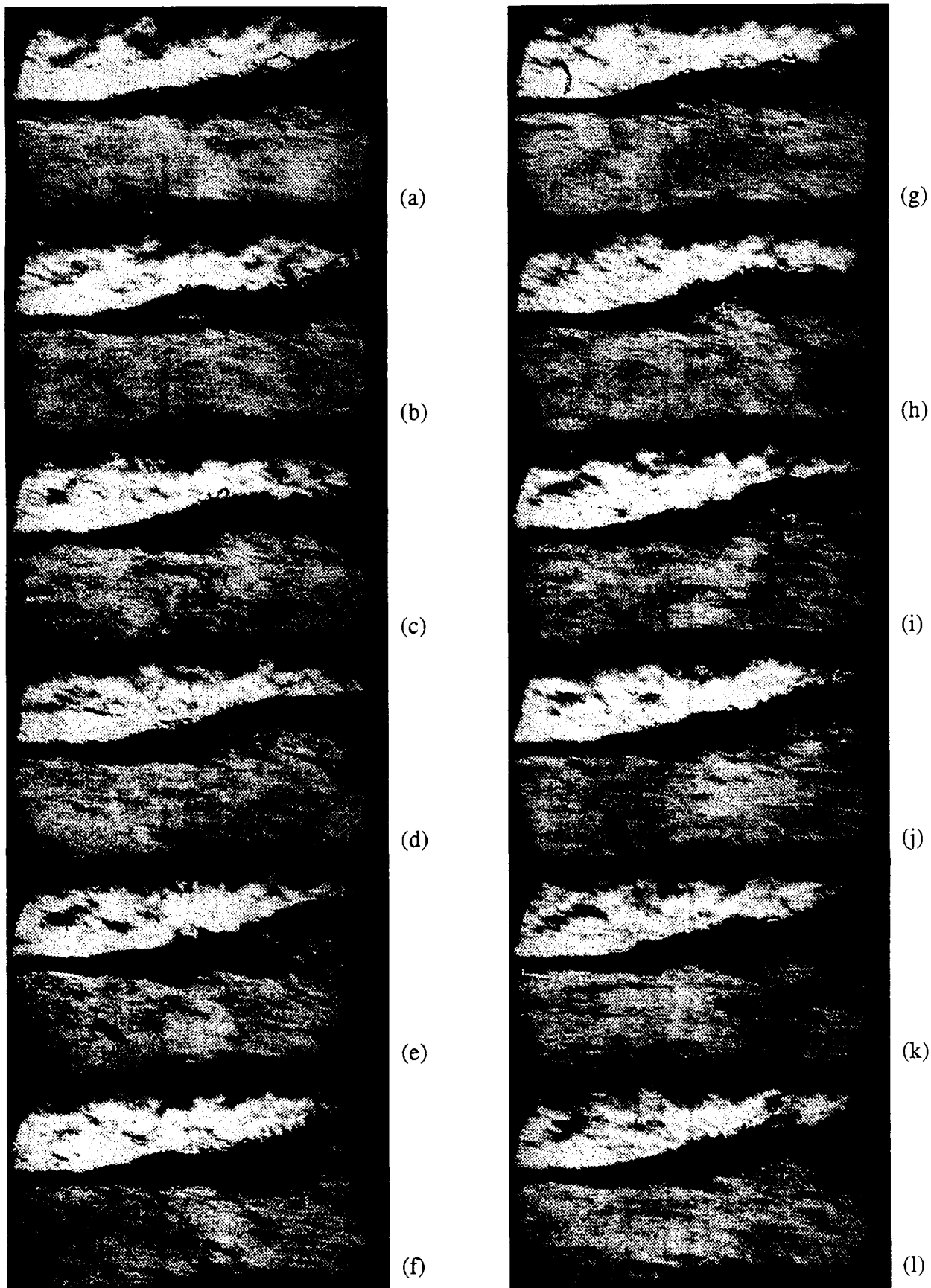


Figure 30. Schlieren images of reacting planar shear layer flows. Frames are 0.1 ms apart, start at top left downward and then shift right.

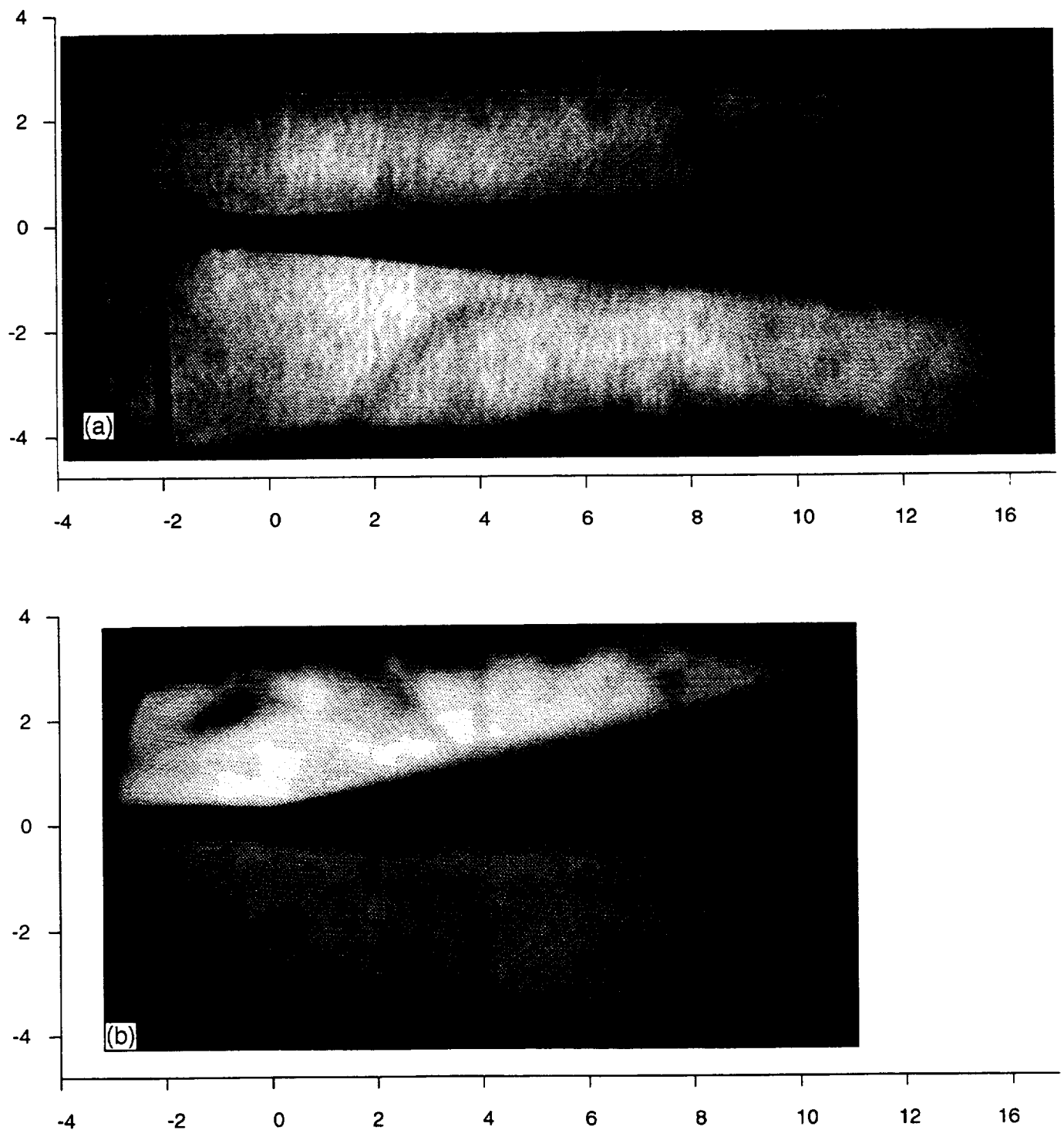


Figure 31. Mean intensity of 256 schlieren images of reacting and nonreacting planar shear layer flows. (The images are 80% of actual size, with 1:1 aspect ratio. Units are centimeters. Flow moved from left to right, with the splitter plate tip at approximately the origin. A vertical marker was placed in the lower left corner to indicate the hot air side of the image.) (a) Nonreacting. (b) Reacting.

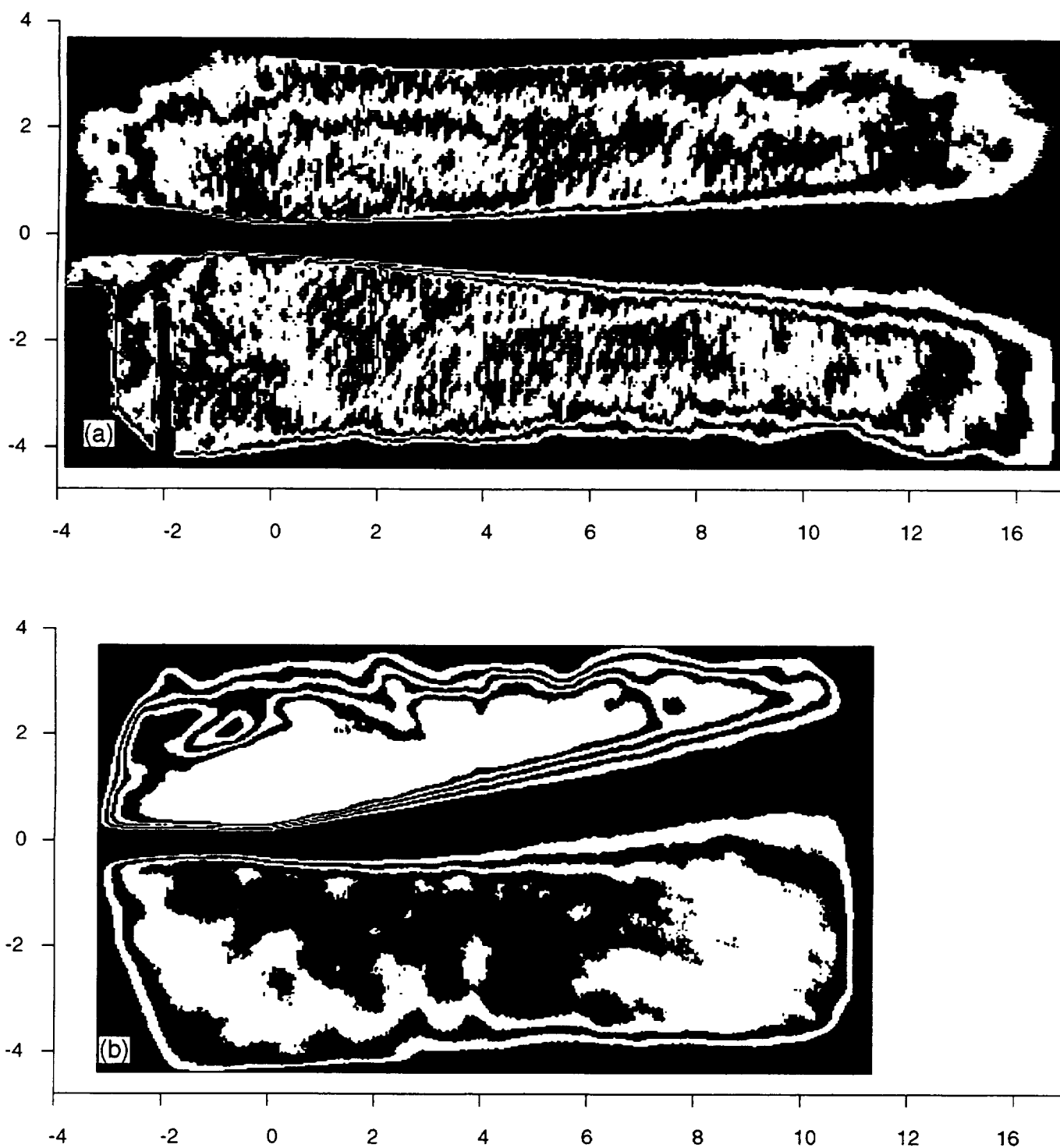


Figure 32. Mean contour of 256 schlieren images of reacting and nonreacting planar shear layer flows. (The images are 80% of actual size, with 1:1 aspect ratio. Units are centimeters. Flow moved from left to right, with the splitter plate tip at approximately the origin. A vertical marker was placed in the lower left corner to indicate the hot air side of the image.) (a) Nonreacting. (b) Reacting.

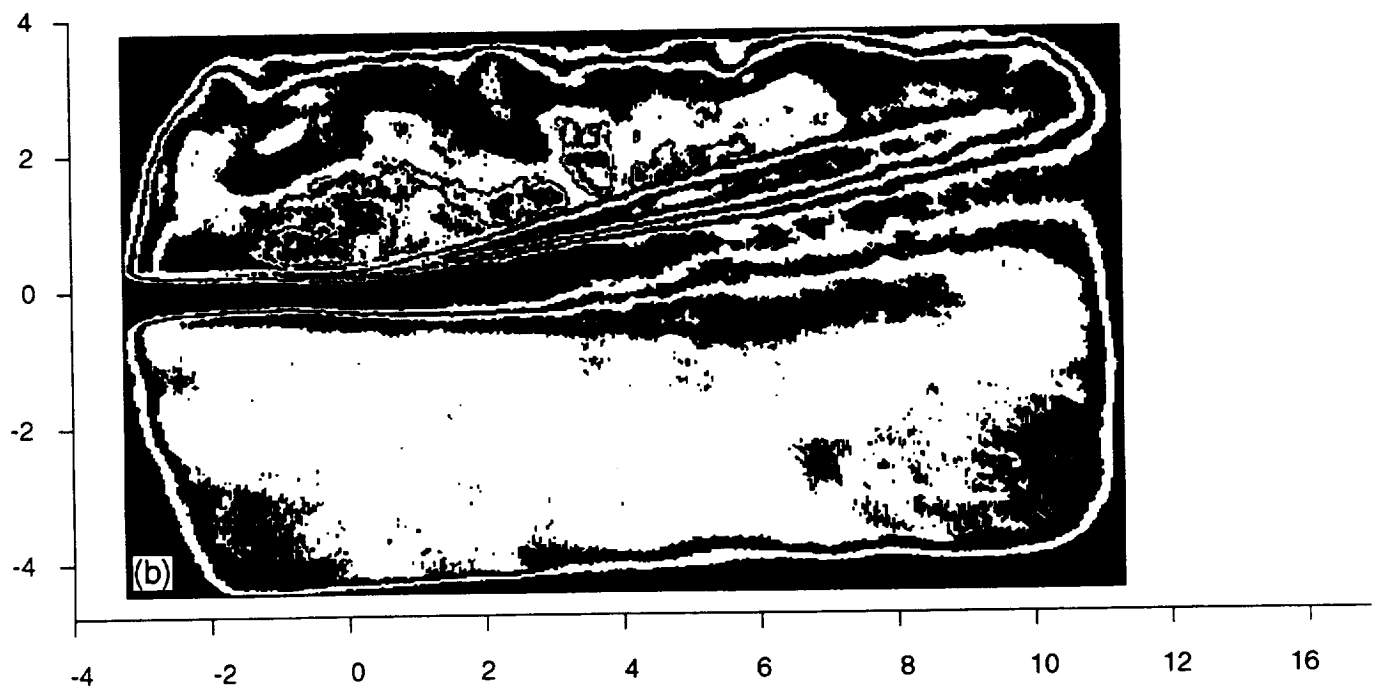
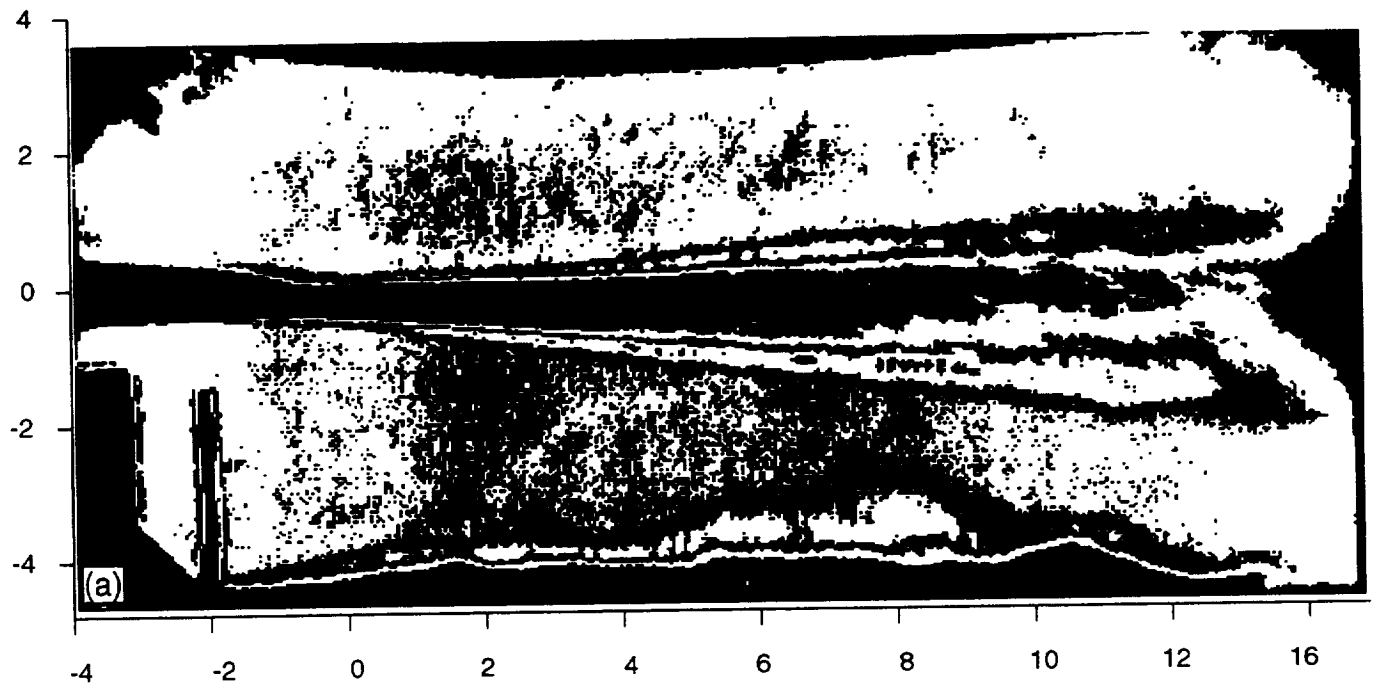


Figure 33. Rms contour of 256 schlieren images of reacting and nonreacting planar shear layer flows. (The images are 80% of actual size, with 1:1 aspect ratio. Units are centimeters. Flow moved from left to right, with the splitter plate tip at approximately the origin. A vertical marker was placed in the lower left corner to indicate the hot air side of the image.) (a) Nonreacting. (b) Reacting.

1. Layer width, mean, reacting
2. Layer width, mean, nonreacting
3. Layer width, rms, reacting
4. Layer width, rms, nonreacting

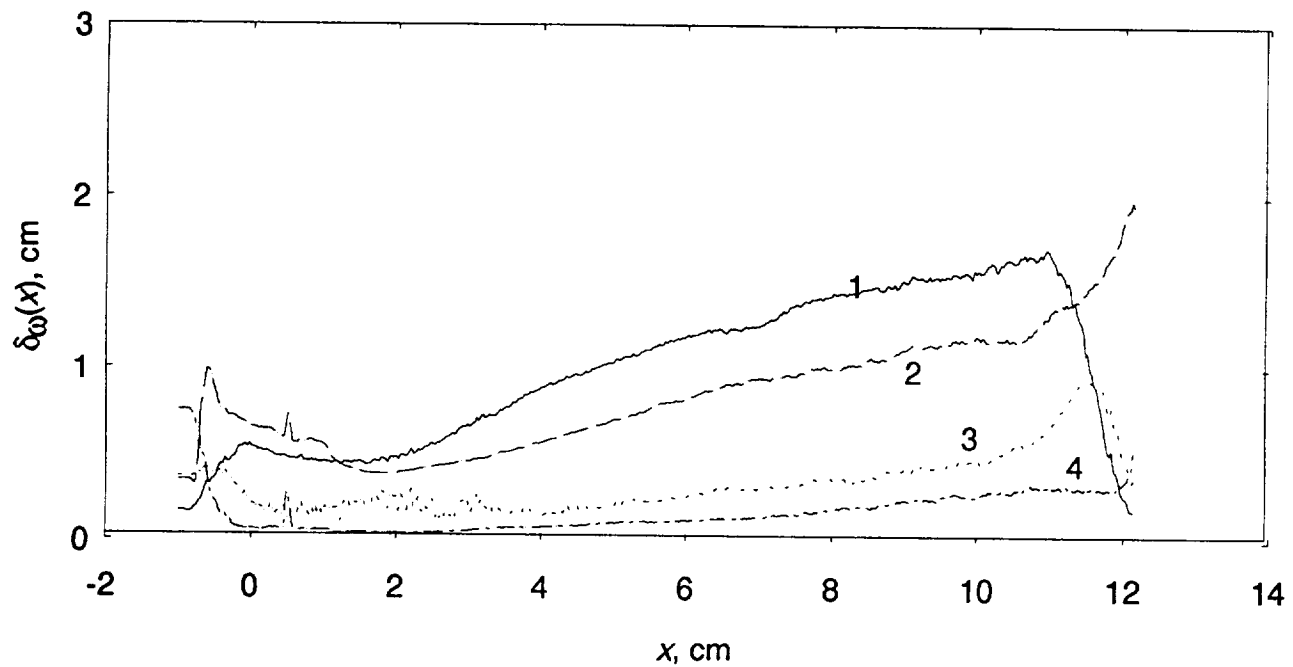


Figure 34. Mean instantaneous shear layer width ($\delta_w(x)$) without layer corrugation.

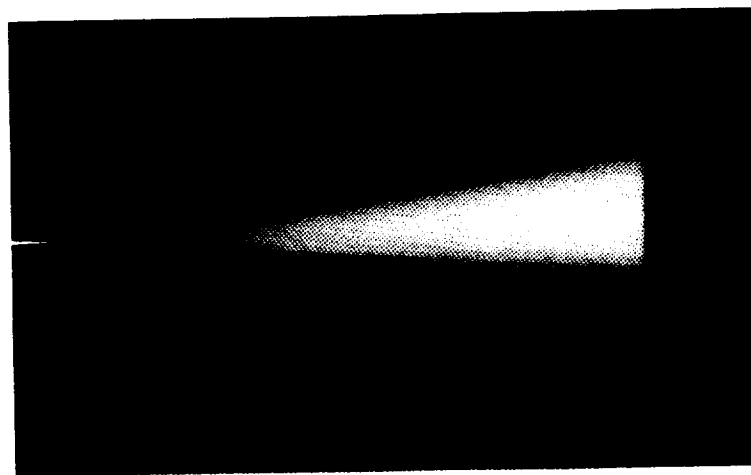


Figure 35. Long-time exposure (>1 ms) OH emission image in first window taken with Xybion camera with 306 nm interference filter. (The actual image is roughly 18 cm wide; the approximate splitter plate tip position is indicated at left.)

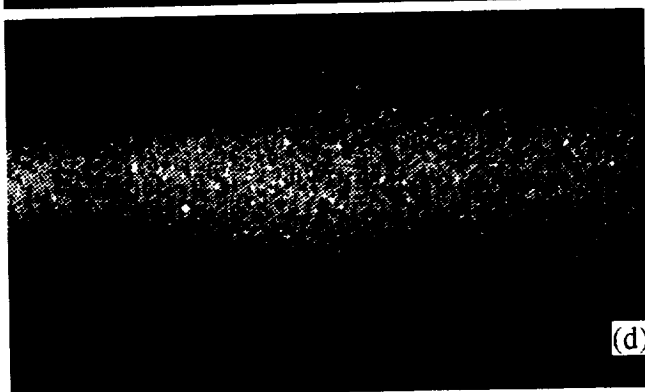
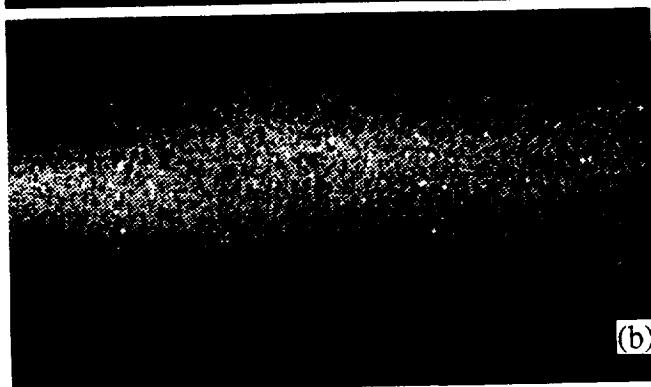
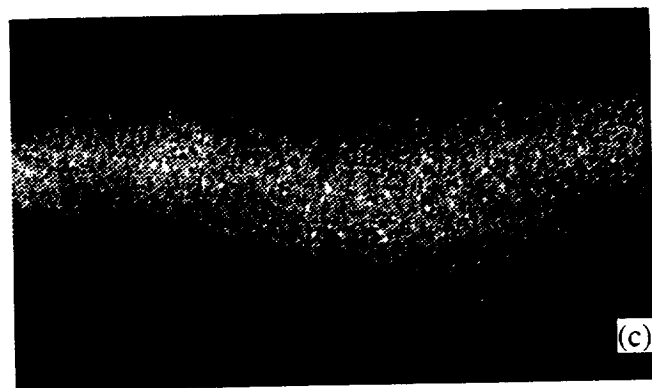


Figure 36. Instantaneous (approximately 10 ns) OH emission image approximately 5 cm downstream of splitter plate taken with a Xybion camera with 306 nm interference filter. (The images are 512 pixels wide by 300 pixels high, with an aspect ratio of 1. The image width roughly corresponds to 5 cm.)

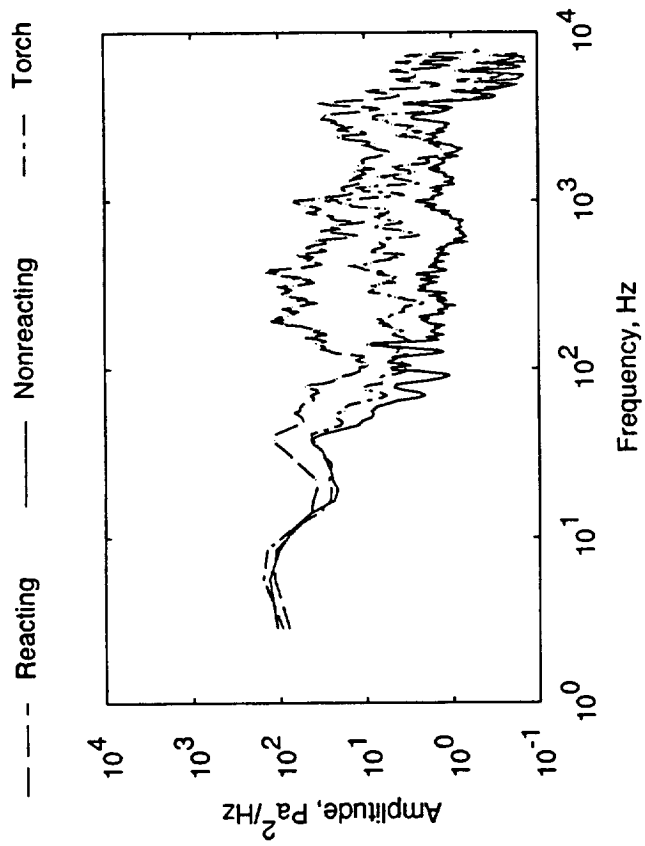


Figure 37. Spectral density of microphone 5 at airstream nozzle inlet near hydrogen torch.

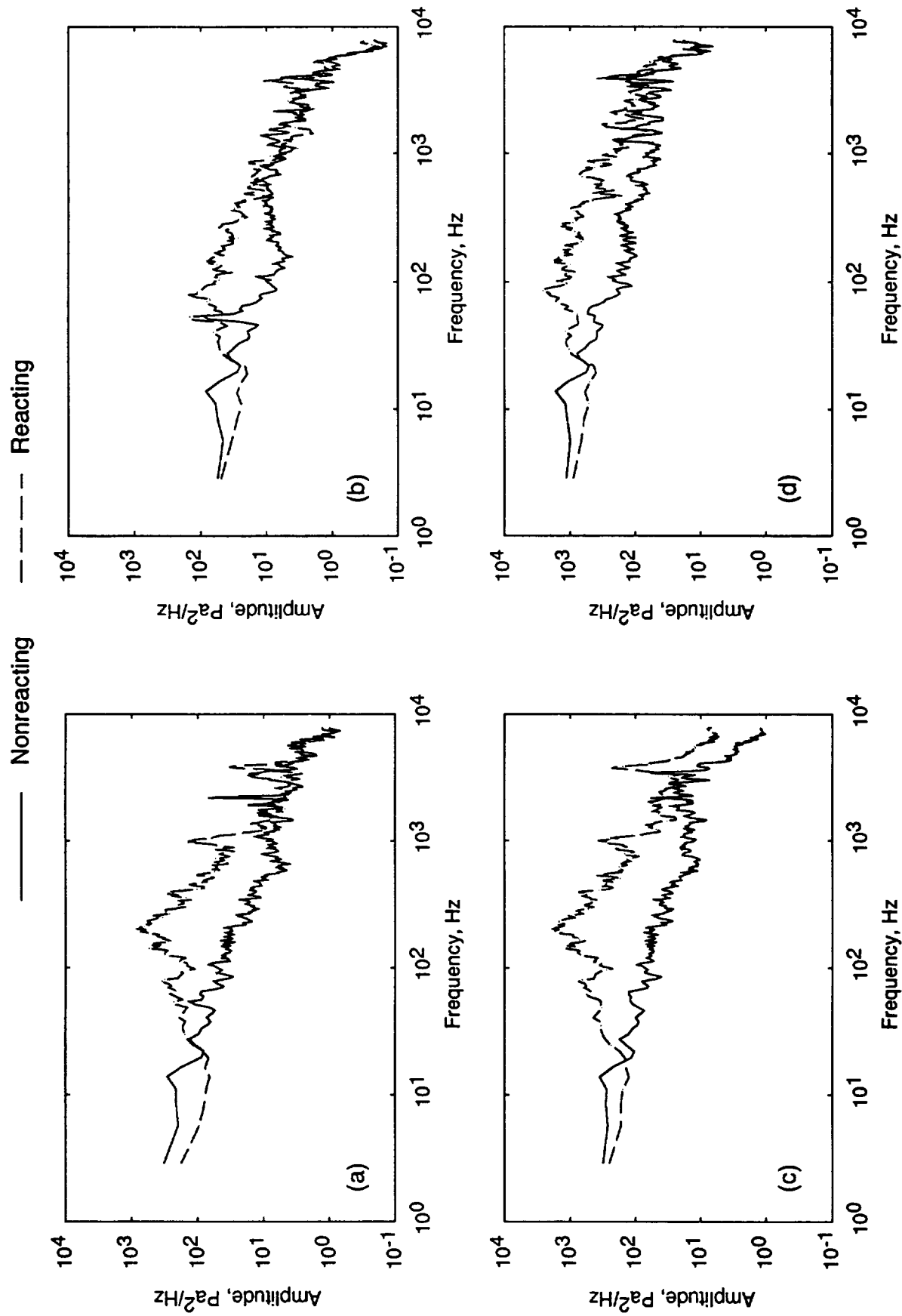


Figure 38. Spectral density distribution of microphones for planar shear layer with and without reaction. (a) Microphone 2. (b) Microphone 3. (c) Microphone 6. (d) Microphone 7.

△ Nonreacting ◇ Torch ○ Reacting

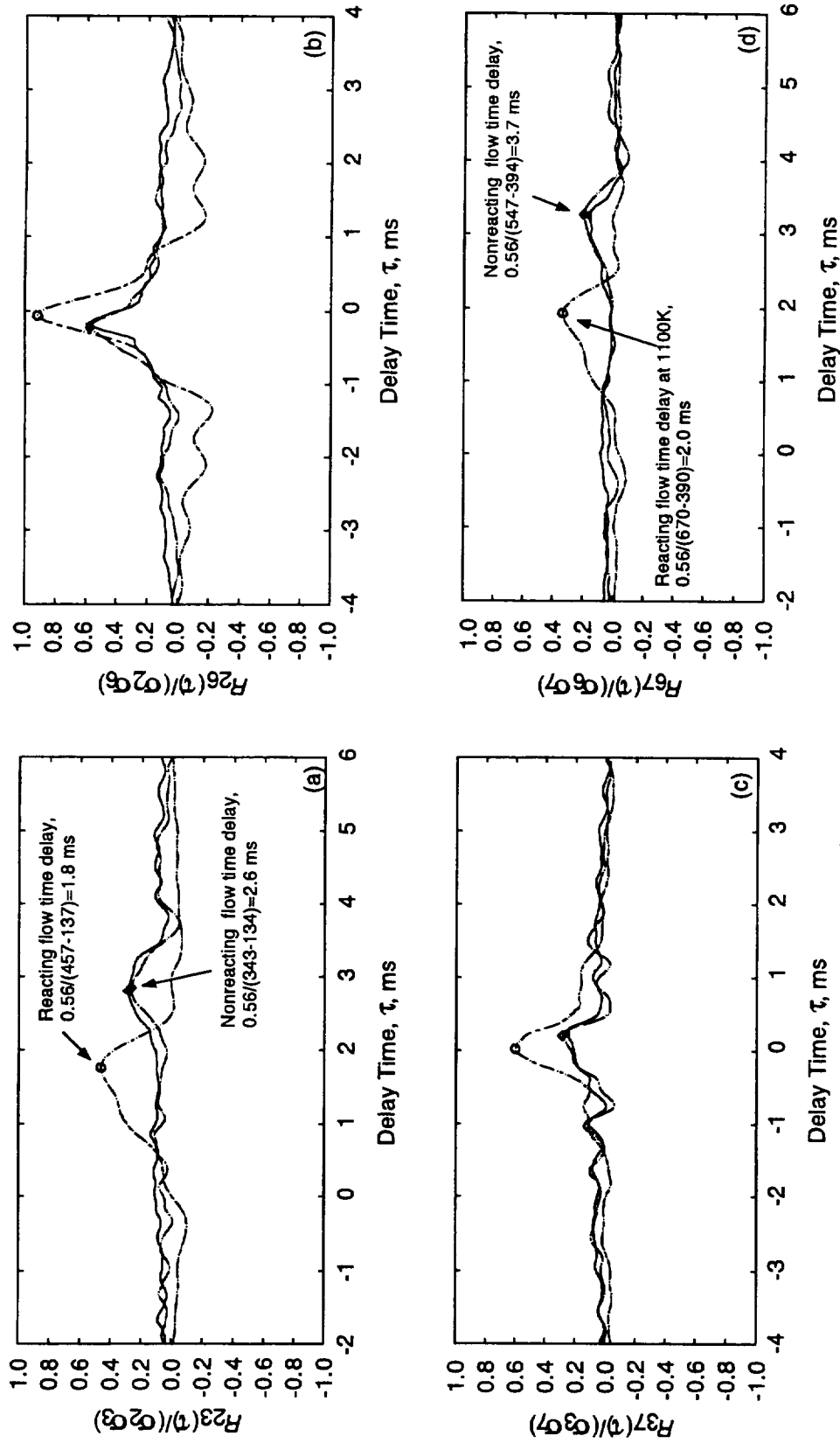


Figure 39. Microphone temporal signal cross-correlation ($R_{ab}(\tau)$) normalized by signal rms (σ_a, σ_b). (Microphone location shown in figure 13. Test date, 93-05-25.) (a) Between microphones 2 and 3, on low-speed fuel side of shear layer. (b) Between microphones 2 and 6, across shear layer, upstream position. (c) Between microphones 3 and 7, across shear layer, downstream position. (d) Between microphones 6 and 7, on high-speed air side of shear layer.

REPORT DOCUMENTATION PAGE			Form Approved OMB No. 0704-0188	
Public reporting burden for this collection of information is estimated to average 1 hour per response, including the time for reviewing instructions, searching existing data sources, gathering and maintaining the data needed, and completing and reviewing the collection of information. Send comments regarding this burden estimate or any other aspect of this collection of information, including suggestions for reducing this burden, to Washington Headquarters Services, Directorate for Information Operations and Reports, 1215 Jefferson Davis Highway, Suite 1204, Arlington, VA 22202-4302, and to the Office of Management and Budget, Paperwork Reduction Project (0704-0188), Washington, DC 20503.				
1. AGENCY USE ONLY (Leave blank)	2. REPORT DATE June 1996	3. REPORT TYPE AND DATES COVERED Technical Paper		
4. TITLE AND SUBTITLE Experimental Reacting Hydrogen Shear Layer Data at High Subsonic Mach Number		5. FUNDING NUMBERS WU-505-62-52		
6. AUTHOR(S) C.T. Chang, C.J. Marek, C. Wey, and C.C. Wey				
7. PERFORMING ORGANIZATION NAME(S) AND ADDRESS(ES) National Aeronautics and Space Administration Lewis Research Center Cleveland, Ohio 44135-3191		8. PERFORMING ORGANIZATION REPORT NUMBER E-7693		
9. SPONSORING/MONITORING AGENCY NAME(S) AND ADDRESS(ES) National Aeronautics and Space Administration Washington, D.C. 20546-0001		10. SPONSORING/MONITORING AGENCY REPORT NUMBER NASA TP-3342		
11. SUPPLEMENTARY NOTES C.T. Chang and C.J. Marek, NASA Lewis Research Center; C. Wey, NYMA, Inc., 2001 Aerospace Parkway, Brook Park, Ohio 44142 (work funded by NASA Contract NAS3-27186); C.C. Wey, Ohio Aerospace Institute, 22800 Cedar Point Road, Brook Park, Ohio 44142. Responsible person, C.T. Chang, organization code 2650, (216) 433-8561.				
12a. DISTRIBUTION/AVAILABILITY STATEMENT Unclassified - Unlimited Subject Category 07 This publication is available from the NASA Center for Aerospace Information, (301) 621-0390.			12b. DISTRIBUTION CODE	
13. ABSTRACT (Maximum 200 words) The flow in a planar shear layer of hydrogen reacting with hot air was measured with a two-component laser Doppler velocimeter (LDV) system, a schlieren system, and OH fluorescence imaging. It was compared with a similar air-to-air case without combustion. The high-speed stream's flow speed was about 390 m/s, or Mach 0.71, and the flow speed ratio was 0.34. The results showed that a shear layer with reaction grows faster than one without; both cases are within the range of data scatter presented by the established data base. The coupling between the streamwise and the cross-stream turbulence components inside the shear layers was low, and reaction only increased it slightly. However, the shear layer shifted laterally into the lower speed fuel stream, and a more organized pattern of Reynolds stress was present in the reaction shear layer, likely as a result of the formation of a larger scale structure associated with shear layer corrugation from heat release. Dynamic pressure measurements suggest that coherent flow perturbations existed inside the shear layer and that this flow became more chaotic as the flow advected downstream. Velocity and thermal variable values are listed in this report for a computational fluid dynamics (CFD) benchmark.				
14. SUBJECT TERMS Shear layer; Planar, Reaction, Turbulent; Hydrogen; LDV			15. NUMBER OF PAGES 89	
			16. PRICE CODE A05	
17. SECURITY CLASSIFICATION OF REPORT Unclassified	18. SECURITY CLASSIFICATION OF THIS PAGE Unclassified	19. SECURITY CLASSIFICATION OF ABSTRACT Unclassified	20. LIMITATION OF ABSTRACT	

National Aeronautics and
Space Administration

Lewis Research Center
21000 Brookpark Rd.
Cleveland, OH 44135-3191

Official Business
Penalty for Private Use \$300

POSTMASTER: If Undeliverable — Do Not Return